



Deliverable 7.10: HITEC – Modelling

Work Package 7

The project leading to this application has received funding from the European Union's Horizon 2020 research and innovation programme under grant agreement No 847593.



EURAD Deliverable 7.10 – HITEC Modelling**Document information**

Project Acronym	EURAD
Project Title	European Joint Programme on Radioactive Waste Management
Project Type	European Joint Programme (EJP)
EC grant agreement No.	847593
Project starting / end date	1st June 2019 – 30 May 2024
Work Package No.	7
Work Package Title	Influence of Temperature on Clay-based Material Behaviour
Work Package Acronym	HITEC
Deliverable No.	7.10
Deliverable Title	HITEC Modelling
Lead Beneficiary	UPC
Contractual Delivery Date	March 2023
Actual Delivery Date	June 2024
Type	Final report of WP7 Task 3.3
Dissemination level	Public
Authors	Ramon B. de Vasconcelos (UPC), Carlos E. Rodríguez (UPC), Antonio Gens (UPC), Tomáš Krejčí (CTU), David Mašín (CU), Tomáš Koudelka (CTU), Jaroslav Kruis (CTU), Veli-Matti Pulkkanen (VTT), Olli-Pekka Rauhala (VTT)

To be cited as:

de Vasconcelos R. B., Rodríguez C. E., Gens A., Krejčí T., Mašín D., Koudelka T., Kruis J., Pulkkanen V.-M., Rauhala, O.-P. (2021): HITEC modelling. Deliverable D7.10 of the HORIZON 2020 project EURAD. EC Grant agreement no: 847593.

Disclaimer

All information in this document is provided "as is" and no guarantee or warranty is given that the information is fit for any particular purpose. The user, therefore, uses the information at its sole risk and liability. For the avoidance of all doubts, the European Commission has no liability in respect of this document, which is merely representing the authors' view.

Acknowledgement

This document is a deliverable of the European Joint Programme on Radioactive Waste Management (EURAD). EURAD has received funding from the European Union's Horizon 2020 research and innovation programme under grant agreement No 847593.

EURAD Deliverable 7.10 – HITEC Modelling

Status of deliverable		
	By	Date
Delivered (Lead Beneficiary)	[UPC]	
Verified (WP Leader)	Markus Olin [VTT]	19/02/2024
Reviewed (Reviewers)	Michael Holmboe, Liu Jinsong	18/05/2024
Approved (PMO)	Bharti Reddy	31/05/2024
Submitted to EC	Andra (Coordinator)	03/06/2024

EURAD Deliverable 7.10 – HITEC Modelling

Authors

Organisation	Authors
UPC	Ramon B. de Vasconcelos, Carlos E. Rodríguez, Antonio Gens
CTU	Tomáš Krejčí, Tomáš Koudelka, Jaroslav Kruis
CU	David Mašín
VTT	Veli-Matti Pulkkanen, Olli-Pekka Rauhala

Executive Summary

This report presents a summary of ongoing modelling activities within EURAD WP7 HITEC (Influence of temperature on clay-based material behaviour). Three teams have been involved, namely CIEMAT (UPC), SURAO (CTU and CU) and VTT.

CIEMAT (UPC) developed a constitutive model as a THM extension of an existing double structure elastoplastic model that incorporates the effects of temperature. Thermal-induced strains are considered reversible at this stage of model development. The numerical simulations of the benchmark experiment defined in MS130 were performed, while the material parameters were calibrated either from bentonite tested at high temperature or by back-calculations. The model reproduced quite well the main features observed during the test of the heated column, i.e. the evolution of temperature, relative humidity, water intake and axial pressure throughout the test. However, some discrepancies have been found between the numerical results and the laboratory data regarding the final distribution of dry density and saturation.

SURAO (CTU and CU) developed and validated the THM hypoplastic model for bentonite. Its formulation has already been available at the start of EURAD project, however, within EURAD, the model was calibrated to represent high temperature experiments and several of its components (such as the formulation of water retention curves and formulation for microstructural collapse) were further developed. The model has been used in simulations of benchmark experiments performed at CTU. Good fit was demonstrated for temperature evolution. Problematic aspects remaining to be solved were simulations of extremely low dry density bentonite, adopted in CTU benchmark 1, and vapour generation during heating above 100°C in CTU benchmark 2, which led to calculation which did not converge.

Finally, VTT prepared a numerical model of the thermal conditions in Olkiluoto disposal site in Finland to obtain a realistic view of the expected thermal conditions. The model includes thermal conduction through the disposal site components surrounding one disposal hole, but also thermal radiation was considered over gas filled gaps within the disposal canister. For simulations, VTT proposed to use Varied Multiplicative Processes model developed within the scope of large deformation plasticity. Simulations of Olkiluoto disposal site are to be finished once the experimental work for the mechanical model dependencies on the temperature by VTT has been finished.

Table of content

Executive Summary.....	5
Table of content.....	6
List of figures	8
List of Tables	11
Glossary.....	12
1. UPC (CIEMAT)	13
1.1 Introduction.....	13
1.2 Description of the formulation and constitutive models	14
1.2.1 Phase diagrams and basic relationships	15
1.2.2 Additive decomposition of the strain tensor	17
1.2.3 The local mass transfer mechanism	18
1.2.4 Balance equations	18
1.2.5 Thermal and hydraulic constitutive equations	21
1.2.6 Mechanical constitutive equations	23
1.3 Benchmark application	29
1.3.1 Description of the benchmark.....	29
1.3.2 Model domain and boundary conditions	34
1.3.3 Thermal, hydraulic and mechanical parameters.....	36
1.3.4 Modelling results and discussion	40
1.3.5 Concluding Remarks	46
1.4 References.....	47
2. CTU & CU (SÚRAO)	49
2.1 Introduction.....	49
2.2 Hypoplastic model overview.....	49
2.2.1 Model background	49
2.2.2 Introduction of hypoplastic framework	50
2.2.3 Mathematical formulation of the THM model.....	52
2.2.4 Input parameters.....	53
2.3 Numerical model of the small-scale experiment	55
2.4 Simulation results of the first run.....	59
2.5 Simulation results of the second run	67
2.6 References	71
3. VTT	72
3.1 Introduction	72
3.2 Pre-modelling and input to experiments	72

EURAD Deliverable 7.10 – HITEC Modelling

3.2.1	Pre-modelling.....	72
3.2.2	Input to experiments	73
3.3	Thermal phenomena to Varied Multiplicative Processes model.....	73
3.3.1	Conceptual model.....	73
3.3.2	(Im)balance equations	74
3.3.3	Multiplicative decomposition of the deformation gradient.....	75
3.3.4	Constitutive assumptions and equations	76
3.3.5	Discussion on included thermal phenomena.....	78
3.4	Thermal dependency of mechanical constitutive models	78
3.5	References	79

List of figures

Figure 1.1: (a) Typical soil fabrics in active clays [1]; (b) Schematic representation of an aggregation of active clays [2].	13
Figure 1.2: Phase diagrams relating volumes (left) and mass of species (right) in each structural level [6].	15
Figure 1.3: Water retention curves (WRC) for the macro- and micro-structural domains of compacted samples of MX-80 bentonite. Experimental data for the MX-80 bentonite at several dry densities from [14-16].	23
Figure 1.4: Three-dimensional representation of the BBM yield surface (modified from [17]).	27
Figure 1.5: Structural coupling functions for the micro-macro coupling mechanism [17].	28
Figure 1.6: Layout of the benchmark column experiment.	30
Figure 1.7: MX-80 bentonite pellets used in the experiment (left) and grading curve of the MX-80 pellets obtained by dry sieving (right).	31
Figure 1.8: (a) Pouring the pellets inside the cell; (b) View of the assembled column; (c) View of the column after installing the thermal insulation.	32
Figure 1.9: Temperature changes due to the improvement of the external insulation system The thick vertical line indicate the reinforcement of the thermal isolation system [21].	33
Figure 1.10: Laboratory temperature, heater power and temperature at 10 cm from the heater (T3) during the hydration stage of the test [20].	33
Figure 1.11: Final water content (left) and dry density (right) distribution along the bentonite column. The dotted horizontal lines represents the initial values [20].	34
Figure 1.12: (a) Finite element mesh generated to simulate the large bentonite cell; (b) modelled domain of the bentonite column before (left) and after (right) the reinforcement of the external isolation system.	35
Figure 1.13: Thermo-hydraulic boundary conditions applied during the infiltration test. Time=0 corresponds to the beginning of heating.	36
Figure 1.14: Variation of thermal conductivity with degree of saturation. Experimental data collected from [21, 23-26].	37
Figure 1.15: Water retention curves for macrostructure (left) and microstructure (right) of MX-80 pellets Symbols represent experimental results (from [14-16]) and full lines correspond to the granular bentonite retention curves used in the modelling of the benchmark.	37
Figure 1.16: Coupling functions used in the numerical modelling.	40
Figure 1.17: Evolution of temperature (left) and RH (right) up to 5000 hours of heating (before the start of hydration).	41
Figure 1.18: Distribution of temperature (left) and RH (right) along the column of pellets for several times (before the start of hydration).	41
Figure 1.19: Water intake during the hydration phase of the test.	42
Figure 1.20: Evolution of temperature (left) and RH (right) until 20000 hours of heating (15000 hours of hydration).	42
Figure 1.21: Distribution of temperature (left) and RH (right) along the column of pellets for several times (up to the first 15000 hours of hydration).	43

EURAD Deliverable 7.10 – HITEC Modelling

Figure 1.22: Evolution of the axial stress at the top of the column of pellets (up to 15000 hours of hydration).....	43
Figure 1.23: Evolution (left) and longitudinal profiles (right) of RH until the end of the test.....	44
Figure 1.24: Evolution of macro and micro suction at 1 cm, 5 cm and 49 cm (left) and at 10 cm, 22 cm and 40 cm (right) from the heater until the end of the test. Symbols represent the average suction estimated by the psychrometric relationships from the data provided by the RH sensors.	44
Figure 1.25: Saturation profile along the column of pellets at the end of the test. Symbols represent the experimental data obtained in the post-mortem analyses [20].....	44
Figure 1.26: Dry density profile along the column of pellets at the end of the infiltration test. Symbols represent the experimental data obtained from the post-mortem observations [20].....	45
Figure 1.27: Evolution of the axial stress at the top of the column of pellets until the end of the test. Model results are given for two different macro-micro water exchange parameter values.....	46
Figure 1.28: Model results from the constitutive analysis using the same input parameters considered in the benchmark (left) and experimental data (from [29-33]) relating the swelling pressure to dry density values (right).....	46
Figure 2.1: Schematic representation of double structure concept (Mašín [10, 12]).	49
Figure 2.2: Schematic representation of the double structure coupling concept adopted in the hypoplastic model (Mašín, 2013 & 2017).	50
Figure 2.3: Demonstration of hypoplasticity principles using a simple one-dimensional model.	51
Figure 2.4: Hysteretic water retention model for macrostructure adopted in hypoplastic THM model for expansive soils – definition of variables (left) and smooth formulation adopted in recent version of the model (right).....	52
Figure 2.33: Installation and the setup of the experiment.....	56
Figure 2.34: Set up of the numerical model.....	56
Figure 2.35: Prescribed water pressure.....	57
Figure 2.36: Temperature history in sensor 214.10.....	60
Figure 2.37: Temperature history in sensor 314.10.....	61
Figure 2.38: Temperature history in sensor 414.10.....	61
Figure 2.39: Temperature history in sensor 511.10.....	62
Figure 2.40: Temperature history in sensor 513.10.....	62
Figure 2.41: Temperature history in sensor 611.10.....	63
Figure 2.42: Temperature history in sensor 613.10.....	63
Figure 2.43: Temperature profile at the end time.....	64
Figure 2.44: Vertical pressure evolution.....	64
Figure 2.45: Saturation degree profile at time 20 days.....	65
Figure 2.46: Saturation degree profile at time 40 days.....	65
Figure 2.47: Saturation degree profile at time 60 days.....	66
Figure 2.48: Scheme of the instrumentation [17].....	67
Figure 2.49: Temperature history in sensor 1215.....	68
Figure 2.50: Temperature history in sensor 1614.....	68

EURAD Deliverable 7.10 – HITEC Modelling

<i>Figure 2.51: Relative humidity evolution</i>	69
<i>Figure 2.52: Saturation degree evolution</i>	69
<i>Figure 2.53: Swelling pressure in radial direction at the bottom</i>	70
<i>Figure 2.54: Swelling pressure in horizontal direction at the bottom</i>	70
<i>Figure 3.1. An example of modelled temperature field surrounding a disposal canister in Olkiluoto disposal site in Finland.</i>	72
<i>Figure 3.2. An illustration of the conceptual model. Solid material and bound water form the bentonite skeleton, while the free porosity is filled either with gas or (free) water where salts can be dissolved. If water moves from the free porosity to the bound state, the bentonite swells. If the movement of water is in reverse direction, the bentonite shrinks.</i>	74
<i>Figure 3.3. Illustration of the multiplicative decomposition of the deformation gradient, mapping properties and the intermediate configurations corresponding to the decomposition.</i>	76

List of Tables

<i>Table 1.1 Notation used in the mathematical description of the double porosity formulation</i>	14
<i>Table 1.2. Balance equations for a double porosity approach (in CODE_BRIGTH) and their unknowns</i>	18
<i>Table 1.3: Main characteristics of the granular bentonite column after installation</i>	31
<i>Table 1.4: Initial conditions for the MX-80 bentonite pellets</i>	35
<i>Table 1.5: Thermal parameters</i>	36
<i>Table 1.6: Model parameters for the retention curves</i>	38
<i>Table 1.7: Hydraulic parameters for the advective water flow in the macrostructure</i>	38
<i>Table 1.8: Main elastic parameters for the bentonite material (MX-80 pellets)</i>	39
<i>Table 1.9: Model parameters for the elastoplastic behaviour (LC mechanism) of the MX-80 pellets</i> ...	39
<i>Table 1.10: Parameters for the coupling functions (see Figure 1.16)</i>	40
<i>Table 2.1: Model parameters and their description (from Mašín [12]).</i>	54
<i>Table 2.2: Material parameters of THM model – transport part</i>	57
<i>Table 2.3: Material parameters of THM model – mechanical part</i>	58
<i>Table 2.4: THM hypoplastic constitutive model parameters for bentonite</i>	58

Glossary

HLW	High-Level Waste
SF	Spent Fuel
WP	Work Package

1. UPC (CIEMAT)

1.1 Introduction

The objective of the UPC (CIEMAT) team is the development of a conceptual framework and a mathematical model for clay buffer material able to incorporate the effects of temperature on their thermo-hydro-mechanical (THM) behaviour. The conceptual framework and mathematical model are based on a coupled THM formulation and appropriate constitutive laws that are described in the next section.

A characteristic feature of the formulation is the adoption of a double structure (or double porosity) scheme that distinguishes between two porosity levels (microstructure and macrostructure). In such scheme, the porous medium is described by a micro-pore domain, composed by the internal structure of individual particles and aggregates of active clays and a macrostructural level corresponding to the arrangement of clay aggregates and other soil grains with macro-pores among them [1], as illustrated in *Figure 1.1*. The micro-pore fraction in this double structure formulation includes both the intra- and the inter-particle voids within a clay aggregate (micro- and meso-pores). The consideration of these distinct but overlapping structural media allows the tracking of the evolution of the clay microstructure. As presented below, this double structure model has been developed in a generalized elastoplastic framework that incorporates two different plastic mechanisms.

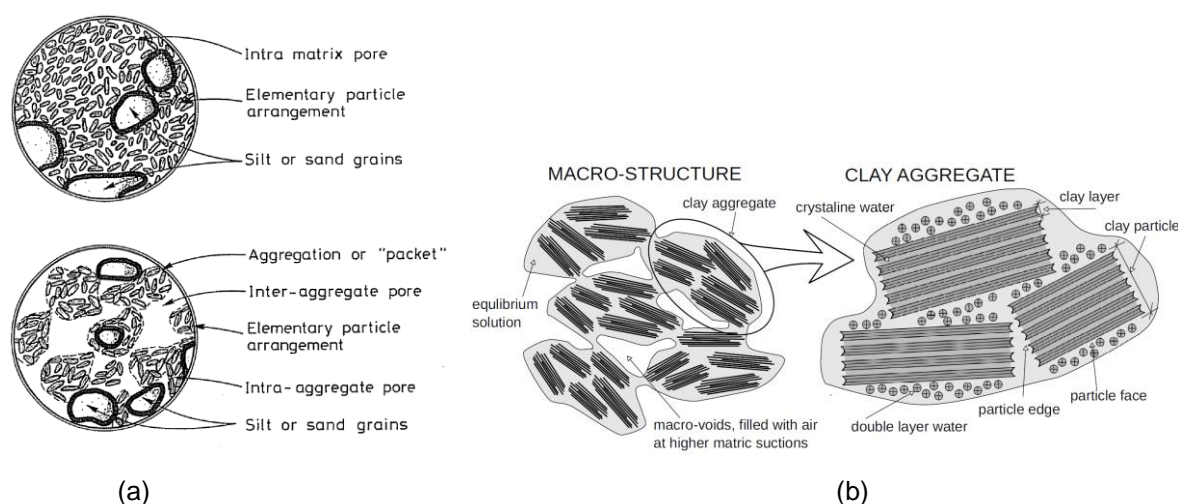


Figure 1.1: (a) Typical soil fabrics in active clays [1]; (b) Schematic representation of an aggregation of active clays [2].

Some of the main features of the double porosity model developed are listed below:

- The microstructure may be unsaturated.
- Advective fluxes through micro-pores are neglected due to the very low mobility of water and gas in that structural domain.
- No hydraulic equilibrium between microstructure and macrostructure is prescribed. This local difference of the water potential in macro- and micro-pores controls the mass of water exchanged between both pore domains (hydraulic structural coupling).
- Microstructural deformations are fully reversible (although non-linear) and purely volumetric.
- Microstructural behaviour is not affected by the deformation state of the macrostructure.
- Plastic macrostructural strains may arise from deformations of the microstructure (mechanical structural coupling).

EURAD Deliverable 7.10 – HITEC Modelling

- No generation of plastic thermal strains is considered at this stage. However, irreversible structural changes due to the thermo-hydronechanical (THM) coupling are possible.

The THM formulation has been implemented in the finite element code CODE_BRIGHT.

1.2 Description of the formulation and constitutive models

The THM formulation requires a set of balance equations and constitutive laws for dealing with the THM coupled processes that may take place in the buffer material. This set of basic equations is written in terms of the primary variables (liquid and gas pressures, displacement, temperature). When the constitutive equations are incorporated into the balance equations [3], a system of partial differential equations is generated that must be solved numerically in a completely coupled way.

The mathematical formulation described in this report is based on the general approach proposed in [3-5], applied to both isothermal and non-isothermal problems in double structure unsaturated media. For a better understanding of the mathematical description of the governing equations, the notation used in the development of the double porosity formulation is presented in *Table 1.1*.

Table 1.1 Notation used in the mathematical description of the double porosity formulation

$(\dot{\blacksquare})$	Incremental (or rate) form of a generic variable.
$(\blacksquare)_{\alpha}, (\blacksquare)_{\beta}, (\blacksquare)_{\alpha\beta}$	Subscripts used to identify the structural level (" $\beta \equiv m$ " for microstructure; " $\beta \equiv M$ " for macrostructure) and/or phases (" $\alpha \equiv s$ " for solid; " $\alpha \equiv l$ " for liquid; " $\alpha \equiv g$ " for gas).
$(\blacksquare)^{\gamma}$	Superscript used to identify the species present in the porous medium (" $\gamma \equiv s$ " for solid grains (mineral); " $\gamma \equiv w$ " for water; " $\gamma \equiv a$ " for air).
$V_s; V_{\alpha\beta}; V$	Volume of the solid species/phase; volume of the α phase (liquid or gas) in the β -structural medium; total volume of the porous medium.
$V_p; V_{p\beta}$	Total volume of pores in the soil; volume of pores in the β -structural medium.
$(\blacksquare)_{\beta}; (\overline{\blacksquare})_{\beta}$	Variable evaluated respect to the volume occupied by the β -structural level; variable evaluated respect to the total volume of the soil.
$\phi; \phi_{\beta}$	Total porosity; porosity of the β -structural medium respect to its actual volume.
$\bar{\phi}_{\beta}$	Pore volume fraction of the β -structural medium.
$\rho_s; \rho_{\alpha\beta}$	Local density of the solid; local density of the α phase in the β -structural medium.
$\omega_{\alpha\beta}^{\gamma}$	Mass fraction of the γ species (solid, water or gas), in the α phase, in the β -structural medium.
$\theta_{\alpha\beta}^{\gamma}$	Partial density of the γ species, in the α phase, in the β -structural medium.
$m_{\alpha\beta}; m_{\alpha\beta}^{\gamma}$	Mass of the α phase in the β -structural medium; mass of the γ species (solid, water or gas), in the α phase, in the β -structural medium.
$S_{\alpha}; S_{\alpha\beta}$	Degree of saturation of the α phase in the soil; degree of saturation of the α phase in the β -structural medium.
s_{β}	Suction at the β -structural level.
E_{α}	Specific internal energy of the α phase.
$\mathbf{j}_{\alpha\beta}^{\gamma}$	Flux of the γ species, in the α phase, in the β -structural medium respect to the solid skeleton.
$\mathbf{q}_{\alpha\beta}$	Advective flux of the α phase in the β -structural medium.
\mathbf{i}_c	Conductive heat flux.

$\sigma, \sigma_\beta; \sigma_t$	Effective stress tensor for the whole porous medium and for the β -structural medium; total stress tensor.
----------------------------------	--

1.2.1 Phase diagrams and basic relationships

An unsaturated soil is treated as a porous multi-phase medium composed by solid grains, water (as liquid water or vapour in the gas phase) and air (as dry air or dissolved in the liquid phase) [3]. In order to define some basic volume-mass relationships commonly used in geotechnical problems, it is useful to depict the phase diagram that shows all the phases – solid (s), liquid (l) and/or gas (g) – present in the porous medium. Three-phase diagrams representing a soil element as a double porosity medium are shown in *Figure 1.2*. From the phase diagram relating volumes, it can be easily noted that the volume of voids in the soil (V_p) is the sum of the volume occupied by macro-pores ($V_{p,M}$) and micro-pores ($V_{p,m}$). The volume of microstructure (V_m) includes the volume of the intra-aggregate pores (micro-pores) and the volume occupied by the solid phase (V_s). Variables defined with the sub-index “ m ” are related to the microstructural level (solid particles and micro-pores) while the sub-index “ M ” refers to variables defined for the macrostructure. Variables defined for the soil (the whole porous medium) are not labelled with any subscript.

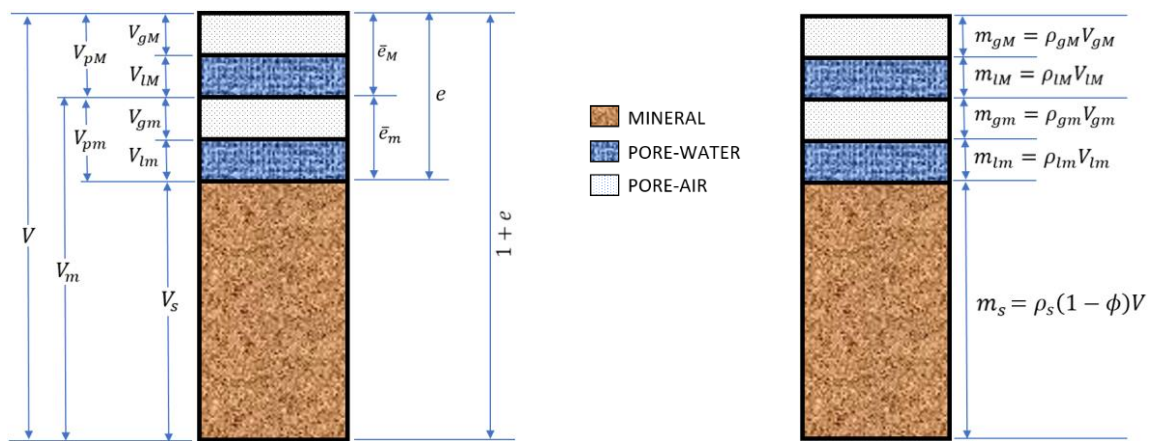


Figure 1.2: Phase diagrams relating volumes (left) and mass of species (right) in each structural level [6].

Porosities (ϕ and ϕ_m) and void ratios (e and e_m) for the two porous media (the soil and the clay aggregate) are defined as:

$$\phi = \frac{V_p}{V} \quad (1-1)$$

$$\phi_m = \frac{V_{p,m}}{V_m} \quad (1-2)$$

$$e = \frac{V_p}{V_s} = \frac{V_p}{V - V_p} = \frac{\phi}{1 - \phi} \quad (1-3)$$

$$e_m = \frac{V_{p,m}}{V_s} = \frac{V_{p,m}}{V_m - V_{p,m}} = \frac{\phi_m}{1 - \phi_m} \quad (1-4)$$

EURAD Deliverable 7.10 – HITEC Modelling

Two additional porosity variables need to be introduced in order to obtain an additive decomposition of the total porosity (ϕ),

$$\phi = \frac{V_p}{V} = \frac{V_{pm}}{V} + \frac{V_{pM}}{V} = \bar{\phi}_m + \bar{\phi}_M \quad (1-5)$$

where $\bar{\phi}_m$ and $\bar{\phi}_M$ are the pore volume fractions associated with microstructure and macrostructure, respectively. These variables are helpful for establishing the mathematical development of the double porosity formulation. The aggregate porosity (ϕ_m), or simply the micro-porosity, can be also evaluated in terms of the macro-pore ($\bar{\phi}_M$) and the micro-pore ($\bar{\phi}_m$) volume fractions according to the following relationship:

$$\phi_m = \frac{V_{pm}}{V_m} = \frac{V_{pm}}{V} \frac{V}{V_m} = \frac{V_{pm}}{V} \left(\frac{V}{V - V_{pM}} \right) = \bar{\phi}_m \left(\frac{1}{1 - \bar{\phi}_M} \right) \quad (1-6)$$

The relationship in Equation (1-5) combined with Equation (1-3) leads to the definition of a micro void ratio (\bar{e}_m) and a macro void ratio (\bar{e}_M), expressed as follows:

$$\bar{e}_m = \frac{\bar{\phi}_m}{1 - \phi} \quad (1-7)$$

$$\bar{e}_M = e - \bar{e}_m = \frac{\bar{\phi}_M}{1 - \phi} \quad (1-8)$$

It is important to mention that the substitution of Equation (1-6) into Equation (1-4) results in $e_m = \bar{e}_m$. The saturation state in the porous medium “ β ” by the α phase, $S_{\alpha\beta}$, is defined as:

$$S_{\alpha\beta} = \frac{V_{\alpha\beta}}{V_{p\beta}} \quad (1-9)$$

where $V_{\alpha\beta}$ denotes the fraction of the volume of voids in the β -structural medium ($V_{p\beta}$) filled with the α phase. The compositional approach used in CODE_BRIGHT to describe the unsaturated porous medium [4] requires the definition of the mass fraction (ω) and the partial density (θ) for each fluid species in the soil in order to also account for the dissolved air in the liquid phase and the water vapour in the gas phase. In the context of double porosity media, the mass fraction of the γ species (“w” for water and “a” for air) in the α phase, in the β -structural medium is given by:

$$\omega_{\alpha\beta}^{\gamma} = \frac{m_{\alpha\beta}^{\gamma}}{m_{\alpha\beta}} \quad (1-10)$$

while the partial density of each fluid species, in each fluid phase and for each structural level is expressed as:

EURAD Deliverable 7.10 – HITEC Modelling

$$\theta_{\alpha\beta}^{\gamma} = \frac{m_{\alpha\beta}^{\gamma}}{V_{\alpha\beta}} = \omega_{\alpha\beta}^{\gamma} \rho_{\alpha\beta} \quad (1-11)$$

where $m_{\alpha\beta}^{\gamma}$ and $m_{\alpha\beta}$ are the mass of the γ species in the α phase and the total mass of the α phase in the β -structural medium, respectively; $\rho_{\alpha\beta} = \frac{m_{\alpha\beta}}{V_{\alpha\beta}}$ is the local density for the fluid phases in each pore-structural level.

1.2.2 Additive decomposition of the strain tensor

The explicit consideration of two structural levels in the double structure approach and the definition of the micro- and macro-pore volume fractions in Equation (1-5) lead to an additive decomposition of the strain rate tensor ($\dot{\epsilon}$) into a micro- and a macro-strain component according to:

$$\dot{\epsilon} = \dot{\epsilon}_m + \dot{\epsilon}_M \quad (1-12)$$

In terms of volumetric components, such a relationship is given by:

$$\dot{\epsilon}^v = \dot{\epsilon}_m^v + \dot{\epsilon}_M^v \quad (1-13)$$

where the volumetric strain rate ($\dot{\epsilon}^v$) and its micro ($\dot{\epsilon}_m^v$) and macro ($\dot{\epsilon}_M^v$) components are defined as:

$$\dot{\epsilon}^v = \frac{\dot{V}}{V} = \frac{\dot{V}_s + \dot{V}_p}{V} = \frac{\dot{V}_s + \dot{V}_{pm}}{V} + \frac{\dot{V}_{pM}}{V} \quad (1-14)$$

$$\dot{\epsilon}_m^v = \frac{\dot{V}_s + \dot{V}_{pm}}{V} \quad (1-15)$$

$$\dot{\epsilon}_M^v = \frac{\dot{V}_{pM}}{V} \quad (1-16)$$

It is important to emphasize the distinction between the micro component of the volumetric strains, shown in Equation (1-15), which is defined in terms of the total volume of the porous medium (V) and the actual volumetric deformation of the clay aggregate ($\dot{\epsilon}_m^v$), which is related to the volume occupied by the microstructure (V_m). However, the volume phase diagram of *Figure 1.2*, these micro-structural deformations are related by the following expression:

$$\dot{\epsilon}_m^v = \frac{\dot{V}_m}{V_m} = \frac{\dot{V}_s + \dot{V}_{pm}}{V_m} = \frac{V}{V_m} \frac{\dot{V}_s + \dot{V}_{pm}}{V} = \frac{V}{V_m} \dot{\epsilon}_m^v = \left(\frac{1 + e}{1 + e_m} \right) \dot{\epsilon}_m^v \quad (1-17)$$

In the adopted elastoplastic framework, the strain rate tensor is split into its elastic ($\dot{\epsilon}^e$) and plastic ($\dot{\epsilon}^p$) strain components. In the context of a double porosity formulation, it is assumed that microstructural strains are purely volumetric and fully reversible [7]. Consequently, the elastic portion of the deformation in active clays is given by its micro ($\dot{\epsilon}_m^e$) and macro ($\dot{\epsilon}_M^e$) strain components, while the plastic component of strains only takes into account the structural changes occurring at the macrostructural domain ($\dot{\epsilon}_M^p$). Thus, Equation (1-12) can also be expressed, in terms of elastic and plastic strain components, as follows:

$$\dot{\epsilon} = \dot{\epsilon}^e + \dot{\epsilon}^p = (\dot{\epsilon}_m^e + \dot{\epsilon}_M^e) + \dot{\epsilon}_M^p \quad (1-18)$$

1.2.3 The local mass transfer mechanism

Hydraulic equilibrium between the two structural levels is not assumed, which leads to a local exchange of mass of water and air between micro- and macro-pores. In [8, 9], it was proposed that the pore-water transferred between microstructure and macrostructure (Γ^w) is proportional to the difference in micro (s_m) and macro (s_M) suctions, that is,

$$\Gamma^w = \gamma^w (s_m - s_M) \quad (1-19)$$

where suction in the β -structural medium, s_β , is defined as:

$$s_\beta = \max(P_{g\beta} - P_{l\beta}, 0) \quad (1-20)$$

where $P_{g\beta}$ and $P_{l\beta}$ are the gas and liquid pressures, respectively, in each pore domain. The leakage parameter, γ^w , is related to geometric characteristics of the porous media [8, 10]. If the gas mobility between the two continua is considered high enough to assume equilibrium between the gas pressure in both porous media, the water mass transfer given by Equation (1-19) is only driven by the difference between the liquid pressures in each structural level.

1.2.4 Balance equations

The compositional approach used in CODE_BRIGHT implies that the mass balance equations are established for the species (mineral, water and air) rather than for the phases (solid, liquid and gas) while the equation for the balance of internal energy is formulated for the porous medium as a whole. These equations, together with the constitutive laws, define the set of governing equations that describe the THM response of a large range of geotechnical materials and boundary conditions commonly found in practical engineering problems.

The general expressions for the mass balance of each species in each structural level, the balance of internal energy and the momentum balance for the porous medium are presented below. In those equations, $\frac{D_s(\bullet)}{Dt}$ represents the material derivative with respect to the solid phase. The main state variables (or unknowns) adopted in the formulation of these balance equations are shown in *Table 1.2*. A detailed mathematical description of the general balance equations for deformable porous media can be found in [5]. For further information on the mathematical development of such equations in the context of a double structure formulation, see [6, 11].

Table 1.2. Balance equations for a double porosity approach (in CODE_BRIGHT) and their unknowns

Balance equations	Unknowns
Solid mass balance	$\bar{\phi}_\beta$ - Pore-volume fractions
Water mass balance for macrostructure	P_{lM} - Liquid pressure at macro-structural level
Water mass balance for microstructure	P_{lm} - Liquid pressure at micro-structural level
Air mass balance for macrostructure	P_{gM} - Gas pressure at macro-structural level

EURAD Deliverable 7.10 – HITEC Modelling

Air mass balance for microstructure	P_{gm} - Gas pressure at micro-structural level
Balance of internal energy	T - Temperature
Momentum balance	$\dot{\mathbf{u}}$ - Solid velocity

The mass balance of solid

The mass balance of solid in a porous media characterized by the existence of two distinct pore domains is expressed as:

$$\frac{D_s \phi}{Dt} = \frac{D_s \bar{\phi}_m}{Dt} + \frac{D_s \bar{\phi}_M}{Dt} = \frac{(1 - \bar{\phi}_m - \bar{\phi}_M) D_s \rho_s}{\rho_s} + (1 - \bar{\phi}_m - \bar{\phi}_M) (\dot{\epsilon}_m^v + \dot{\epsilon}_M^v) \quad (1-21)$$

which relates the variation of porosity to the changes in solid density (ρ_s) and to the volumetric deformation at each structural level.

The mass balance of water

Water is present in soils in the liquid phase and/or as vapour in the gas phase. In double structure porous media, water is found both in macro- and micro-pores. Consequently, it is necessary to write a balance equation to account for the mass of macrostructural water, expressed as:

$$\frac{D_s (\theta_{lM}^w S_{lM} + \theta_{gM}^w S_{gM})}{Dt} \bar{\phi}_M + (\theta_{lM}^w S_{lM} + \theta_{gM}^w S_{gM}) \dot{\epsilon}_M^v + \nabla \cdot (\mathbf{j}'_{lM} + \mathbf{j}'_{gM}) = -\Gamma^w \quad (1-22)$$

and another one to consider the mass of water in micro-pores, whose simplified form is given as follows:

$$\begin{aligned} \frac{D_s (\theta_{lm}^w S_{lm} + \theta_{gm}^w S_{gm})}{Dt} \bar{\phi}_m + (\theta_{lm}^w S_{lm} + \theta_{gm}^w S_{gm}) \dot{\epsilon}_m^v \\ = \Gamma^w - (\theta_{lm}^w S_{lm} + \theta_{gm}^w S_{gm}) (1 - \phi) \frac{\dot{\rho}_s}{\rho_s} \end{aligned} \quad (1-23)$$

where \mathbf{j}'_{lM} and \mathbf{j}'_{gM} are the macrostructural fluxes of water in liquid and gas phases, respectively, respect to the solid skeleton. Γ^w is the local water exchange term that represents the hydraulic coupling between the two pore domains. In the current double structure formulation, a positive value of this term implies that differences in the local water potential lead to a water mass transfer from macro- to micro-pores, while a negative value means that the water exchange occurs in the opposite direction.

It is important to highlight that Equation (1-23) assumes that the water mobility through micro-pores is very low and, consequently, the microstructural water does not contribute to the advective flux [12]. Therefore, the divergence term of the advective flux in the mass balance of microstructural water can be neglected, that is, $\nabla \cdot (\mathbf{j}'_{lm} + \mathbf{j}'_{gm}) \approx \mathbf{0}$. This assumption allows the treatment of the liquid pressure at microstructural level (P_{lm}) as a history variable to be updated during the constitutive integration of stresses.

The mass balance of air

The mass balance of air present in macro-pores, as gas or dissolved in the liquid phase, is given by the following expression:

EURAD Deliverable 7.10 – HITEC Modelling

$$\frac{D_s(\theta_{lM}^a S_{lM} + \theta_{gM}^a S_{gM})}{Dt} \bar{\phi}_M + (\theta_{lM}^a S_{lM} + \theta_{gM}^a S_{gM}) \dot{\bar{\epsilon}}_M^v + \nabla \cdot (\mathbf{j}'_{lM} + \mathbf{j}'_{gM}) = -\Gamma^a \quad (1-24)$$

while the mass balance of air present in the microstructural domain, under the assumption of negligible gas mobility through micro-pores, can be written as:

$$\begin{aligned} \frac{D_s(\theta_{lm}^a S_{lm} + \theta_{gm}^a S_{gm})}{Dt} \bar{\phi}_m + (\theta_{lm}^a S_{lm} + \theta_{gm}^a S_{gm}) \dot{\bar{\epsilon}}_m^v \\ = \Gamma^a - (\theta_{lm}^a S_{lm} + \theta_{gm}^a S_{gm})(1 - \phi) \frac{\dot{\rho}_s}{\rho_s} \end{aligned} \quad (1-25)$$

If it is also assumed that there is local equilibrium between the pore-air pressures, the air mass transfer between micro- and macro-pores (Γ^a) can be neglected, that is, $\Gamma^a \approx 0$.

The balance of internal energy

The assumption of local thermal equilibrium between the phases implies that the equation for the internal energy balance is established for the porous medium as a whole by accounting for the energy stored in each phase. In the context of a double porosity approach, the energy balance equation is given by:

$$\begin{aligned} \frac{D_s(E_s \rho_s)}{Dt} (1 - \phi) + \frac{D_s(E_l \rho_{lm} S_{lm} + E_g \rho_{gm} S_{gm})}{Dt} \bar{\phi}_m + \frac{D_s(E_l \rho_{lM} S_{lM} + E_g \rho_{gM} S_{gM})}{Dt} \bar{\phi}_M \\ + (E_l \rho_{lm} S_{lm} + E_g \rho_{gm} S_{gm}) \dot{\bar{\epsilon}}_m^v + (E_l \rho_{lM} S_{lM} + E_g \rho_{gM} S_{gM}) \dot{\bar{\epsilon}}_M^v \\ + \nabla \cdot (\mathbf{i}_c + E_l \rho_{lM} \mathbf{q}_{lM} + E_g \rho_{gM} \mathbf{q}_{gM}) \\ = f^Q - (E_l \rho_{lm} S_{lm} + E_g \rho_{gm} S_{gm} - E_s \rho_s)(1 - \phi) \frac{\dot{\rho}_s}{\rho_s} \end{aligned} \quad (1-26)$$

where E_α is the specific internal energy of the α phase; f^Q is an internal/external energy supply per unit volume of soil; \mathbf{i}_c represents the heat flux by conduction through the porous medium and \mathbf{q}_{lM} , \mathbf{q}_{gM} are the macrostructural advective fluxes of the liquid and gas phases with respect to the solid phase, respectively. The energy transport by the fluid motion through the micro-pores has been neglected in Equation (1-26).

The balance of momentum

The balance of momentum reduces to the equilibrium of stresses in the porous medium. In the context of a double porosity formulation, the momentum equilibrium equation is expressed as follows:

$$\nabla \cdot \boldsymbol{\sigma}_t + (\rho_s(1 - \phi) + (\rho_{lm} S_{lm} + \rho_{gm} S_{gm}) \bar{\phi}_m + (\rho_{lM} S_{lM} + \rho_{gM} S_{gM}) \bar{\phi}_M) \mathbf{g} = \mathbf{0} \quad (1-27)$$

where $\boldsymbol{\sigma}_t$ is the total stress tensor and \mathbf{g} is the gravity vector. The vector of body forces, represented by the second term on the left-hand side of Equation (1-27), also takes into account the weight of the liquid and gas phases in both structural media.

EURAD Deliverable 7.10 – HITEC Modelling

1.2.5 Thermal and hydraulic constitutive equations

The mathematical formulation for solving THM problems also requires a set of constitutive equations that provides the coupling among the main thermal, hydraulic and mechanical phenomena that take place in geotechnical porous media. The THM constitutive equations relate the independent variables (the unknowns of the coupled THM problems) with the dependent ones (fluxes of liquid and gas phases, heat fluxes, degree of saturation, liquid and gas densities, stress tensor, etc.).

In the following, a brief description of the general expressions of the thermal and hydraulic constitutive laws used in the current double porosity model is presented. A detailed explanation of such equations can be found in [5] (for single porosity media) and in [6, 8, 11] (for multi-porosity media).

Thermal constitutive equations

Heat conduction through the soil (i_c) is driven by temperature gradients (∇T) and described by Fourier's law according to:

$$i_c = -\lambda \cdot \nabla T \quad (1-28)$$

where the global thermal conductivity of the porous medium (λ) is usually expressed as a function of the thermal conductivity of each phase in the soil (λ_α), porosity (ϕ) and degree of saturation (S_l), that is,

$$\lambda = f(\lambda_\alpha, \phi, S_l) \quad (1-29)$$

In double porosity media, the thermal conductivity becomes dependent not only on the water content in the two pore-structure domains but also on the pore volume fraction in each structural medium. Thus, the global thermal conductivity is evaluated in terms of an average degree of saturation (S_l), which is defined as:

$$S_l = \frac{\bar{\phi}_m}{\phi} S_{lm} + \frac{\bar{\phi}_M}{\phi} S_{lM} \quad (1-30)$$

Hydraulic constitutive equations

In the current double porosity approach, the volumetric advective fluxes are only formulated for the macrostructural domain since the liquid and gas advective fluxes through micro-pores have been neglected. Therefore, the generalized Darcy's law ($q_{\alpha M}$) for the α phase (liquid, l ; gas, g) in active clays can be expressed as:

$$q_{\alpha M} = -\mathbf{k}_M \frac{k_{r\alpha M}}{\mu_{\alpha M}} (\nabla P_{\alpha M} - \rho_{\alpha M} \mathbf{g}) \quad (1-31)$$

The intrinsic permeability tensor for the macrostructure, \mathbf{k}_M , only depends on its pore structure, according to the modified Kozeny-Carman equation:

EURAD Deliverable 7.10 – HITEC Modelling

$$\mathbf{k}_M = \mathbf{k}_{M,0} \frac{\bar{\phi}_M^3}{(1 - \bar{\phi}_M)^2} \frac{(1 - \bar{\phi}_{M,0})^2}{\bar{\phi}_{M,0}^3} \quad (1-32)$$

or, alternatively, by means of an empirical exponential expression:

$$\mathbf{k}_M = \mathbf{k}_{M,0} \cdot \exp\left(b(\bar{\phi}_M - \bar{\phi}_{M,0})\right) \quad (1-33)$$

In such relationships, $\bar{\phi}_{M,0}$ is the pore fraction for which the reference intrinsic permeability tensor $\mathbf{k}_{M,0}$ is set and b is a fitting parameter of the model.

The phase relative permeability, $k_{r\alpha,M}$, expresses the dependence of the hydraulic permeability on the degree of saturation of macrostructure. The decrease in the water permeability with the reduction of the liquid saturation in macro-pores is defined through the following exponential function:

$$k_{rl,M} = A_{rl} (S_{e,M})^{\lambda_{rl}} \quad (1-34)$$

where the effective degree of saturation of macrostructure, $S_{e,M}$, is defined by:

$$S_{e,M} = \frac{S_{lM} - S_{lr,M}}{S_{ls,M} - S_{lr,M}} \quad (1-35)$$

in which S_{lM} , $S_{lr,M}$, $S_{ls,M}$ are the current, the residual and the maximum degree of saturation of the macrostructure, respectively; A_{rl} , λ_{rl} are model parameters.

The dependence of the dynamic viscosities of fluid species in macro-pores ($\mu_{\alpha M}$) on temperature is also considered in the current THM formulation – see [6].

The water retention curve (WRC) of a porous medium relates its water content (or degree of saturation) to the pore-water potential (suction). Due to the assumption that micro-pores may be unsaturated, it is also necessary to define hydraulic constitutive laws for the microstructure by the definition of a WRC for this pore domain as well. In CODE_BRIGHT the water retention capacity of a porous medium is described by a modified van Genuchten law. In the current double structure formulation, this empirical relationship is defined for the β -structural medium as follows:

$$S_{e,\beta} = \left(1 + \left(\frac{P_{g\beta} - P_{l\beta}}{P}\right)^{\frac{1}{1-\lambda_{r\beta}}}\right)^{-\lambda_{r\beta}} \left(1 - \frac{P_{g\beta} - P_{l\beta}}{P_{d\beta}}\right)^{\lambda_{d\beta}} \quad (1-36)$$

in which the thermal effect on the WRC can be taken into account by means of the following relationship proposed in [13]:

$$P = P_0 \frac{\sigma(T)}{\sigma_0(T_0)} \quad (1-37)$$

where P and P_0 are model parameters related to the pore-air entry value at the current temperature (T) and at a reference temperature (T_0), respectively. Surface tension, σ (in N/m) is a function of

temperature and σ_0 is its value at the same temperature at which P_0 is measured. $\lambda_{r\beta}$ and $\lambda_{d\beta}$ are model parameters and $P_{d\beta}$ is the suction value at fully dry conditions. The main differences between the retention curves at each structural domain, i.e. the different pore-air entry pressures and desaturation rates, can be clearly observed in *Figure 1.3*. The water storage capacity of the whole porous medium can be determined by taking into account the water potential and the pore volume fractions in each structural domain.

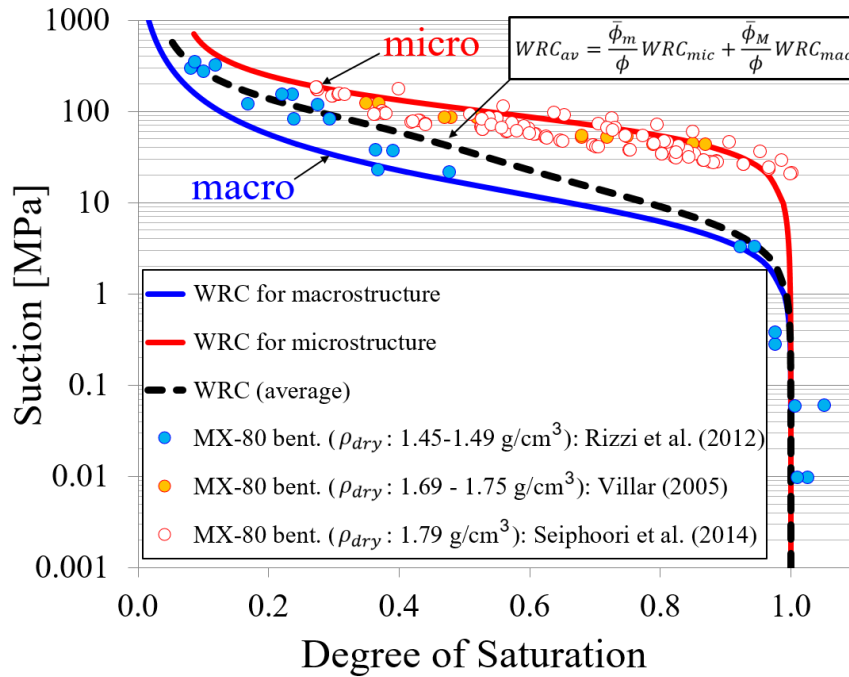


Figure 1.3: Water retention curves (WRC) for the macro- and micro-structural domains of compacted samples of MX-80 bentonite. Experimental data for the MX-80 bentonite at several dry densities from [14-16].

1.2.6 Mechanical constitutive equations

In this section, a brief description of the mechanical constitutive law developed in the current double porosity framework is presented. A more detailed presentation is provided in [6, 8, 11].

A direct consequence of assuming that the expansive clay incorporates two distinct but interacting continuum media is the possibility of establishing distinct stress-strain constitutive relationships for each structural level. The coupling between these two porous media is accomplished through mass transfer processes and strain coupling mechanisms that account for the component of macrostructural strains arising from the deformations that occur at particle level (microstructure).

The generalized stress-strain relationship for the β -structural domain can be expressed by:

$$\dot{\sigma}_{\beta} = [D_{\beta}] \dot{\epsilon}_{\beta} + \mathbf{h}_{l\beta} \dot{P}_{l\beta} + \mathbf{h}_{g\beta} \dot{P}_{g\beta} + \mathbf{h}_{T\beta} \dot{T} \quad (1-38)$$

where $\dot{\sigma}_{\beta}$ is the constitutive stress rate vector, $\dot{\epsilon}_{\beta}$ is the strain rate vector, $[D_{\beta}]$ is the constitutive stiffness matrix, $\mathbf{h}_{l\beta}$, $\mathbf{h}_{g\beta}$ are the generic constitutive vectors relating changes in liquid and gas pressures, respectively, to stress increments and $\mathbf{h}_{T\beta}$ is a constitutive vector relating stress to temperature changes.

EURAD Deliverable 7.10 – HITEC Modelling

As mentioned before, it is assumed that the macro-pore structure can be affected by the microstructural deformations [1, 8, 17]. Consequently, it is reasonable to define a macrostructural strain component that expresses such a mechanical coupling ($\dot{\boldsymbol{\epsilon}}_{m \rightarrow M}^e$). In contrast, it is assumed that the microstructural behaviour is not affected by the deformations of macrostructure. Moreover, the plastic changes in the soil fabric are attributed to the loading-collapse mechanism (LC mechanism) and to the micro-macro structural coupling mechanism (beta mechanism). The more relevant features of the elastic and the plastic behaviour described by the current double porosity model are briefly described below. More detailed information on the mechanical constitutive behaviour can be found in [6, 11].

Elastic behaviour

Taking into account the strain decomposition given in Equation (1-18), the elastic behaviour of the expansive soil is completely described by its microstructural and macrostructural strain components. In the context of THM analyses, the elastic strain component associated with microstructure, $\dot{\boldsymbol{\epsilon}}_m^e$, can be split into a hydro-mechanical component, $\dot{\boldsymbol{\epsilon}}_{m, HM}^e$, and a thermal component, $\dot{\boldsymbol{\epsilon}}_{m, \Delta T}^e$, as follows:

$$\dot{\boldsymbol{\epsilon}}_m^e = \dot{\boldsymbol{\epsilon}}_{m, HM}^e + \dot{\boldsymbol{\epsilon}}_{m, \Delta T}^e \quad (1-39)$$

where

$$\dot{\boldsymbol{\epsilon}}_{m, HM}^e = [\bar{\mathbf{D}}_m^e]^{-1} \dot{\boldsymbol{\sigma}}_m = [\bar{\mathbf{D}}_m^e]^{-1} \dot{\boldsymbol{\sigma}} + \frac{1}{3\bar{K}_m} \mathcal{H}(S_{lm}, P_{lm}, P_{gm}, T) \mathbf{m} \quad (1-40)$$

$$\dot{\boldsymbol{\epsilon}}_{m, \Delta T}^e = \left(\frac{1 + e_m}{1 + e} \right) \dot{\boldsymbol{\epsilon}}_{m, \Delta T}^e \quad (1-41)$$

In such expressions, $[\bar{\mathbf{D}}_m^e]$ and $\dot{\boldsymbol{\sigma}}_m$ are the elastic constitutive stiffness matrix and the generalized Bishop effective stress vector for the microstructure; \bar{K}_m is the volumetric elastic modulus of the microstructural medium; $\dot{\boldsymbol{\sigma}}$ is the net effective stress vector (for the soil); \mathcal{H} represents a non-linear function of temperature, the saturation and the fluid pressures in micro-pores; and $\mathbf{m} = [1 \ 1 \ 1 \ 0 \ 0 \ 0]^t$ is an auxiliary vector. Equation (1-17) is recalled in order to establish the relationship between the thermal component of the microstructural strain, $\dot{\boldsymbol{\epsilon}}_{m, \Delta T}^e$, and the elastic thermal expansion of the clay aggregate (actual microstructure), $\dot{\boldsymbol{\epsilon}}_{m, \Delta T}^e$, as given in Equation (1-41).

The elastic deformations of the solid skeleton (macrostructure), $\dot{\boldsymbol{\epsilon}}_M^e$, can be also described by means of a hydro-mechanical component, $\dot{\boldsymbol{\epsilon}}_{M, HM}^e$, and a thermal strain component, $\dot{\boldsymbol{\epsilon}}_{M, \Delta T}^e$:

$$\dot{\boldsymbol{\epsilon}}_M^e = \dot{\boldsymbol{\epsilon}}_{M, HM}^e + \dot{\boldsymbol{\epsilon}}_{M, \Delta T}^e \quad (1-42)$$

with

$$\dot{\boldsymbol{\epsilon}}_{M, HM}^e = [\bar{\mathbf{D}}_M^e]^{-1} \dot{\boldsymbol{\sigma}} + \frac{1}{3\bar{K}_S} \dot{s}_M \mathbf{m} + \dot{\boldsymbol{\epsilon}}_{m \rightarrow M, HM}^e \quad (1-43)$$

$$\dot{\boldsymbol{\epsilon}}_{M, \Delta T}^e = \dot{\boldsymbol{\epsilon}}_{m \rightarrow M, \Delta T}^e = \dot{\boldsymbol{\epsilon}}_{\Delta T}^e - \dot{\boldsymbol{\epsilon}}_{m, \Delta T}^e \quad (1-44)$$

EURAD Deliverable 7.10 – HITEC Modelling

where $[\bar{D}_M^e]$ is the elastic constitutive matrix for the macrostructure; \bar{K}_s is the volumetric elastic modulus related to changes in the macrostructural suction, \dot{s}_M ; $\dot{\epsilon}_{\Delta T}^e$ is the elastic thermal expansion of the soil (as a whole), defined as:

$$\dot{\epsilon}_{\Delta T}^e = \frac{1}{3K_T} \dot{T} \mathbf{m} \quad (1-45)$$

where K_T is the thermal bulk modulus of the porous medium. The assumption of fully reversible thermal strains in the mathematical formulation of the current double porosity model implies that the porous skeleton must undergo the same thermal expansion experienced by the solid particles (clay aggregates) when temperature changes [18]. In other words, $\dot{\epsilon}_{\Delta T}^e = \dot{\epsilon}_{m,\Delta T}^e$. Consequently, the macrostructural component of the elastic thermal strains in Equation (1-44) is given by:

$$\dot{\epsilon}_{M,\Delta T}^e = \bar{\phi}_M \dot{\epsilon}_{\Delta T}^e = \frac{\bar{\phi}_M}{3K_T} \dot{T} \mathbf{m} \quad (1-46)$$

The elastic bulk moduli, \bar{K}_M , \bar{K}_s and K_T , are defined by the following expressions:

$$\bar{K}_M = \frac{(1 + e_M)p}{\bar{\kappa}_M} \quad (1-47)$$

$$\bar{K}_s = \frac{(1 + e_M)(s_M + p_{atm})}{\bar{\kappa}_s} \quad (1-48)$$

$$K_T = \frac{1}{\alpha_0 + 2\alpha_2 \Delta T} \quad (1-49)$$

where p is the net mean effective stress, p_{atm} is the atmospheric pressure and $\bar{\kappa}_M$, $\bar{\kappa}_s$, α_0 and α_2 are model parameters. It is important to remark that the macro void ratio parameter in such expressions (e_M) is not equal to the macro void ratio defined in Equation (1-8). In Equation (1-47) and (1-48), e_M is estimated without taking into account the fraction of pores within the clay particles/aggregates, that is,

$$e_M = \frac{\bar{\phi}_M}{1 - \bar{\phi}_M} \quad (1-50)$$

The assumption of no fabric changes in the elastic range entails a geometrical restriction that links the elastic moduli of microstructure (\bar{K}_m) and macrostructure (\bar{K}_M). This coupling between the elastic parameters leads to the following relationships:

$$K = K_m = \left(\frac{1 + e}{1 + e_m} \right) \bar{K}_m \quad (1-51)$$

$$K = \bar{\phi}_M \bar{K}_M \quad (1-52)$$

EURAD Deliverable 7.10 – HITEC Modelling

$$\bar{K}_m = \left(\frac{e - e_m}{1 + e_m} \right) \bar{K}_M \quad (1-53)$$

where K and K_m are the bulk moduli of the soil and of the clay aggregate, respectively.

Plastic Loading-Collapse (LC) mechanism

The plastic loading-collapse (LC) mechanism of the double porosity formulation is fully defined by the same set of equations and parameters that describe the single porosity, thermo-elastoplastic Barcelona Basic Model (BBM). A complete description of the evolution of the yield surface in the stress space and its dependence on the stress state, history variables and (macro) suction can be found in [6, 8, 11, 17]. Only the main mathematical ingredients characterizing this plastic mechanism are given below.

The yield surface for a general state, expressed in terms of the stress invariants (p, J, θ), is expressed by:

$$F_{LC} = 3J^2 - M_F^2 \left(\frac{g_F(\theta, \alpha_F)}{g_F\left(-\frac{\pi}{6}, \alpha_F\right)} \right)^2 (p + p_s)(p_0 - p) = 0 \quad (1-54)$$

where M_F is the slope of the critical state line, g_F is a function of Lode's angle (θ), α_F is a model parameter and p_s expresses the dependence of the shear strength on macro suction and temperature [19], according to:

$$p_s = p_{s0} + k_s s_M \cdot \exp(-\rho_T \Delta T) \quad (1-55)$$

where p_{s0} is the tensile strength in saturated conditions; k_s and ρ_T are model parameters that computes the dependence of p_s on the macro suction and temperature, respectively. The apparent non-saturated pre-consolidation pressure (p_0), that defines the locus of activation of irreversible deformations due to loading increments or macrostructural collapse, is given by:

$$p_0 = p_c \left(\frac{p_{0,T}^*}{p_c} \right)^{\frac{\lambda_{(0)} - \bar{\kappa}_M}{\lambda_{(s_M)} - \bar{\kappa}_M}} \quad (1-56)$$

where:

$$p_{0,T}^* = p_0^* + 2(\alpha_1 \Delta T + \alpha_3 \Delta T |\Delta T|) \quad (1-57)$$

$$\lambda_{(s_M)} = \lambda_{(0)} [r + (1 + r) \cdot \exp(-\beta s_M)] \quad (1-58)$$

where $\lambda_{(0)}$ and $\lambda_{(s_M)}$ is the macrostructural compressibility at saturated conditions and for a given macro suction, s_M , respectively; p_0^* is the pre-consolidation pressure at saturation and p_c is a reference pressure. α_1 and α_3 are model parameters that control the size of the yielding surface for a temperature increment (ΔT); r and β are model parameters that expresses the dependence of the size and evolution

of the LC curve on the macro suction. A three-dimensional representation of the BBM yield surface is given in *Figure 1.4*.

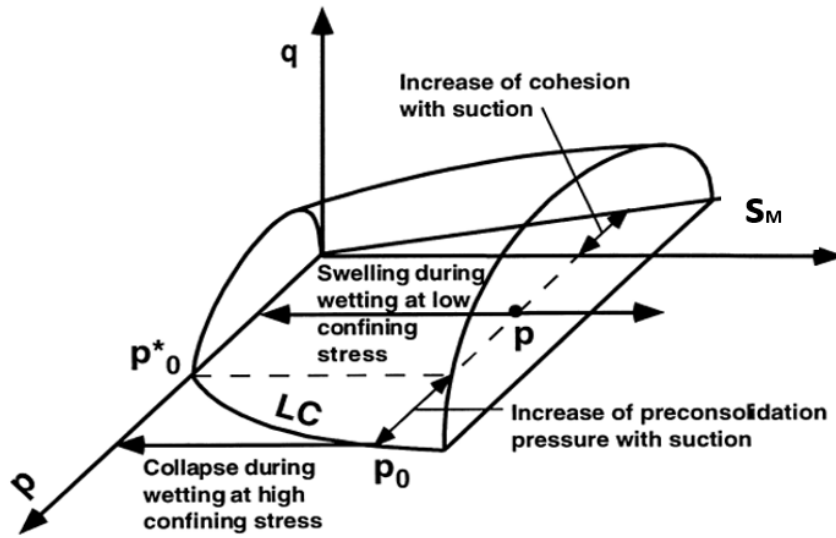


Figure 1.4: Three-dimensional representation of the BBM yield surface (modified from [17]).

The generation of macrostructural plastic deformations when the LC mechanism is activated is governed by the plastic flow rule, which is given by the following expression:

$$\dot{\epsilon}_{M,LC}^p = \dot{\lambda}_{LC} \frac{\partial G_{LC}}{\partial \sigma} \quad (1-59)$$

where the magnitude of the plastic deformation rate is determined by the scalar plastic multiplier, $\dot{\lambda}_{LC}$. The plastic potential function of the LC mechanism, G_{LC} , is expressed as:

$$G_{LC} = \omega \cdot 3J^2 - M_F^2 \left(\frac{g_F(\theta, \alpha_G)}{g_F\left(-\frac{\pi}{6}, \alpha_G\right)} \right)^2 (p + p_s)(p_0 - p) = 0 \quad (1-60)$$

in which ω is the non-associativity parameter. When ω is equal to 1, plastic flow becomes associated.

Plastic Beta mechanism

It has been assumed that microstructural behaviour is not affected by the macrostructural state. However, the volumetric deformations of microstructure may induce plastic strains at the macrostructural level [1]. The magnitude of these macrostructural deformations ($\dot{\epsilon}_{M,beta}^p$) is taken as proportional to the microstructural elastic strains [1, 7, 17]:

$$\dot{\epsilon}_{M,beta}^p = f_{beta} \dot{\epsilon}_m^e \quad (1-61)$$

EURAD Deliverable 7.10 – HITEC Modelling

where f_{beta} represents a pair of micro-macro coupling functions that distinguishes between the stress paths characterized by a **microstructural contraction** (MC paths) and those paths in which a **microstructural swelling** (MS paths) occurs. The following general expression has been used in the current double porosity approach:

$$f_{beta} = \begin{cases} f_{MC}^{(1)} + (f_{MC}^{(0)} - f_{MC}^{(1)})(1 - \mu_{\beta})^{n_{MC}} & \text{if } \dot{p}_m > 0 \\ f_{MS}^{(1)} + (f_{MS}^{(0)} - f_{MS}^{(1)})(1 - \mu_{\beta})^{n_{MS}} & \text{if } \dot{p}_m < 0 \end{cases} \quad (1-62)$$

where μ_{β} is a parameter that accounts for the degree of compactness of macrostructure and \dot{p}_m is the rate of the mean effective stress at the microstructural domain. $f_{MC}^{(0)}$, $f_{MC}^{(1)}$, n_{MC} and $f_{MS}^{(0)}$, $f_{MS}^{(1)}$, n_{MS} are model parameters that define the coupling function in MC paths and MS paths, respectively. A general representation of the micro-macro coupling functions, including the main behaviour features expected during wetting and drying paths are shown in *Figure 1.5*.

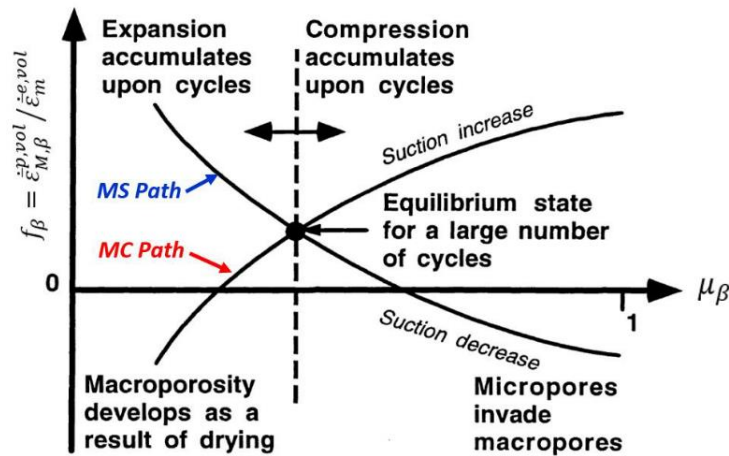


Figure 1.5: Structural coupling functions for the micro-macro coupling mechanism [17].

A modification of Equation (1-61) has been proposed in order to ensure the simplifying assumption of elastic thermal deformations at both structural levels in non-isothermal analyses. In such conditions, the thermal expansion of microstructure does not generate any irreversible structural changes (such as thermal collapse) in the soil skeleton. Consequently, the thermal component of the microstructural deformations must be discounted from the total microstructural strains:

$$\dot{\boldsymbol{\epsilon}}_{M,beta}^p = f_{beta}(\dot{\boldsymbol{\epsilon}}_m^e - \dot{\boldsymbol{\epsilon}}_{m,\Delta T}^e) \quad (1-63)$$

When isothermal analyses are performed, $\dot{\boldsymbol{\epsilon}}_{m,\Delta T}^e = \mathbf{0}$, and Equation (1-61) is recovered.

Hardening rule

The hardening of the double porosity medium is given by the evolution of the isotropic yield stress due to the contribution of both plastic mechanisms considered in the current formulation. Thus, the evolution

EURAD Deliverable 7.10 – HITEC Modelling

of the saturated pre-consolidation pressure (the hardening parameter of this model), \dot{p}_0^* , is given as follows:

$$\dot{p}_0^* = p_0^* \left(\frac{1 + e_M}{\lambda_{(0)} - \bar{\kappa}_M} \right) (\dot{\epsilon}_{M,LC}^{p,v} + \dot{\epsilon}_{M,beta}^{p,v}) \quad (1-64)$$

where $\dot{\epsilon}_{M,LC}^{p,v}$ is the volumetric plastic strain generated by the yielding of macrostructure due to the LC mechanism and $\dot{\epsilon}_{M,beta}^{p,v}$ is the volumetric component of macrostructural strains due to the plastic β -mechanism.

In non-isothermal problems, the evolution of this hardening parameter, $\dot{p}_{0,T}^*$, can also become dependent on the temperature changes. In such conditions, the general expression for the hardening rule of the double structure model is given as follows:

$$\dot{p}_{0,T}^* = p_{0,T}^* \left(\frac{1 + e_M}{\lambda_{(0)} - \bar{\kappa}_M} \right) (\dot{\epsilon}_{M,LC}^{p,v} + \dot{\epsilon}_{M,beta}^{p,v}) + 2(\alpha_1 \pm 2\alpha_3 \Delta T) \dot{T} \quad (1-65)$$

1.3 Benchmark application

The formulation and constitutive models outlined above are intended to be applied to the analysis of a benchmark involving the long-term heating (with temperatures up to 140°C) and hydration of a column of granular bentonite. The corresponding experiment was performed by CIEMAT and it engages the main coupled THM phenomena that are incorporated in the formulation developed. This experiment has been selected as a for T3.3 benchmark in cooperation with DONUT [17].

A number of modelling tasks are described in the following sub-sections. These tasks refer to the definition of the Finite Element mesh and boundary and initial conditions (1.3.2), and the determination of the model parameters required for THM constitutive laws considered in the mathematical formulation (1.3.3). The following subsection presents the modelling results and associated discussion (1.3.4). A summary description of the benchmark is first presented for completeness (1.3.1).

1.3.1 Description of the benchmark

The test was performed on a 50 cm-long column of bentonite pellets, hydrated through the top surface and heated through the bottom surface (*Figure 1.6*). The body of the cell consisted of four cylindrical elements made out of Teflon PTFE (thermal conductivity 0.25 W/m·K) to prevent as much as possible lateral heat loss. The cell was wrapped with a 5-mm thick dense foam insulation to further reduce heat loss (thermal conductivity 0.04 W/m·K). The insulation of the bottom 5 cm of the column was enhanced after 1518 hours of heating by the addition of a 30-mm thick insulation wool layer (Superwool 607 HT) blanket (thermal conductivity 0.04 W/m·K) and a 25-mm thick ISOVER BT-LV blanket (thermal conductivity 0.034 W/m·K). The nominal internal diameter of the cell was 7 cm and the inner length 50 cm. Those are, therefore, the dimensions of the specimen column.

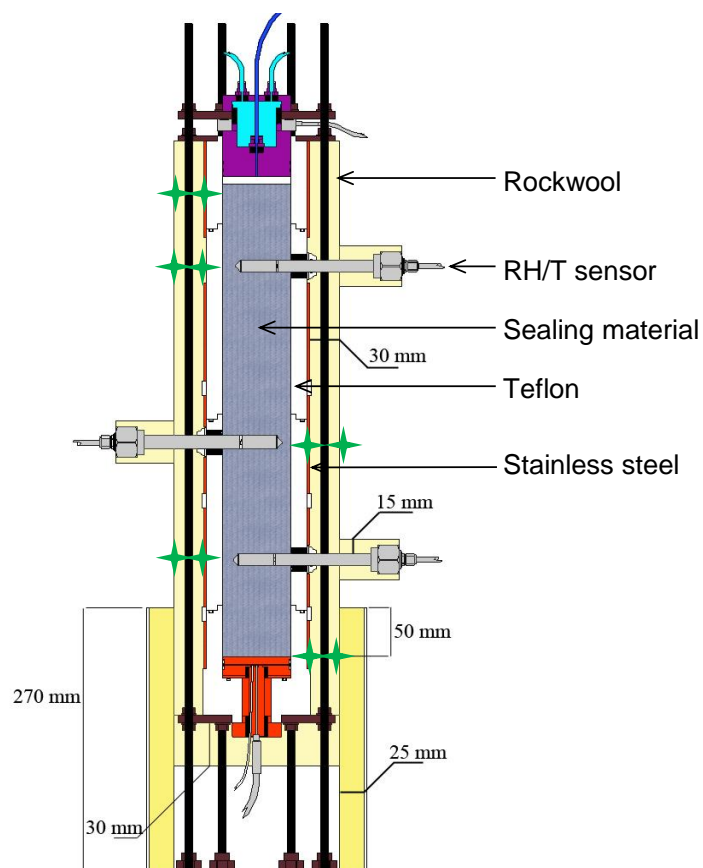


Figure 1.6: Layout of the benchmark column experiment.

After the cell was filled with the bentonite sealing material, its walls were perforated for the installation of capacitive-type sensors placed in the axis of the column at three different vertical levels (10, 22 and 40 cm from the heater) to measure relative humidity (RH) and temperature (T) inside the bentonite. The water intake (in weight), the heater power, the axial pressure and the relative humidity (RH) and temperature (T) at three different levels inside the bentonite were continuously measured during the test.

The material used in the experiment was made up of MX-80 bentonite pellets, the same material used in a section of the HE-E experiment carried out in the Mont Terri laboratory. The as-received water content of the material was 6.4%. The aspect of the material and the grading curve obtained by dry sieving in the CIEMAT laboratory are shown in *Figure 1.7*. It was also reported that 69% of pores were larger than 200 nm [20]. In the context of a double porosity approach, this pore fraction could be considered as the initial macro-pore volume fraction for the constitutive model described in Section 1.2. Therefore, the initial micro- and macro-pore volume fractions used in the modelling of the current benchmark were 0.159 and 0.285, respectively. The initial total porosity was estimated at 0.444.

EURAD Deliverable 7.10 – HITEC Modelling

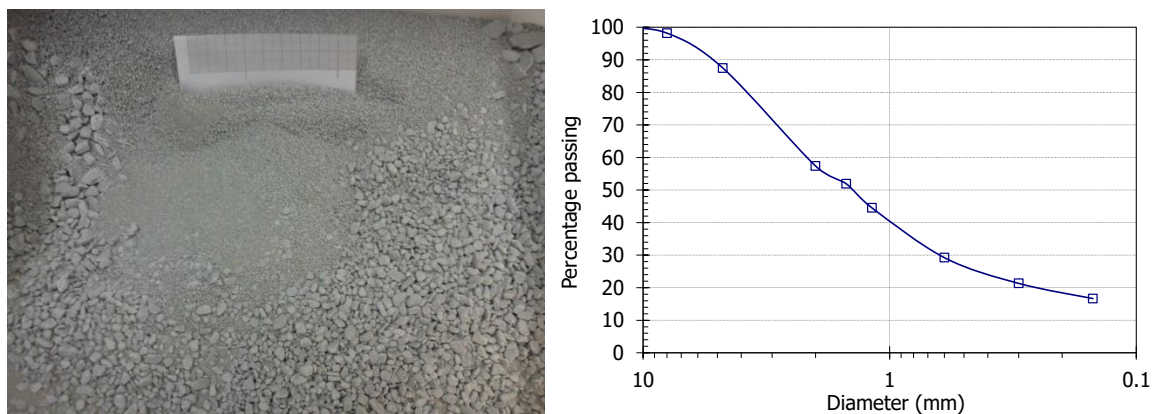


Figure 1.7: MX-80 bentonite pellets used in the experiment (left) and grading curve of the MX-80 pellets obtained by dry sieving (right).

The column was built by filling the cell in seven equal layers. Between the bentonite and the upper lid, a porous stone was placed. This assembly was weighed and afterwards the holes for the insertion of the sensors were drilled into the granulate material through the Teflon walls. The assembly was weighed again in order to record how much material had been lost as a consequence of drilling. In this way, the initial characteristics of the column could be obtained (Table 1.3). Figure 1.8 shows a view of the column realization and the cell in its final configuration before and after being wrapped with the insulating material.

Table 1.3: Main characteristics of the granular bentonite column after installation

Initial water content (%)	6.4
Sample mass (g)	3094
Sample mass after drilling (g)	3076
Volume of sensors (cm ³)	20
Theoretical dry mass (g)	2891
Diameter (mm)	70.0
Height (mm)	483.9
Dry density (g/cm ³)	1.53
Porosity	0.444
Void ratio	0.797
Degree of saturation (%)	22

EURAD Deliverable 7.10 – HITEC Modelling

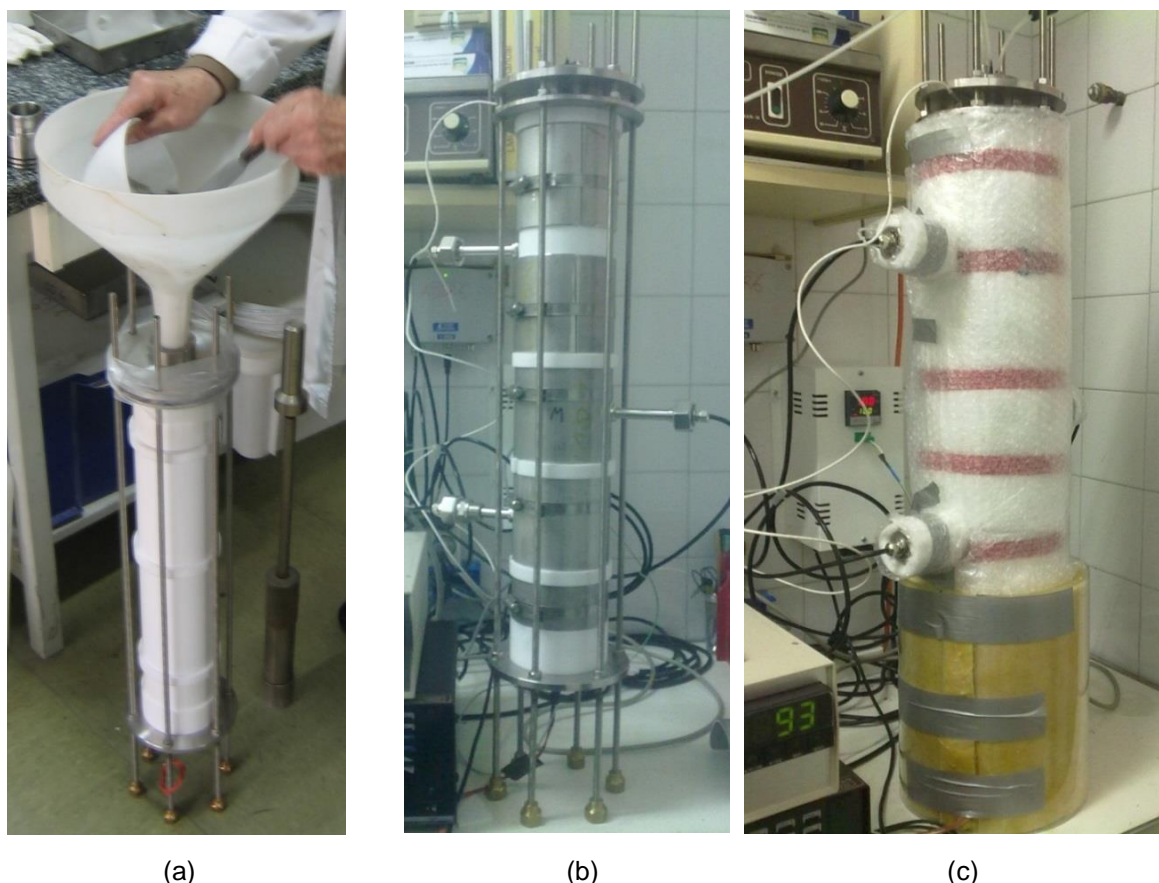


Figure 1.8: (a) Pouring the pellets inside the cell; (b) View of the assembled column; (c) View of the column after installing the thermal insulation.

The first stage of the test involved heating but no hydration. The heating started on 22/11/2011, a date that was considered as the initial time ($t=0$) of the experiment. After 33 minutes the first target temperature of 100°C was reached. On 17/4/2012, after the observations of relative humidity throughout the column had stabilised, the temperature was increased in 17 minutes to 140°C. The improvement of the thermal insulation system was performed between these two heating episodes in order to minimize the lateral heat losses through the cell wall. Due to that, it was observed an increase of temperature measured by the sensors installed inside the column, especially in the sensor closer to the heater (see *Figure 1.9*). On 18/6/2012 hydration started while maintaining the heater temperature to 140°C. Hydration was performed by applying a constant water height of 60 cm on the top surface of the specimen. The thermal and hydraulic conditions have been kept constant since then. *Figure 1.10* shows the laboratory temperature, heater power and temperature at 10 cm from the heater during the hydration stage of the test. It can be observed that there were fluctuations (mainly seasonal) in the laboratory temperature that affected somewhat the temperatures in the column. The power required to maintain a constant temperature in the heater was affected as well.

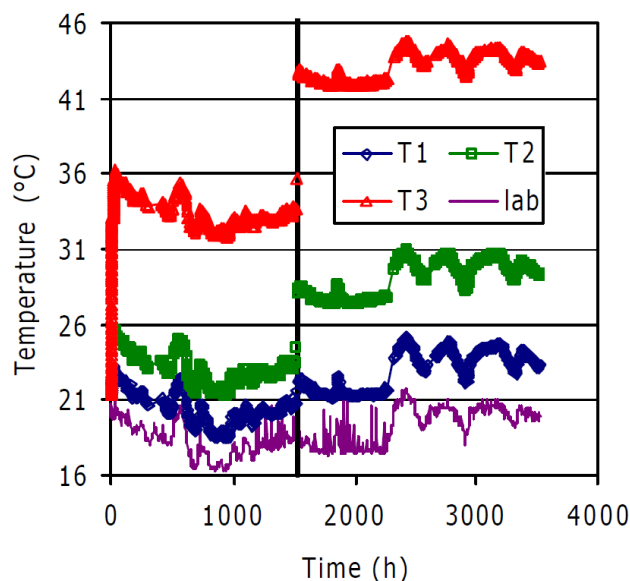


Figure 1.9: Temperature changes due to the improvement of the external insulation system. The thick vertical line indicate the reinforcement of the thermal isolation system [21].

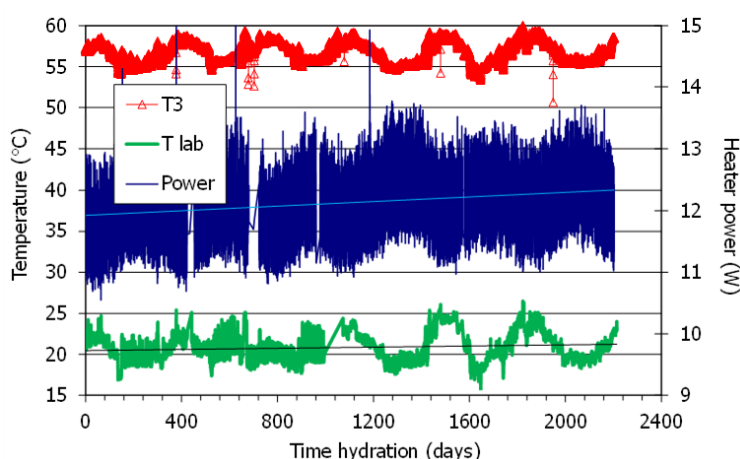


Figure 1.10: Laboratory temperature, heater power and temperature at 10 cm from the heater (T3) during the hydration stage of the test [20].

Hydration of the heated column continued for almost 10 years. Then, water injection line was closed, the heater was switched off and the cell was dismantled in November 2021. A detailed description of the sequence of activities carried out in the laboratory after the end of hydration and the start of the dismantling of the bentonite column are found in [20]. Several 2 cm high sampling sections were recovered and small samples were taken from the disassembled column in order to evaluate the final state of the bentonite material in terms of its water content and dry density distribution. These sampling sections were separated by sawing or with knives, depending on their consistency. The upper portion of the bentonite column was dark, cohesive and with homogeneous appearance, which reflected the high water content in this area. In the middle portion of the column, the material was also dark in colour and coherent. However, a progressive loss of consistency and lighter colour of the material was observed towards the heater. The material near the heater (up to a distance of 10 cm from it) was completely loose. The weight and volume of each sampling section were measured once they were separated, which allowed the estimation of the bulk density along the column.

EURAD Deliverable 7.10 – HITEC Modelling

The water content distribution was estimated from the mass of water contained in each small sample as the difference between the mass of the sample before and after its oven drying at 110 °C for 48 hours. The mass of the dry sample and the volume occupied by it prior to oven drying were used to determine its dry density. The volume of the small sample was estimated by weighing the mercury displaced when the sample was immersed in it. The distributions of water content and dry density along the column at the end of the experiment are shown in *Figure 1.11*.

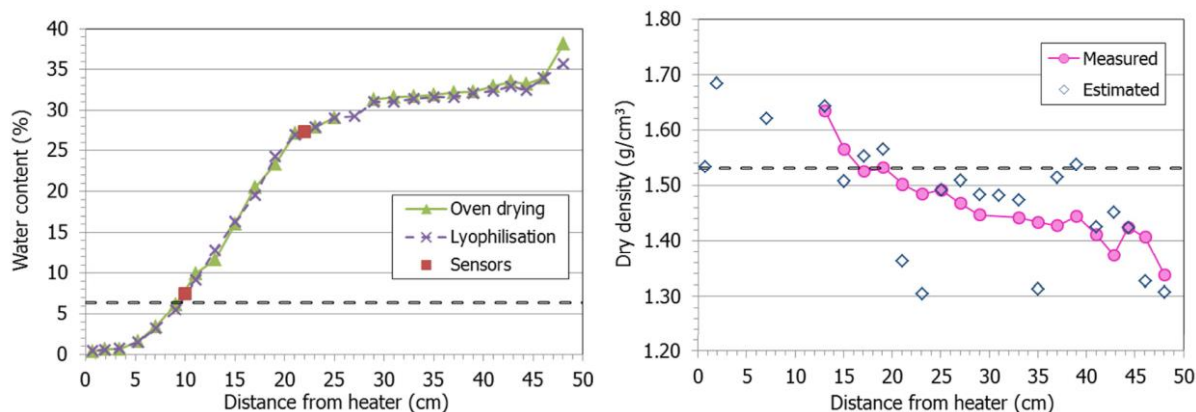


Figure 1.11: Final water content (left) and dry density (right) distribution along the bentonite column. The dotted horizontal lines represents the initial values [20].

As expected, the values measured in laboratory indicated a general trend of saturation of the upper portion of the column while the portion closest to the heater remained very dry due to the high temperatures applied in the experiment. Moreover, the volumetric expansion induced by the artificial re-saturation of the mass of pellets near the hydration system led to a gradual compression of the underlying bentonite layers. Therefore, an increase in dry density was observed in the unsaturated portion of the column (the lower 20 cm) while values lower than the initial dry density were estimated for the material in the saturated portion of the column. Additional information on the dismantling and sampling operations, the methodology employed to estimate the water content and dry density of the small samples and the evaluation of the final state of the bentonite column are presented in [20].

The following results were requested from the numerical analysis:

- Evolution of temperatures in the three sensors from time $t=0$ to the end of the test (the laboratory temperature fluctuations could be disregarded).
- Evolution of relative humidity in three locations from time $t=0$ to the end of the test.
- Evolution of water intake from time $t=0$ to the end of the test.
- Evolution of axial pressure from time $t=0$ to the end of the test.
- Distributions of dry density, water content and degree of saturation along the column at the end of the test (from dismantling data)

1.3.2 Model domain and boundary conditions

Heating and hydration of the bentonite column was modelled by means of a finite element (FE) analysis using CODE_BRIGHT [3]. A structured FE mesh comprising 700 linear quadrilaterals was generated as illustrated in *Figure 1.12(a)*. The lower horizontal boundary simulated the heating element while the upper horizontal boundary represented the hydration system. The body of the cell (made of Teflon PTFE) and the thick layer of dense foam provided the external isolation of the cell during the first stage of heating. The improvement of the thermal isolation of the bentonite column with the replacement of the dense foam by a thick layer of insulation wool, performed between the first and the second heating

EURAD Deliverable 7.10 – HITEC Modelling

episodes, was also taken into account. The modelled geometries before and after the enhancement of the external insulation system are shown in *Figure 1.12(b)*. All dimensions were ascribed in accordance to the test dimensions specified in [21]. The initial conditions assumed in the calculations for the bentonite material are shown in *Table 1.4*.

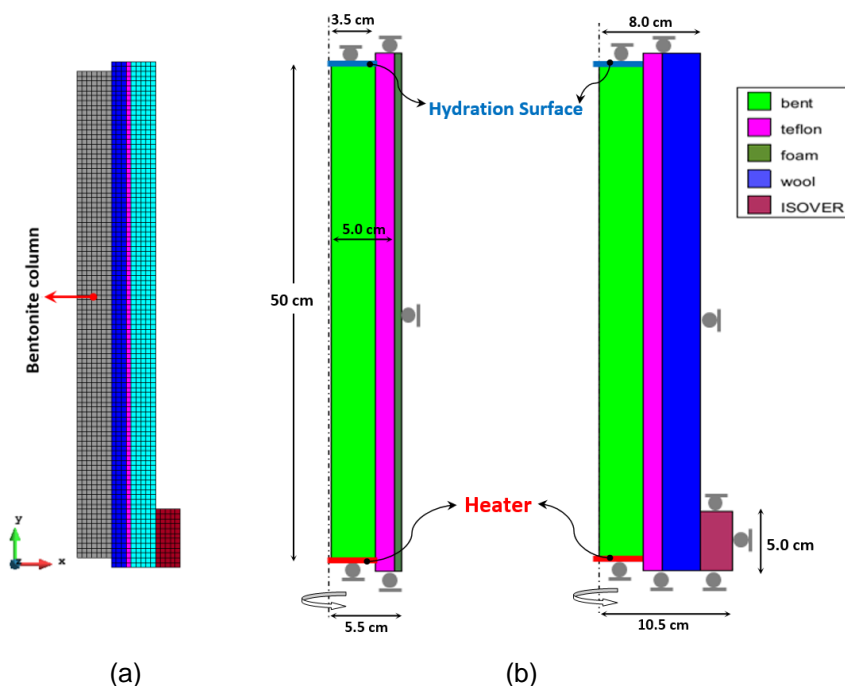


Figure 1.12: (a) Finite element mesh generated to simulate the large bentonite cell; (b) modelled domain of the bentonite column before (left) and after (right) the reinforcement of the external insulation system.

Table 1.4: Initial conditions for the MX-80 bentonite pellets

Initial conditions (numerical modelling)	Unit	Value
Temperature, T_0	[°C]	22
Suction (macrostructure), s_M	[MPa]	123
Suction (microstructure), s_m	[MPa]	123
Confining stress (isotropic conditions)	[MPa]	0.1
Total porosity, ϕ_0	-	0.44
Micro-pore volume fraction, $\bar{\phi}_{m,0}$	-	0.16

Heating was simulated by prescribing the corresponding temperature at the bottom of the cell. A null-flux condition was applied on the upper boundary of the column (the hydration line) prior to the beginning of the infiltration phase of the experiment. No vertical displacements were allowed along the upper and the lower horizontal boundaries of the bentonite column. Furthermore, displacements were also restricted at the external vertical boundaries so that heating and the re-saturation of the bentonite column was modelled under constant overall volume conditions. Hydration was simulated via a constant liquid pressure of 0.006 MPa (0.06 bar) applied on the upper horizontal boundary of the column of pellets. This flux condition was kept invariable throughout the analysis. The stages followed during the test and the applied thermal and hydraulic loads are schematized in *Figure 1.13*.

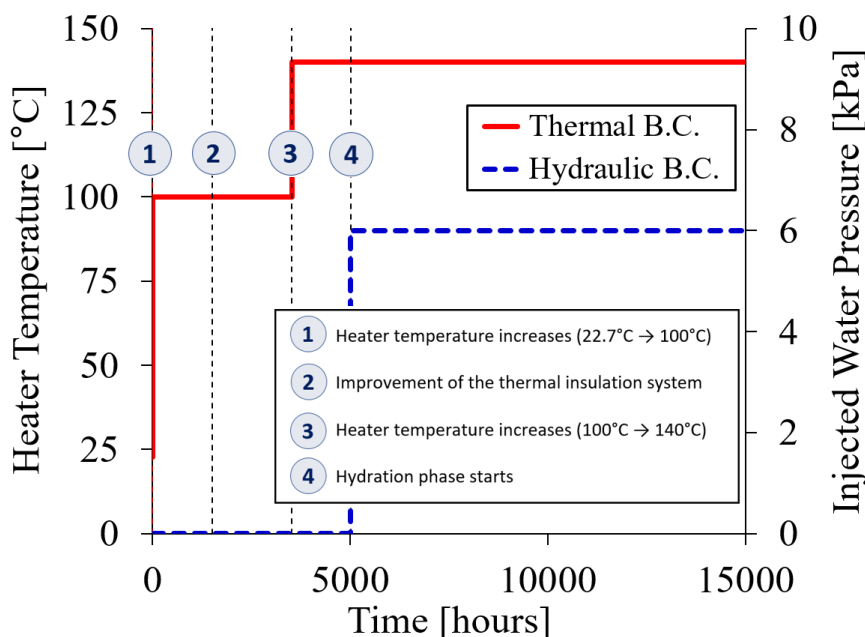


Figure 1.13: Thermo-hydraulic boundary conditions applied during the infiltration test. Time=0 corresponds to the beginning of heating.

1.3.3 Thermal, hydraulic and mechanical parameters

The thermal parameters adopted in the numerical simulations are listed in *Table 1.5*. They are derived from experimental data reported in the literature [21-26]. The variation of thermal conductivity with degree of saturation is shown in *Figure 1.14*. It was assumed that these physical properties remain constant in the temperature range of the experiment (22°C – 140°C).

Table 1.5: Thermal parameters

Heat conductivity		
Thermal conduct. of the dry soil, λ_{dry}	[W m ⁻¹ K ⁻¹]	0.35
Thermal conduct. of the saturated soil, λ_{sat}	[W m ⁻¹ K ⁻¹]	1.30
Thermal Expansion		
Linear thermal expansion for grains	[°C ⁻¹]	2.5e-05
Volum. thermal expansion for water (at 40°C)	[°C ⁻¹]	-3.4e-04
Volum. thermal expansion for the medium	[°C ⁻¹]	7.5e-05
Solid phase specific heat		[J kg ⁻¹ K ⁻¹]
		893

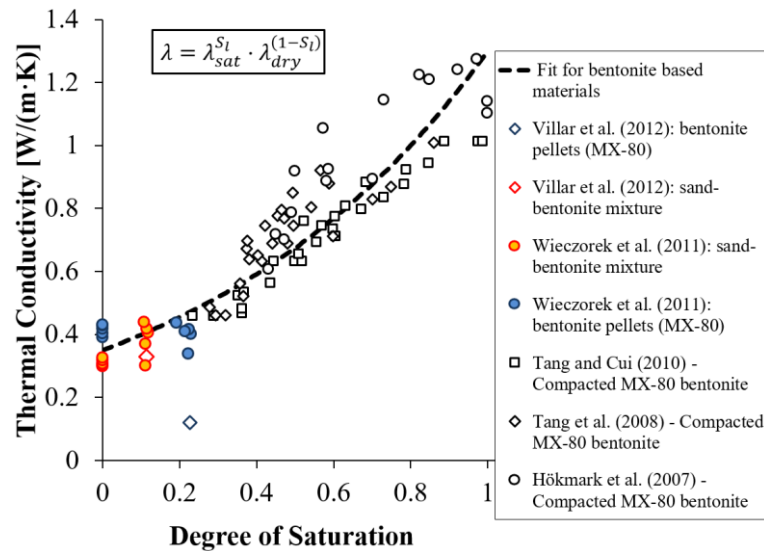


Figure 1.14: Variation of thermal conductivity with degree of saturation. Experimental data collected from [21, 23-26].

The macrostructural pore-water retention curve of the granular bentonite material was calibrated from the data provided by small oedometer tests, in which compacted granular MX-80 bentonite materials were submitted to controlled wetting or drying paths at different temperatures [15]. The model parameters presented in Table 1.6 adjust these experimental data to a water retention function expressed by the modified van Genuchten law, see Equation (1-36) and Figure 1.15(a).

The same modified van Genuchten law was also used to model the microstructural retention curves, but due to the lack of more specific information about the water retention capacity of micro-pores in MX-80 bentonites, such curves were defined by assuming a high value for the air entry parameter. This assumption was related to the pore-water retention behaviour of denser clay fabrics, where micro-pores are the predominant pore-size fraction present in high-density specimens [9]. The shape of the water retention capacity of micro-pores, obtained from the model parameters listed in Table 1.6, is shown in Figure 1.15(b) together with some experimental water retention data for bentonite samples compacted at high dry densities (in the range 1.69 – 1.79 g/cm³).

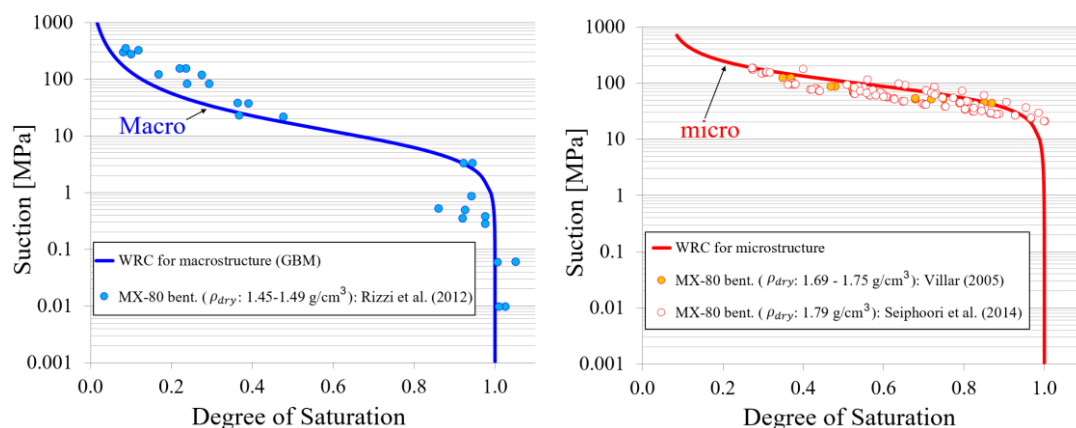


Figure 1.15: Water retention curves for macrostructure (left) and microstructure (right) of MX-80 pellets. Symbols represent experimental results (from [14-16]) and full lines correspond to the granular bentonite retention curves used in the modelling of the benchmark.

Table 1.6: Model parameters for the retention curves

Retention curve parameters for macrostructure		
Input Parameter (description)	Unit	Value
Measured P at 20°C, P_0	[MPa]	8.0
Surface tension at 20°C, σ_0	[N/m]	0.072
Shape function for retention curve, λ_{rM}	-	0.45
Pressure related with the suction at zero degree of saturation, P_{dM}	[MPa]	1500
Model parameter, λ_{dM}	-	1.0
Residual saturation, $S_{lr,M}$	-	0.01
Maximum saturation, $S_{ls,M}$	-	1.00
Retention curve parameters for microstructure		
Input Parameter (description)	Unit	Value
Measured P at 20°C, P_0	[MPa]	80
Surface tension at 20°C, σ_0	[N/m]	0.072
Shape function for retention curve, λ_{rm}	-	0.60
Pressure related with the suction at zero degree of saturation, P_{dm}	[MPa]	2000
Model parameter, λ_{dm}	-	2.0
Residual saturation, $S_{lr,m}$	-	0.07
Maximum saturation, $S_{ls,m}$	-	1.00

The dependence of intrinsic permeability on the pore structure of the granular expansive materials was modelled using Kozeny's law, Equation (1-32). In the double-porosity approach, such an intrinsic permeability variation is considered dependent on the macro-pore volume fraction ($\bar{\phi}_M$) instead of the total porosity (ϕ). The increase in the hydraulic permeability with saturation was modelled as a power function of the degree of saturation (see Equation (1-34)). The adopted parameters for the water flux through macro-pores are given in Table 1.7.

Table 1.7: Hydraulic parameters for the advective water flow in the macrostructure

Input Parameter (description)	Unit	Value
Intrinsic permeability, $k_{M,0}$	[m ²]	4.50e-19
Reference porosity, $\bar{\phi}_{M,0}$	-	0.29
Constant parameter (for relative permeability), A_{rl}	-	1.0
Power parameter (for relative permeability), λ_{rl}	-	10

The parameter for the local water mass transfer between the two families of pores (γ^w , see Equation (1-19)) is in principle related to properties of the microstructural medium (e.g. aggregate size, specific surface and inter-layer permeability of the clay particles). Due to the difficulty to characterize in detail the microstructure of the granular bentonite, the leakage coefficient used in the numerical calculations was estimated from back-analysis calibrations. Several values for the local water transfer coefficient were considered in the modelling tasks. However, the value taken for this parameter in the calculations presented in Section 1.3.4 was in the range $1.0 \times 10^{-9} - 1.0 \times 10^{-8}$ kg/s/m³/MPa.

EURAD Deliverable 7.10 – HITEC Modelling

The mechanical parameters for the bentonite pellets were taken from experimental data obtained in the mechanical characterization of bentonite mixtures with similar composition and dry density ranges. However, some of those parameters had to be calibrated during the modelling of the HE-E experiment [27] to fit the model predictions to the data recorded by the sensors installed in the *in situ* experiment and in the laboratory heating tests. The main input mechanical parameters used in the numerical calculations are listed in *Table 1.8*, *Table 1.9* and *Table 1.10*.

Table 1.8: Main elastic parameters for the bentonite material (MX-80 pellets).

Elastic behaviour		
Input Parameter (description)	Unit	Value
Elastic slope for specific volume – mean stress, $\bar{\kappa}_M$	-	2.0e-3
Elastic slope for specific volume – macro suction, $\bar{\kappa}_S$	-	1.0e-2
Poisson's ratio, ν	-	0.30
Bulk thermal modulus for the soil, K_T	[°C]	4.0e4
Parameter for elastic thermal strain, α_0	[°C ⁻¹]	0.0
Parameter for elastic thermal strain, α_2	[°C ⁻²]	0.0

Table 1.9: Model parameters for the elastoplastic behaviour (LC mechanism) of the MX-80 pellets.

Elastoplastic behaviour (loading-collapse mechanism)		
Slope of void ratio – mean stress at saturation, $\lambda_{(0)}$	-	0.17
Parameter defining the maximum soil stiffness, r	-	0.80
Parameter controlling the rate of increase of stiffness with macro suction, β	[MPa ⁻¹]	0.05
Reference pressure, p_c	[MPa]	0.09
Initial pre-consolidation mean stress at saturation, p_0^*	[MPa]	0.7 – 1.0
Tensile strength in saturated conditions, p_{s0}	[MPa]	0.10
Parameter related to the increase of tensile strength due to macro suction, k_s	-	0.10
Parameter of decrease in tensile strength due to ΔT , ρ_T	-	0.0
Parameter for plastic thermal strain, α_1	[MPa·°C ⁻¹]	0.0
Parameter for plastic thermal strain, α_3	[MPa·°C ⁻²]	0.0
Friction angle, φ	[°]	27
Smoothed shape parameter, α_F	-	8
Smoothed shape parameter, α_G	-	8
Non-associativity parameter, ω	-	1.0

Table 1.10: Parameters for the coupling functions (see Figure 1.16)

Parameter	Unit	Value
$f_{MS}^{(0)}$	-	0.5
$f_{MS}^{(1)}$	-	0.0
n_{MS}	-	3.0
$f_{MC}^{(0)}$	-	-0.1
$f_{MC}^{(1)}$	-	1.0
n_{MC}	-	3.0

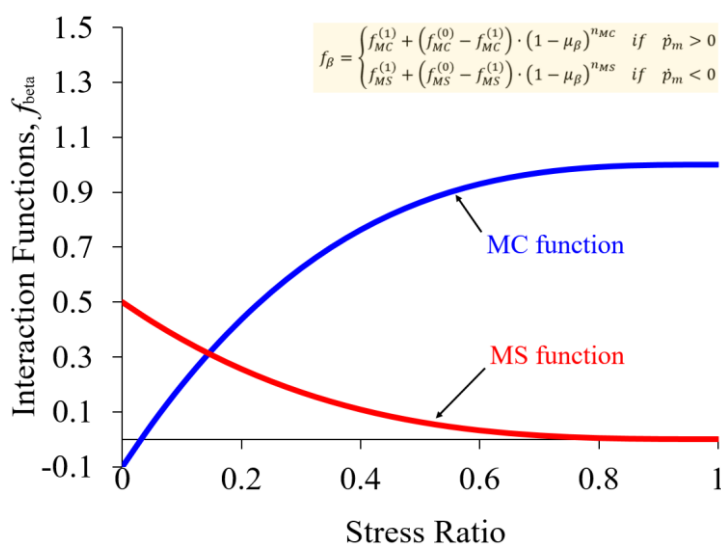


Figure 1.16: Coupling functions used in the numerical modelling.

1.3.4 Modelling results and discussion

The reproduction of the evolution of temperature and relative humidity (RH) in the early stages of the test using the double porosity model can be observed in *Figure 1.17* and *Figure 1.18* where distances are taken from the bottom of the cell. The numerical results and experimental data showed in these plots correspond to the heating phase that took place before the beginning of hydration. It can be noted the good agreement between the numerical and the measured data especially at the sensors closer to the heater. Temperature oscillations recorded by the sensors are associated with the changes in the laboratory temperature [28] and were not incorporated into the model.

EURAD Deliverable 7.10 – HITEC Modelling

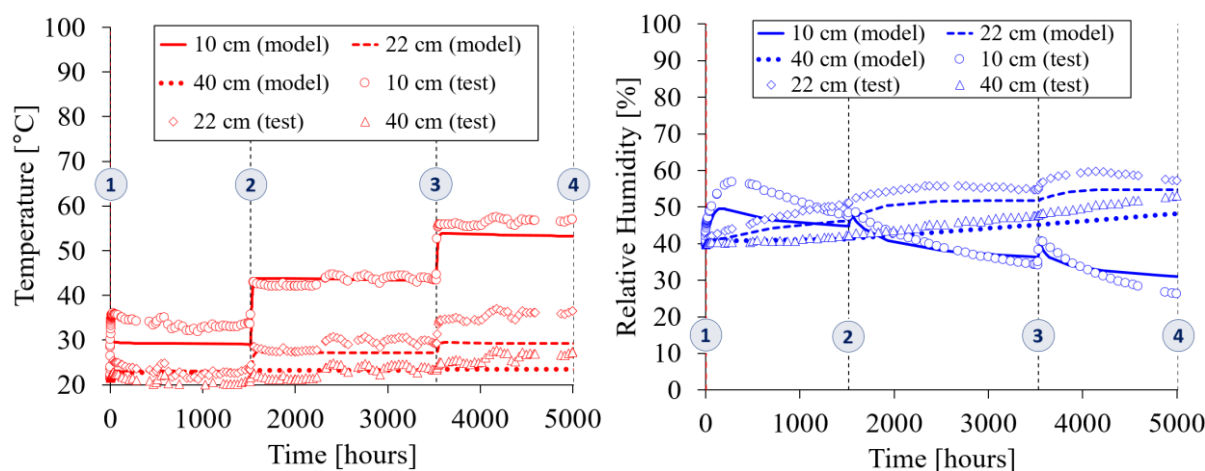


Figure 1.17: Evolution of temperature (left) and RH (right) up to 5000 hours of heating (before the start of hydration).

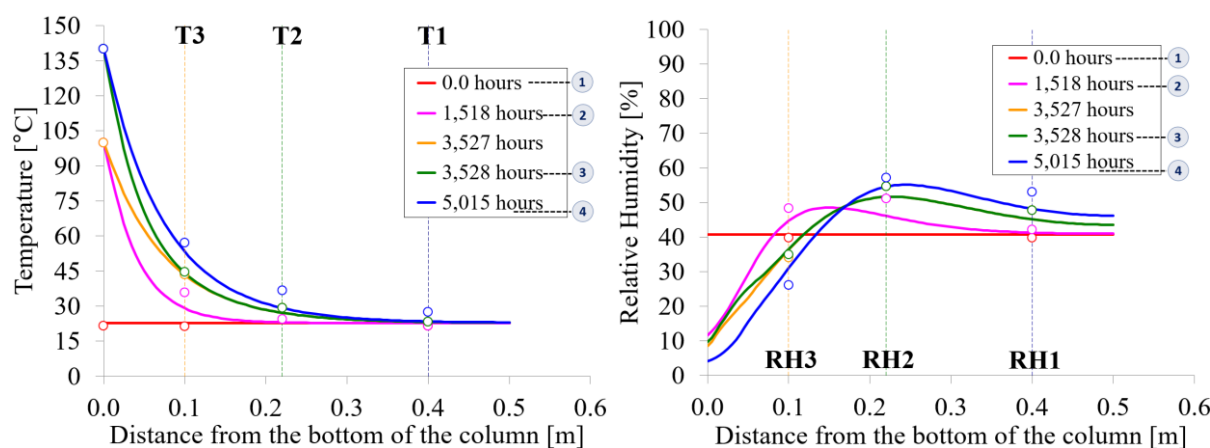


Figure 1.18: Distribution of temperature (left) and RH (right) along the column of pellets for several times (before the start of hydration).

The changes in temperature occurred during the heating without hydration are related to the increments in temperature caused by the heat propagation from the bottom towards the top of the column and by the improvement of the insulation system. The model also predicted the initial increase of RH at the sensor close to the heater due to vapour migration. The initial dry state of the bentonite pellets and associated low thermal conductivity induced a high thermal gradient in the 20 cm closest to the heater. Therefore, the humidity registered in the sensor at 10 cm from the heater decreased due to evaporation and the subsequent vapour diffusion to the upper portion of the column. The local RH gradually increased at the sensors further from the heater (at 22 and 40 cm) due to the condensation of vapour coming from the bottom of the cell. This is the result of properly considering in the formulation the water phase changes and the diffusion of vapour from the hotter to the cooler zones inside the column.

The amount of water injected into the column during the controlled hydration of the heated bentonite column is shown in Figure 1.19. It can be observed that modeling provides an accurate representation of the water intake. The evolution and some profiles of temperature and RH obtained from the numerical calculations are plotted in Figure 1.20 and Figure 1.21 together with the laboratory measurements during the early stages of hydration. Once hydration has started, the upper portion of the bentonite column experienced a sudden saturation due to the downward flux of liquid water, which is reflected in the marked increase of RH in the sensors at 22 cm and 40 cm from the heater. Also in this case, the comparison between observations and modelling results were satisfactory.

EURAD Deliverable 7.10 – HITEC Modelling

The evolution of axial pressure at the top of the bentonite column arising from the application of the thermo-hydraulic load under confined conditions is shown in *Figure 1.22*. The evolution of the axial pressure was mostly related to the expansion of the bentonite pellets due to hydration. The model predictions for the swelling behaviour fitted quite well the laboratory data measured during the early stages of hydration. It should be stated, however, that, the leakage parameter controlling the local transfer of mass of water between micro and macro-pores (γ^w) was calibrated taking into account the early evolution of the axial pressure, since the swelling behaviour is strongly affected by the changes of the water content at microstructural level which, in turn, is controlled by the leakage parameter.

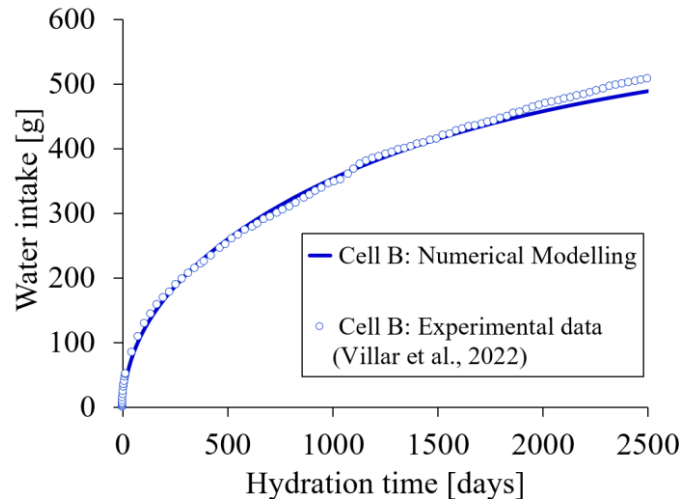


Figure 1.19: Water intake during the hydration phase of the test.

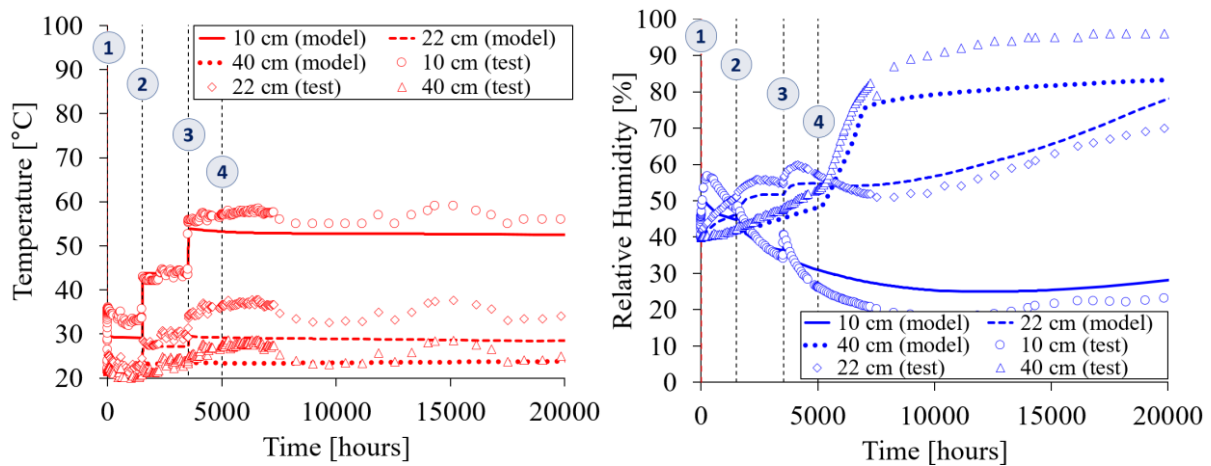


Figure 1.20: Evolution of temperature (left) and RH (right) until 20000 hours of heating (15000 hours of hydration).

EURAD Deliverable 7.10 – HITEC Modelling

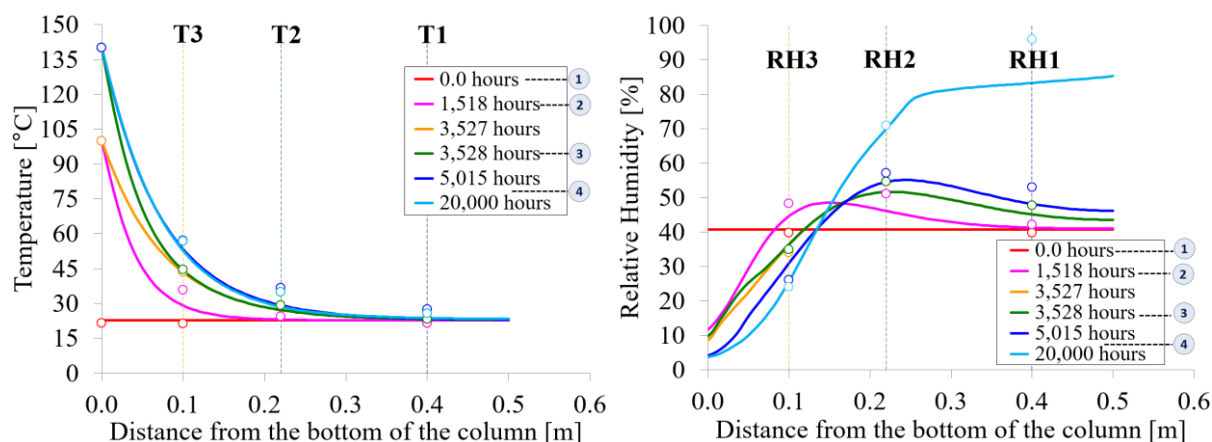


Figure 1.21: Distribution of temperature (left) and RH (right) along the column of pellets for several times (up to the first 15000 hours of hydration).

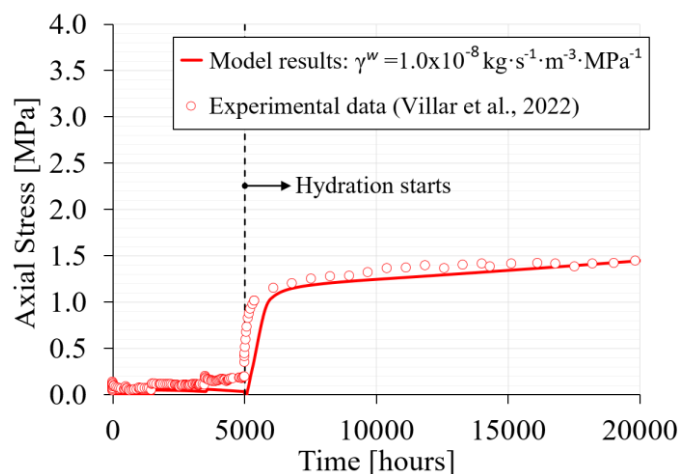


Figure 1.22: Evolution of the axial stress at the top of the column of pellets (up to 15000 hours of hydration).

As the infiltration test progressed, the saturation front continued to move downward, the water content increased in all the sensor positions and the macro and micro suctions decreased, as can be seen in *Figure 1.23* and *Figure 1.24*. The average suction (or saturation) in the expansive material was estimated from the retention curves of the macrostructure and the microstructure taking into account the pore volume fraction of each structural medium.

The saturation state along the column of pellets at the end of the infiltration test is plotted in *Figure 1.25*. The saturation in the surroundings of the sensor at 10 cm from the heater shows the influence of the high thermal gradient close to the heater. It can be noted that the laboratory measurements indicated that the bentonite material was still quite dry while the model overestimated the saturation state at the end of the test of the bentonite in the lower half of the column. The swelling of the bentonite material in the upper layers of the column may have a large impact on the final density state of the heated material located in the middle portion of the column, as indicated by the dry density distribution at the end of the test (see *Figure 1.26*). A considerable reduction of macro-porosity could lead to a decrease in the mobility of macrostructural water in the lower half of the column and, consequently, to a reduction in the water content in both pore levels. It should be noted that the evolution of the saturation of macro-pores is governed by the water permeability while the evolution of the saturation of micro-pores is due to the local water mass transfer controlled by the leakage parameter.

EURAD Deliverable 7.10 – HITEC Modelling

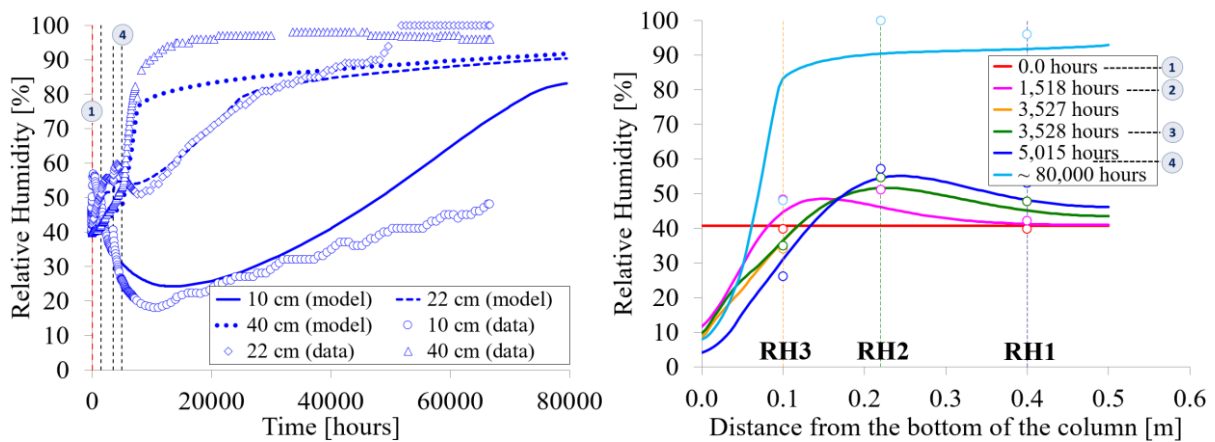


Figure 1.23: Evolution (left) and longitudinal profiles (right) of RH until the end of the test

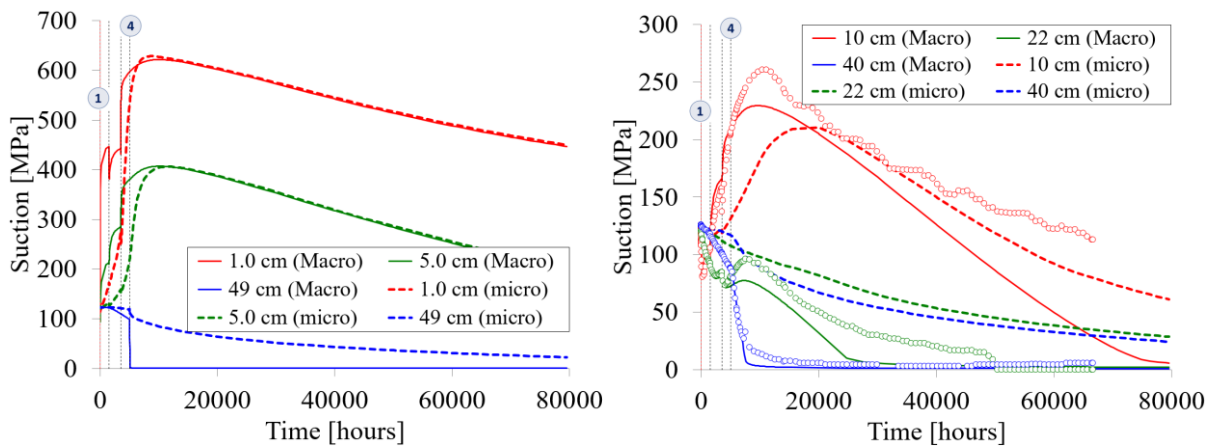


Figure 1.24: Evolution of macro and micro suction at 1 cm, 5 cm and 49 cm (left) and at 10 cm, 22 cm and 40 cm (right) from the heater until the end of the test. Symbols represent the average suction estimated by the psychrometric relationships from the data provided by the RH sensors.

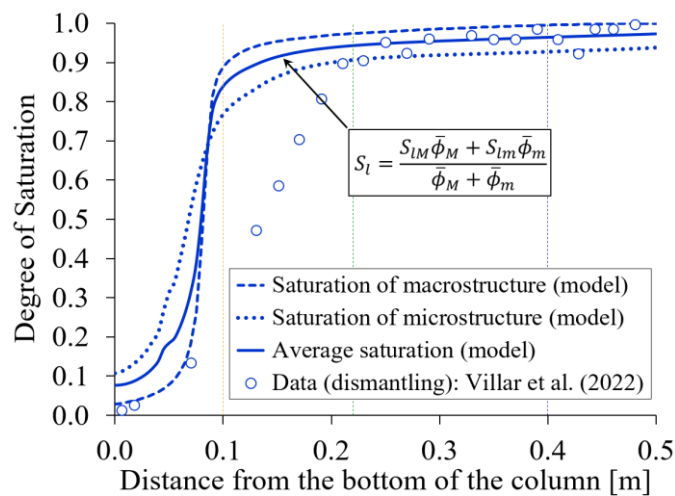


Figure 1.25: Saturation profile along the column of pellets at the end of the test. Symbols represent the experimental data obtained in the post-mortem analyses [20].

EURAD Deliverable 7.10 – HITEC Modelling

The numerical simulation using the current model predicted a very limited reduction of the dry density close to the hydration end, see *Figure 1.26*; this local reduction was in fact much smaller than the actual density changes measured at the end of the test. Incidentally, the peak in the model distribution of dry density close to the heater is a numerical artefact caused by relatively coarse calculation finite element mesh with no physical significance.

The progressive evolution of the axial stress at the top of the bentonite column until the end of hydration is shown in *Figure 1.27*. The overestimation of the magnitude of the axial pressure in the later stages of hydration could be affected by the development of lateral friction between the saturated bentonite material and the cell body, a feature that was not considered in the numerical simulations. However, when a lower value for the local water transfer parameter has been used, i.e., when the re-saturation of microstructure is delayed, the difference between the model predictions and the laboratory measurements became very small, as shown in *Figure 1.27* for $\gamma^w = 10^{-9} \text{ kg}\cdot\text{s}^{-1}\cdot\text{m}^{-3}\cdot\text{MPa}^{-1}$ (model results in dashed line).

Some complementary constitutive analyses with the same THM model parameters and initial conditions adopted in the benchmark were performed in order to estimate the swelling response of the bentonite material when hydrated under isothermal conditions. The swelling pressure obtained from such constitutive analyses was about 4 MPa (see *Figure 1.28*). This value is in close agreement with the experimental data for this type of bentonite material at similar dry density values (1.45 – 1.55 g/cm³).

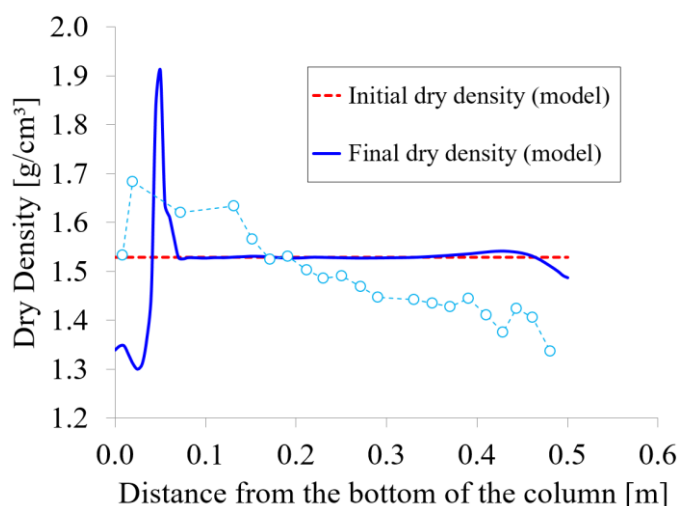


Figure 1.26: Dry density profile along the column of pellets at the end of the infiltration test. Symbols represent the experimental data obtained from the post-mortem observations [20].

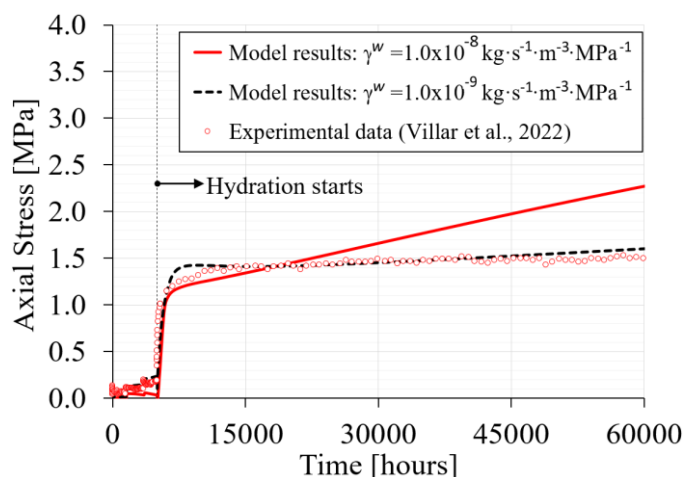


Figure 1.27: Evolution of the axial stress at the top of the column of pellets until the end of the test. Model results are given for two different macro-micro water exchange parameter values.

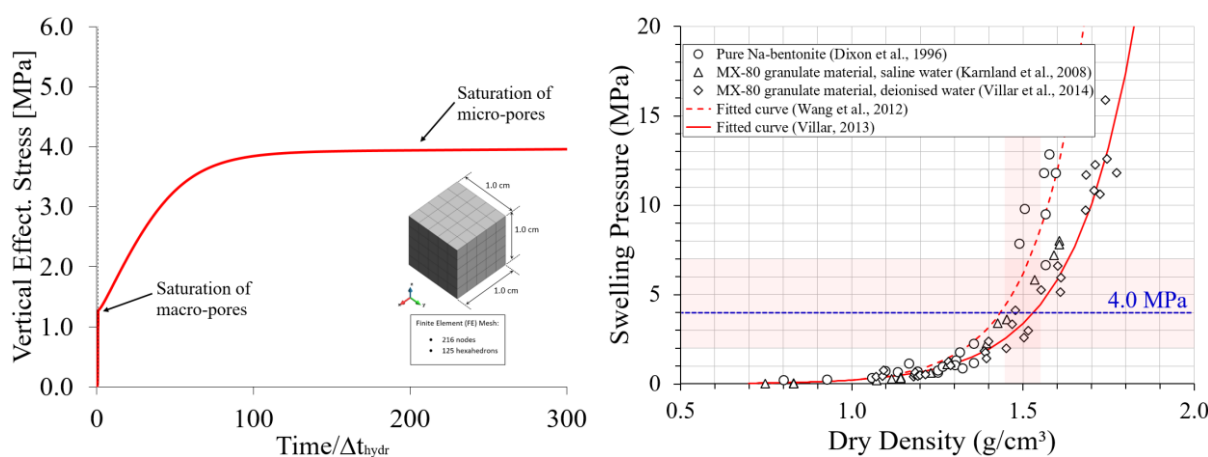


Figure 1.28: Model results from the constitutive analysis using the same input parameters considered in the benchmark (left) and experimental data (from [29-33]) relating the swelling pressure to dry density values (right).

1.3.5 Concluding Remarks

The formulation and constitutive models used in the simulations incorporated a number of relevant processes observed in the laboratory test such as heat conduction, water phase changes, vapour diffusion, differential thermal expansion of the solid and the liquid phases and swelling behaviour induced by thermo-hydraulic actions. Despite some limited departures of the measured data from the model results, it can be concluded that, by and large, the numerical formulation and the elastoplastic constitutive model based on a double structure approach described in Section 1.2 predicted satisfactorily the evolution of temperature, RH, water intake and axial stress during the whole duration of the test; larger discrepancies, however, were observed regarding the final state of the column.

The performance of back-calculation analyses and the calibration of some parameters controlling the re-saturation of macro-pores (by the advective flux of water) and micro-pores (by the local water mass exchange), the development of swelling pressure and the evolution of the clay fabric showed that the modelling of the transient hydration under thermal and hydraulic gradients remains a complex issue. Further calibration of some model parameters and improvement of the constitutive model to include other features such as the dependence of the water retention curves on the evolution of the pore volume

EURAD Deliverable 7.10 – HITEC Modelling

fractions in micro and macro media, may be necessary to achieve a closer fit of the model results to the final experimental observations.

1.4 References

- [1] Gens, A. & Alonso, E. E., 1992. A framework for the behaviour of unsaturated expansive clays, *Canadian Geotechnical Journal*, 29, pp. 1013–1032.
- [2] Mašín, D. & Khalili, N., 2016. Swelling phenomena and effective stress in compacted expansive clays, *Canadian Geotechnical Journal*, 53 (1), pp. 134-147.
- [3] Olivella, S., Gens, A., Carrera, J. & Alonso, E.E., 1996. Numerical formulation for a simulator (CODE_BRIGHT) for the coupled analysis of saline media, *Engineering Computations*, 13 (7), pp. 87-112.
- [4] Olivella, S., Carrera, J., Gens, A. & Alonso, E.E., 1994. Non-isothermal multiphase flow of brine and gas through saline media, *Transport in Porous Media*, 15, pp. 271-293.
- [5] Olivella, S., 1995. Nonisothermal multiphase flow of brine and gas through saline media. PhD Thesis, Technical University of Catalonia. Barcelona, Spain.
- [6] Vasconcelos, R., 2021. A double-porosity formulation for the THM behaviour of bentonite-based materials. PhD Thesis, Technical University of Catalonia. Barcelona, Spain
- [7] Sánchez, M., Gens, A., Guimarães, L. do N. & Olivella, S., 2005. A double structure generalized plasticity model for expansive materials, *International journal for numerical and analytical methods in geomechanics*, (January 2004), pp. 751–787. doi: 10.1002/nag.434.
- [8] Sánchez, M., 2004. Thermo-hydro-mechanical coupled analysis in low permeability media. PhD Thesis, Technical University of Catalonia. Barcelona, Spain.
- [9] Gens, A., Valleján, B., Sánchez, M., Imbert, C., Villar, M.V. & Van Geet, M., 2011. Hydromechanical behaviour of a heterogeneous compacted soil: experimental observations and modelling, *Géotechnique*, (5), pp. 367–386. doi: 10.1680/geot.SIP11.P.015.
- [10] Alonso, E. E. & Navarro, V., 2005. Microstructural model for delayed deformation of clay: loading history effects, *Canadian Geotechnical Journal*, 42, pp. 381-392.
- [11] Ruiz, D., 2020. Hydro-mechanical analysis of expansive clays constitutive and numerical modelling. PhD Thesis, Technical University of Catalonia. Barcelona, Spain.
- [12] Romero, E., 1999. Characterisation and thermo-hydro-mechanical behaviour of unsaturated Boom Clay: an experimental study. PhD Thesis, Technical University of Catalonia. Barcelona, Spain.
- [13] Olivella, S. & Gens, A., 2000. Vapour transport in low permeability unsaturated soils with capillary effects, *Transport in Porous Media*, 40, pp. 219-241.
- [14] Villar, M.V. (2005). MX-80 bentonite. Thermo-hydro-mechanical characterisation performed at CIEMAT in the context of the Prototype Project. CIEMAT Technical Report 1053. Madrid, Spain.
- [15] Rizzi, M., Seiphoori, A., Ferrari, A., Ceresetti, D. & Laloui, L., 2012. Analysis of the behaviour of granular MX-80 bentonite in THM processes. *Nagra-Aktennotiz AN 12-102*. Wettingen, Switzerland.
- [16] Seiphoori, A., Ferrari, A. and Laloui, L. (2014). Water retention behaviour and microstructural evolution of MX-80 bentonite during wetting and drying cycles. *Géotechnique*, 64, No. 9, pp. 721-734.
- [17] Alonso, E. E., Vaunat, J. & Gens, A., 1999. Modelling the mechanical behaviour of expansive clays, *Engineering Geology*, 54, pp. 173–183.
- [18] Khalili, N., Uchaipichat, A. & Javadi, A.A., 2010. Skeletal thermal expansion coefficient and thermo-hydro-mechanical constitutive relations for saturated homogeneous porous media, *Mechanics of Materials*, 42, pp. 593-598.

EURAD Deliverable 7.10 – HITEC Modelling

- [19] Gens, A., 1995. Constitutive laws. In: Modern issues in non-saturated soils. Edited by A. Gens, P. Jouanna & B. Schrefler. Springer-Verlag. pp. 129-158.
- [20] Villar, M.V., Iglesias, R.J. and Gutiérrez-Álvarez, C. (2022). Project HITEC: Dismantling of a THM column cell with MX-80 pellets simulating the HE-E in situ experiment. CIEMAT Technical Report CIEMAT/DMA/2G222/1/22. Madrid, Spain.
- [21] Villar, M.V., Martín, P.L., Gómez-Espina, R., Romero, F.J. and Barcala, J.M. (2012). THM cells for the HE-E test: setup and first results. PEBS Report D2.2-7.1. CIEMAT Technical Report CIEMAT/DMA/2G210/02/2012. Madrid, Spain.
- [22] Hökmark, H. (2004). Hydration of the bentonite buffer in a KBS-3 repository. Applied Clay Science, 26, 219-233.
- [23] Hökmark, H., Ledesma, A., Lassabatere, T., Fälth, B., Börgesson, L., Robinet, J.C., Sellali, N. and Sémété, P. (2007). Modelling heat and moisture transport in the ANDRA/SKB temperature buffer test. Physics and Chemistry of the Earth, 32, pp. 753-766.
- [24] Tang, A.M., Cui, Y.J., Le, T.T. (2008). A study on the thermal conductivity of compacted bentonites. Applied Clay Science, 41 (3), pp. 181-189.
- [25] Tang, A.-M. and Cui, Y.-J. (2010). Effects of mineralogy on thermo-hydro-mechanical parameters of MX80 bentonite. Journal of Rock Mechanics and Geotechnical Engineering, 2 (1), pp. 91-96.
- [26] Wieczorek, K., Miehe, R. and Garitte, B. (2011). Measurement of thermal parameters of the HE-E buffer materials. PEBS Deliverable D2.2-5.
- [27] Gens, A. and Vasconcelos, R. (2019). HE-E Experiment: Modelling of the HE-E test. Mont Terri Project TN 2019-43. Barcelona, Spain.
- [28] Villar, M.V., Martín, P.L., Romero, F.J., Iglesias, R.J. and Gutiérrez-Rodrigo, V. (2016). Saturation of barrier materials under thermal gradient. Geomechanics for Energy and the Environment, 8, pp. 38-51.
- [29] Dixon, D.A., Gray, M.N. and Graham, J. (1996). Swelling and hydraulic properties of bentonites from Japan, Canada and USA. In: Proceedings of the 2nd International Congress on Environmental Geotechnics (ICEG: IS-Osaka'96). Osaka, Japan. November 5-8, 1996, pp. 43-48.
- [30] Karnland, O., Nilsson, U., Weber, H. and Wersin, P. (2008). Sealing ability of Wyoming bentonite pellets foreseen as buffer material – Laboratory results. Physics and Chemistry of the Earth, Parts A/B/C, 33, S472-S475.
- [31] Wang, Q., Tang, A.M., Cui, Y.J., Delage, P. and Gatmiri, B. (2012). Experimental study on the swelling behaviour of bentonite/claystone mixture. Engineering Geology, 124, pp. 59-66.
- [32] Villar, M.V. (2013). Long-term THM tests: isothermal infiltration tests with materials from the HE-E. PEBS Deliverable 2.2-7.2. CIEMAT Technical Report CIEMAT/DMA/2G210/07/2013. Madrid, Spain.
- [33] Villar, M.V., Martín, P.L. and Romero, F.J. (2014). THM cells for the HE-E test: update of results until February 2014. CIEMAT Technical Report CIEMAT/DMA/2G210/03/2014. Madrid, Spain.
- [34] M. V. Villar, A. Gens, K. Černochová, J. Svoboda, D. Mašín, Milestone MS130: HITEC Task 3.3 – Modelling benchmarks – description (Description of calibration case, verification cases and benchmarks selected for T3.3 in cooperation with DONUT), Work Package 7, 4., 2021

2. CTU & CU (SÚRAO)

2.1 Introduction

Modelling of Czech team (CTU, CU, SÚRAO) focuses on representation of THM bentonite behaviour using hypoplastic constitutive model for bentonite implemented within fully and partially coupled unsaturated ground water flow and mechanical finite element code. The final goal is to define soil parameters for bentonite behaviour at temperatures above 100°C and evaluate model predictions with respect to simulation of small- and medium-scale laboratory experiments. In the case the model predictions are not satisfactory, model formulation will be updated to fit the experiment.

At the present state, laboratory experiments on bentonite at high temperatures as well as experiments on thermally treated bentonite are still ongoing. The thermal part of the model, which has already been developed in previous projects, thus cannot be newly calibrated and tested against data above 100°C. For that reason, simulations have been run using thermal parameters calibrated at temperatures below 100°C and they will be updated later once the new parameter set will be known.

In this report, we first present model background and formulation in Sec. 2.2. Later, in Sec. 2.3, simulations of benchmark experiment, as defined in MS130 [17], are presented and discussed.

2.2 Hypoplastic model overview

The model has been developed using a double-structure framework originally proposed by Gens and Alonso [3], who introduced the double structure concept, and Alonso et al. [1], who developed a complete constitutive model. The model is based on the hydro-mechanical double structure hypoplastic model proposed by Mašín [10], which has been enhanced by the effects of temperature. Background and basic hypotheses of this model is briefly described in this section.

2.2.1 Model background

The hypoplastic double-structure model, and double-structure models in general, are based on the assumption supported by various micro-mechanical studies that in expansive soils one can identify two levels of structure: a macrostructure, which represents an assembly of silt-size aggregates of the clay particles, and a microstructure, which represents the internal structure of these aggregates. A conceptual sketch of these two levels of structure is shown in Figure 2.1.

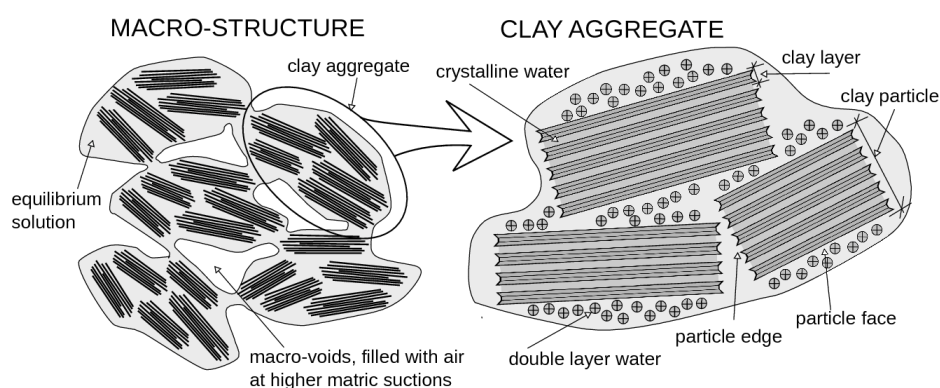


Figure 2.1: Schematic representation of double structure concept (Mašín [10, 12]).

In Mašín [10], separate models are considered for the mechanical and hydraulic responses of the microstructure and of the macrostructure. These responses are coupled at each structural level, and the behavior of the two structural levels is linked through the double-structure coupling function. A schematic of the adopted modeling approach is in Figure 2.2. The individual models are denoted as G^M , G^m , H^M , and H^m , respectively.

EURAD Deliverable 7.10 – HITEC Modelling

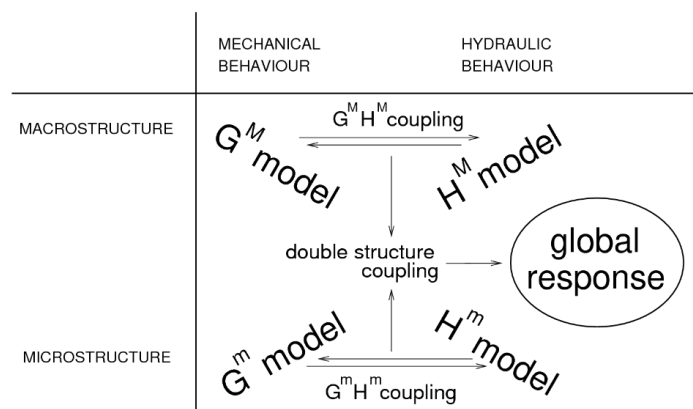


Figure 2.2: Schematic representation of the double structure coupling concept adopted in the hypoplastic model (Mašín, 2013 & 2017).

In the double-structure model from Mašín [10], the mechanical behavior of the macrostructure (G^M) was described using the model for unsaturated soils developed by Mašín and Khalili [13], which itself was based on a hypoplastic model for saturated clays from Mašín [7]. The hydraulic response of the macrostructure (H^M) was based on the void ratio–dependent water retention model from Mašín [8]. The microstructure has always been considered as fully saturated (simple H^m model), with its mechanical behavior (G^m) reversible volumetric, governed by the Terzaghi effective stress principle (see Mašín and Khalili [14] for a thorough discussion). The $G^M H^M$ coupling was accomplished by the dependency of H^M on volume change and by the dependency of the effective stress on degree of saturation of the macrostructure S_r^M . The $G^m H^m$ coupling was introduced through the adoption of the Terzaghi effective stress for the mechanical behavior of the microstructure. Finally, the double-structure coupling was controlled by a function of relative void ratio, which evolved from the original proposition by Alonso et al. (1999).

The model by Mašín [12], adopted in HITEC simulations, evolved from the Mašín [10] by including the thermal component. To accomplish this task, additional thermal dependency has been introduced for water retention curves, volumetric behaviour of microstructure and normal compression behaviour of macrostructure. The final model is a comprehensive model capable of predicting complex THM behaviour of bentonites.

2.2.2 Introduction of hypoplastic framework

Hypoplasticity is an approach to non-linear constitutive modelling of geomaterials. In its general form (Gudehus [4]) it may be written as

$$\dot{\boldsymbol{\sigma}} = f_s(\mathcal{L} : \dot{\boldsymbol{\epsilon}} + f_d \mathbf{N} \|\dot{\boldsymbol{\epsilon}}\|) \quad (1)$$

where $\dot{\boldsymbol{\sigma}}$ and $\dot{\boldsymbol{\epsilon}}$ represent the objective (Zaremba-Jaumann) stress rate and the Euler stretching tensor respectively, \mathcal{L} and \mathbf{N} are fourth- and second-order constitutive tensors, and f_s and f_d are two scalar factors. In hypoplasticity, stiffness predicted by the model is controlled by the tensor \mathcal{L} , while strength (and asymptotic response in general, is governed by a combination of \mathcal{L} and \mathbf{N} . Earlier hypoplastic models (such as the model by von Wolffersdorff [15] and Mašín [7]) did not allow to change the \mathcal{L} formulation arbitrarily, as any modification of the tensor \mathcal{L} undesirably influenced the predicted asymptotic states. This hypoplasticity limitation was overcome by Mašín [9]. He developed an approach enabling to specify the asymptotic state boundary surface independently of the tensor \mathcal{L} and demonstrated it by proposing a simple hypoplastic equivalent of the Modified Cam-clay model. Based on this approach, Mašín [11] developed an advanced hypoplastic model for clays, which is adopted in the THM model used in this work.

The basic hypoplastic model requires five material parameters φ_c , N , λ^* , κ^* and v . The parameters have the same physical interpretation as parameters of the Modified Cam clay model, and they are thus easy to calibrate based on standard laboratory experiments. The model parameters N and λ^* define the

EURAD Deliverable 7.10 – HITEC Modelling

position and the slope of the isotropic normal compression line in the $\ln(1 + e)$ vs. $\ln(p/p_r)$ plane. The isotropic normal compression line is described using equation

$$\ln(1 + e) = N - \lambda^* \ln\left(\frac{p}{p_r}\right) \quad (2)$$

where $p_r = 1$ kPa is a reference stress. Parameter κ^* controls the slope of the isotropic unloading line in the same plane and also of the isotropic compression line of over-consolidated soil. φ_c is the critical state friction angle, with identical meaning with any other critical state soil mechanics – based model. Finally, the parameter ν controls shear modulus.

Apart from stress, the most important state variable controlling the response of the model is void ratio e , or, equivalently, overconsolidation ratio OCR . The OCR is in hypoplasticity defined as:

$$OCR = \frac{p_e}{p} \quad (3)$$

where p_e is the Hvorslev equivalent pressure; that is, mean effective stress at the isotropic normal compression line calculated using Eq. (2) at the current void ratio.

The principle of hypoplasticity can best be demonstrated using a simple one-dimensional model. 1D version of hypoplastic model for shear reads:

$$d\tau = Ld\gamma + N|d\gamma| \quad (4)$$

where $d\tau$ is increment of shear stress (note that compression negative sign convention is adopted), $|X|$ represents absolute value of X and L and N are two moduli. In hypoplasticity, neither the switch function distinguishing between loading and unloading, as in elasto-plastic model, nor strain decomposition into elastic and plastic parts, are needed. A scalar "modulus" N may be defined as

$$N = LY \quad (5)$$

with

$$Y = \frac{\tau}{\tau_{yield}} \quad (6)$$

The modulus L may be specified using a parameter such that $L = E_n$. This simple 1D hypoplastic model thus requires two parameters τ_{yield} and E_n . Predictions of this 1D model are shown in Figure 2.3, where they are compared with predictions of model elastoplastic.

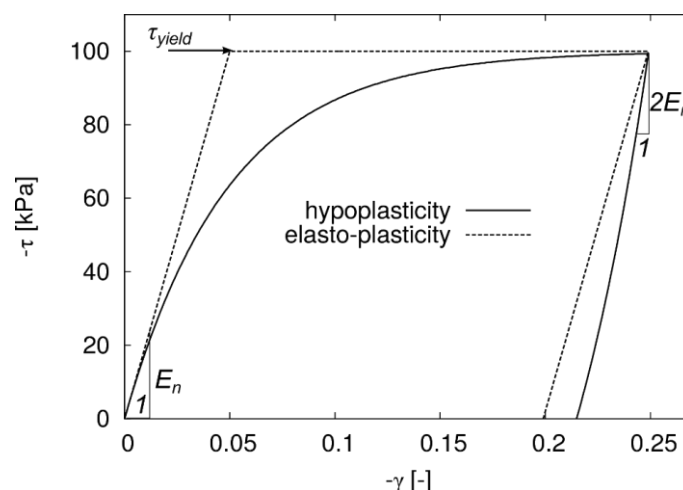


Figure 2.3: Demonstration of hypoplasticity principles using a simple one-dimensional model.

Let us now consider the Equation (4) and evaluate the stiffness predicted by the hypoplastic model. First of all, the stiffness depends on loading direction (as in elasto-plasticity), thanks to the absolute value appearing in Eq. (4). The following two cases are important for clarifying the model performance:

1. When $\tau = 0$, Y calculated using Eq. (4) is equal to zero. Therefore, $N = 0$ and thus

EURAD Deliverable 7.10 – HITEC Modelling

$$d\tau = Ld\gamma \quad (7)$$

L thus specifies the initial modulus for loading from the state $\tau = 0$.

2. When $\tau = \tau_{yield}$, Y is equal to one. Therefore, $N = L$ and the hypoplastic equation reads

$$d\tau = L(dy + |d\gamma|) \quad (8)$$

In loading, $d\gamma < 0$ and therefore $d\tau = 0$, similar as in elasto-plasticity. During unloading, $d\gamma > 0$ and hypoplasticity predicts

$$d\tau = 2Ld\gamma \quad (9)$$

It follows from the above that for the special cases of $\tau = 0$ and $\tau = \tau_{yield}$ the hypoplastic model predicts similar response as the elasto-plastic model (apart from the unloading modulus at $\tau = \tau_{yield}$, which is twice as high as the loading modulus at $\tau = 0$). The most important difference in predictions of the two models is in the intermediate states $\tau_{yield} < \tau < 0$. While elasto-plasticity predicts constant stiffness E_n , hypoplasticity predicts gradual decrease of stiffness, starting from the initial modulus E_n and ending with the fully plastic state with stiffness equal to zero. The stiffness decrease is caused by the definition of Y , whose value gradually increases from 0 to 1 and thus forces the modulus N to vary between zero and L .

2.2.3 Mathematical formulation of the THM model

The primary equation of the THM hypoplastic model reads

$$\dot{\sigma}^M = f_s[\mathcal{L} : (\dot{\epsilon} - f_m \dot{\epsilon}^m) + f_d \mathbf{N} \|\dot{\epsilon} - f_m \dot{\epsilon}^m\|] + f_u(\mathbf{H}_s + \mathbf{H}_T) \quad (10)$$

For description of the complete mathematical formulation of the model, interested reader is referred to Mašín (2017). Complete model formulation is also given in Appendix of this report. In the following, the main components of Eq. (10) are described:

- Behaviour of *macrostructure* is defined using the hypoplastic approach. Thus, Eq. (10) defines the effective stress rate of macrostructure $\dot{\sigma}^M$. It is defined using Bishop equation, in which the factor χ is equal to the degree of saturation of macrostructure.

$$\sigma^M = \sigma^{net} - \mathbf{1} S_r^M s \quad (11)$$

where σ^{net} is net stress, s is suction and S_r^M is degree of saturation of macrostructure defined using a hysteretic macrostructural void ratio-dependent water retention model of Brooks and Corey [2] type. The water retention model for macrostructure is sketched in Figure 2.4.

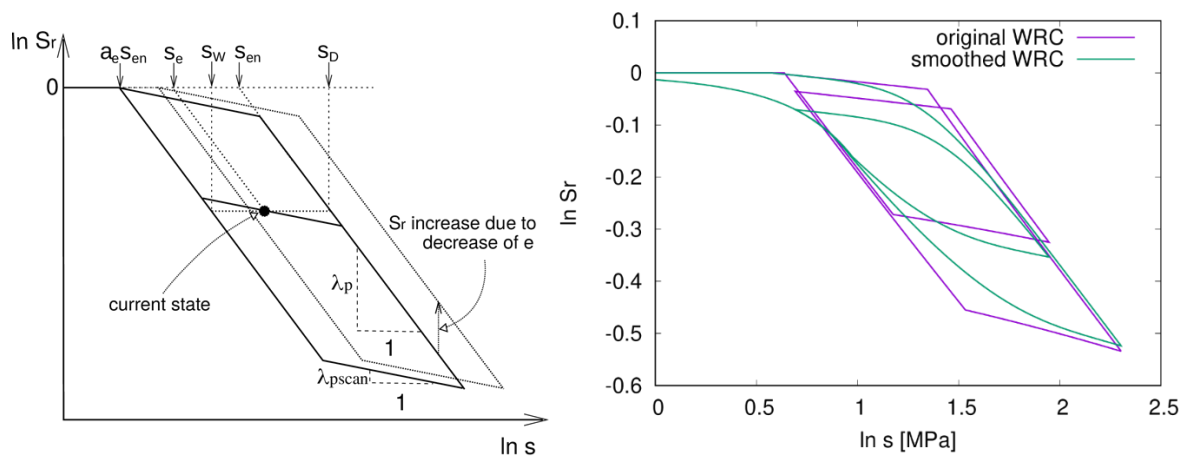


Figure 2.4: Hysteretic water retention model for macrostructure adopted in hypoplastic THM model for expansive soils – definition of variables (left) and smooth formulation adopted in recent version of the model (right)

- Behaviour of *microstructure* is defined using elastic volumetric model, which can be written as

EURAD Deliverable 7.10 – HITEC Modelling

$$\dot{\epsilon}^m = \frac{1}{3} \left(\alpha_s \dot{T} - \frac{\kappa_m}{p^m} \dot{p}^m \right) \quad (12)$$

where $\dot{\epsilon}^m$ is microstructural strain, \dot{T} is temperature rate, p^m is microstructural mean effective stress and α_s and κ_m are parameters. Microstructure is always assumed to be fully saturated and its behaviour governed by the Terzaghi effective stress, that is

$$\sigma^m = \sigma^{net} - 1s \quad (13)$$

- The double structure coupling is accomplished through the factor f_m appearing in Eq. (10). This factor depends on relative density, such that for the most dense state $f_m = 1$ and for the most loose state $f_m = 0$. These values mean that at the loose state microstructural strain does not cause any macrostructural deformation, because microstructural units (aggregates) swell into the macrovoids. Contrary, at the densest possible state macrostructure is basically closed, and any microstructural strain causes equivalent strain macrostructural. The factor f_m is defined as

$$f_m = 1 - (r_{em})^m \quad (14)$$

where m is a parameter and r_{em} is relative void ratio defined as

$$r_{em} = \frac{e - e_d}{e_i - e_d} \quad (15)$$

where e_d is minimum void ratio (equal to microstructural void ratio) and e_i is maximum void ratio (equal to the void ratio at the isotropic normal compression line).

- Eq. (10) contains two tensors \mathbf{H}_s and \mathbf{H}_T and a scalar factor f_u . The factors \mathbf{H}_s and \mathbf{H}_T are denoted as wetting- and heating-induced collapse factors, calculated to ensure that during wetting and heating of specimen whose state is close to the isotropic normal compression line (NCL), its state remains at NCL and thus wetting- and heating-induced collapse is predicted. The factor f_u depends on relative density and decreases the effect of \mathbf{H}_s and \mathbf{H}_T for higher overconsolidation ratios.
- Last, Eq. (10) contains two scalar factors f_s and f_d . These are denoted as barotropy- and pyknotomy factors and they control the effect of stress and void ratio on macrostructural soil stiffness. They were taken over from the basic hypoplastic model for clays from Mašín (2014).

The complete mathematical formulation of the THM hypoplastic model is in Appendix.

2.2.4 Input parameters

Model parameters and their description is summarised in Table 2.1.

Table 2.1: Model parameters and their description (from Mašín [12]).

Parameter	Description
φ_c	Critical state friction angle of macrostructure in a standard soil-mechanics context
λ^*	Slope of isotropic normal compression line in $\ln(p^M/p_r)$ versus $\ln(1 + e)$ space
κ^*	Macrostructural volume strain in p^M unloading
N	Position of isotropic normal compression line in $\ln(p^M/p_r)$ versus $\ln(1 + e)$ space
ν	Stiffness in shear
n_s	Dependency of position of isotropic normal compression line on suction
l_s	Dependency of slope of isotropic normal compression line on suction
n_T	Dependency of position of isotropic normal compression line on temperature
l_T	Dependency of slope of isotropic normal compression line on temperature
m	(1) Control of f_u and thus dependency of wetting-/heating-induced compaction on distance from state boundary surface; (2) control of double-structure coupling function and thus response to wetting-drying and heating-cooling cycles (Mašín 2013b)
α_s	Dependency of microstructural volume strains on temperature
κ_m	Dependency of microstructural volume strains on p^m
e_{r0}^m	Reference microstructural void ratio for reference temperature T_r , reference suction s_r , and zero total stress
c_{sh}	Value of f_m for compression
s_{e0}	Air-entry value of suction for reference macrostructural void ratio e_0^M
a	Dependency of macrostructural air-entry value of suction on temperature
b	Dependency of macrostructural air-entry value of suction on temperature
a_e	Ratio of air entry and air expulsion values of suction for macrostructure water retention model
s_r	Reference suction for e^m
e_0^M	Reference macrostructural void ratio for air-entry value of suction of macrostructure
T_r	Reference temperature

2.3 Numerical model of the small-scale experiment

The aim of the small-scale experiment (chamber of \varnothing 30 cm, height 30 cm) was the investigating the influence of long-term thermal loading (dry and wet materials loaded at 150°C for 6, 12, and 24 months) on bentonite material. Attention was paid to analyses of water content and dry density changes and obtaining data for mathematical modelling - measuring the geotechnical parameters – hydraulic conductivity, swelling pressure, liquid limit, etc. The experiment was performed in the Josef Underground Research Facility (URF) laboratory of the Faculty of Civil Engineering Czech Technical University in Prague, Czech Republic. Two runs of the experiment were performed. For the first, the BCV (bentonite from Černý Vrch repository) of the initial dry density 900 kg/m³ was used. The material was saturated with 6 bars of water pressure and heated up to 150°C. Phases of watering and heating were performed simultaneously to avoid water boiling. In the second run, the experiment was heated up to 150°C the first and then watered. For this setup, the water boiling is expected in the middle of the chamber. The BCV initial dry density was 1400 kg/m³. This second run simulates the conditions in the nuclear waste repository more precisely.

The thermo-hydro-mechanical (THM) model of the small-scale experiment is simulated using partially coupled analysis consisting of two individual finite element modules – a transport part solving heat and moisture analysis and a mechanical part describing the mechanical response. Both parts are running simultaneously, and the necessary data are transferred between modules in each time step. The coupled analysis is based on the extended micromechanical approach for coupled heat and moisture transfer in porous media presented by Lewis and Schrefler in [6] and the hypoplastic model for expansive clays presented by Mašín in [12] implemented into the SIFEL bundle [5].

The numerical model discretizes the bentonite sample and the whole steel structure as an axisymmetric domain. The finite element mesh consists of 17,282 nodes and 5,756 elements with linear approximation functions in the transport part and quadratic approximation functions in mechanical part. The possibility of the detachment of the bentonite material along the inner surface of the steel structure is secured by doubled nodes at the bentonite-steel interface. The coupling of individual degrees of freedom for surface perpendicular displacements and temperature is ensured.

The model is loaded by water pressure at the top bentonite surface and heating in the area corresponding to the heater installed. Boundary Newton's condition is prescribed on the external surfaces modelling the heat transfer between steel structure and the air (*Figure 2.34*). The heat transfer coefficient $\beta = 20 \text{ W}\cdot\text{K}^{-1}\cdot\text{m}^{-2}$. The prescribed temperature of the ambient air is taken from measurements – sensor No. 711.10, the temperature of the heating system is taken from sensor No. 113.10. The watering is prescribed according to data measurement – sensor No. 799.90. For computational stability, the data were approximated by a piecewise linear function, see *Figure 2.35*.

EURAD Deliverable 7.10 – HITEC Modelling

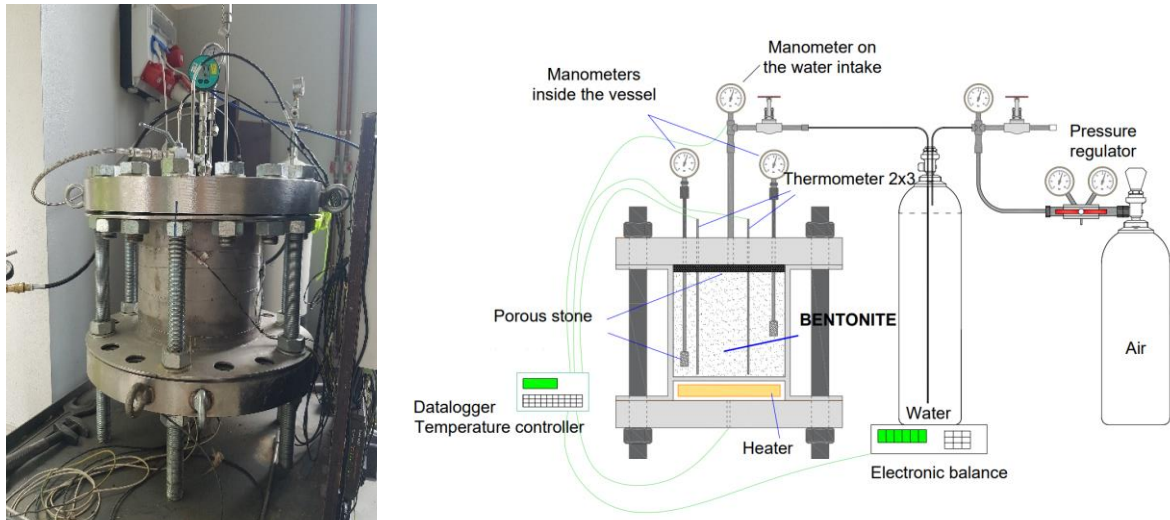


Figure 2.33: Installation and the setup of the experiment

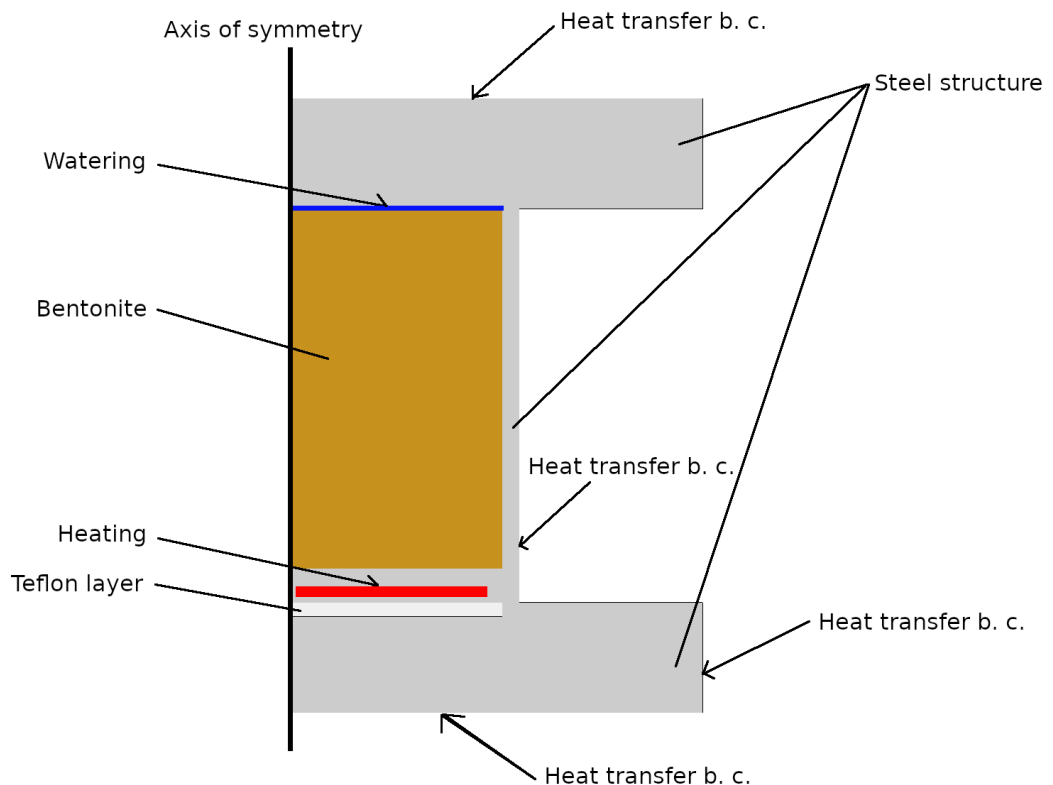


Figure 2.34: Set up of the numerical model

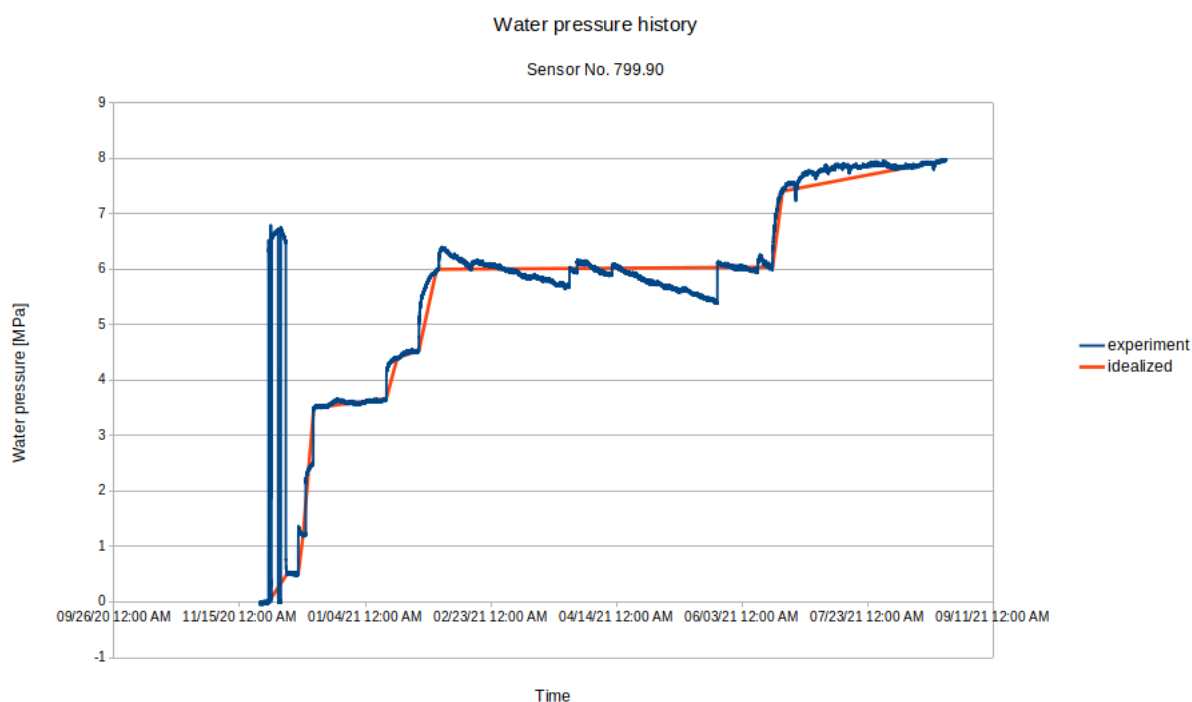


Figure 2.35: Prescribed water pressure

Due to convergence problems of the hypoplastic bentonite model for low dry densities, the initial material parameters were set for the dry density $\rho_d = 1500 \text{ kg}\cdot\text{m}^{-3}$. All material parameters are listed in *Table 2.2*, *Table 2.3* and *Table 2.4*. It should be noted steel structure and the Teflon layer have been modelled as ideal linear elastic materials enabling only heat transfer and no water and moisture transfer.

Table 2.2: Material parameters of THM model – transport part

Material parameters for bentonite	Value
Initial porosity	0.4774
Intrinsic permeability	$2\cdot 10^{-19} \text{ m}^2$
Volume density	$1500 \text{ kg}\cdot\text{m}^{-3}$
Effective specific heat	$1000 \text{ J}\cdot\text{kg}^{-1}\cdot\text{K}^{-1}$
Dry effective thermal conductivity	$0.6 \text{ W}\cdot\text{m}^{-1}\cdot\text{K}^{-1}$
Wet effective thermal conductivity	$1.35 \text{ W}\cdot\text{m}^{-1}\cdot\text{K}^{-1}$
Cubic thermal dilatation coefficient	$1\cdot 10^{-7} \text{ K}^{-1}$
Material parameters for steel	Value
Volume density	$7850 \text{ kg}\cdot\text{m}^{-3}$

EURAD Deliverable 7.10 – HITEC Modelling

Specific heat	450 J·kg ⁻¹ ·K ⁻¹
Thermal conductivity	47 W·m ⁻¹ ·K ⁻¹
Thermal dilatation coefficient	12·10 ⁻⁶ K ⁻¹
Material parameters for Teflon	Value
Volume density	2150 kg·m ⁻³
Specific heat	1000 J·kg ⁻¹ ·K ⁻¹
Thermal conductivity	0.25 W·m ⁻¹ ·K ⁻¹
Thermal dilatation coefficient	12·10 ⁻⁶ K ⁻¹

Table 2.3: Material parameters of THM model – mechanical part

State variables for bentonite	Value
Dry density	1500 kg·m ⁻³
Initial void ratio	0.9133
Material parameters for steel	Value
Young's modulus	210 GPa
Poisson's ratio	0.3
Material parameters for Teflon	Value
Young's modulus	340 MPa
Poisson's ratio	0.3

Table 2.4: THM hypoplastic constitutive model parameters for bentonite

Parameter	Unit	Value
φ_c	°	25
λ	–	0.12

EURAD Deliverable 7.10 – HITEC Modelling

κ	–	0.02
N	–	1.62
ν	–	0.24
n_s	–	0.01
l_s	–	0.0
n_T	–	-0.07
l_T	–	0
m	–	10
α_s	$1/K$	0.00015
κ_m	–	0.1
s_r	kPa	-1000
e_{r0}^m	–	1.0
c_{sh}	–	0.1
s_{e0}	kPa	-2,700
e_0^M	–	0.50
T_r	K	294
a	N/m	0.118
b	$N/(mK)$	-0.000154
a_e	–	0.75
λ_{p0}	–	1.2

2.4 Simulation results of the first run

The analysis simulated the watering and heating processes from the beginning of the experiment to the present time (the experiment is currently still ongoing). The start time $t_{start} = 0$ sec was set to 11/22/2020 23:00:00, and the end time $t_{end} = 23,626,800$ sec was set to 08/03/2021 22:20:00. The whole analysis took 30 hours on PC computer Intel® Core™ i7-10700F CPU @ 2.90GHz x 16 equipped

EURAD Deliverable 7.10 – HITEC Modelling

with RAM 32 GB using multithreading OpenMP system on the Linux Ubuntu 21.04 platform. Selected results of the history of temperatures are presented in *Figure 2.36* to *Figure 2.42*. The final temperature profile is in *Figure 2.43*. *Figure 2.44* shows the evolution of vertical pressure at the top and bottom of the bentonite sample, which was unfortunately not measured. Selected profiles of saturation degree are depicted in *Figure 2.45* to *Figure 2.47*. *Figure 2.48* recalls the scheme of all sensors placement in the experiment.

Analysis of results shows agreement in calculated and measured temperatures for almost all sensors except sensor No. 611.10, which is placed at the bottom part of the external surface of the steel cylinder. The bentonite sample is fully saturated in approximately 60 days from the beginning of the water filling. The evolution of the vertical pressure corresponding to swelling pressure follows the gradual saturation of the bentonite and subsequent increase of water pressure. The values corresponding to dry density $\rho_d = 1500 \text{ kg}\cdot\text{m}^{-3}$ are at higher levels than values expected from the measurements.

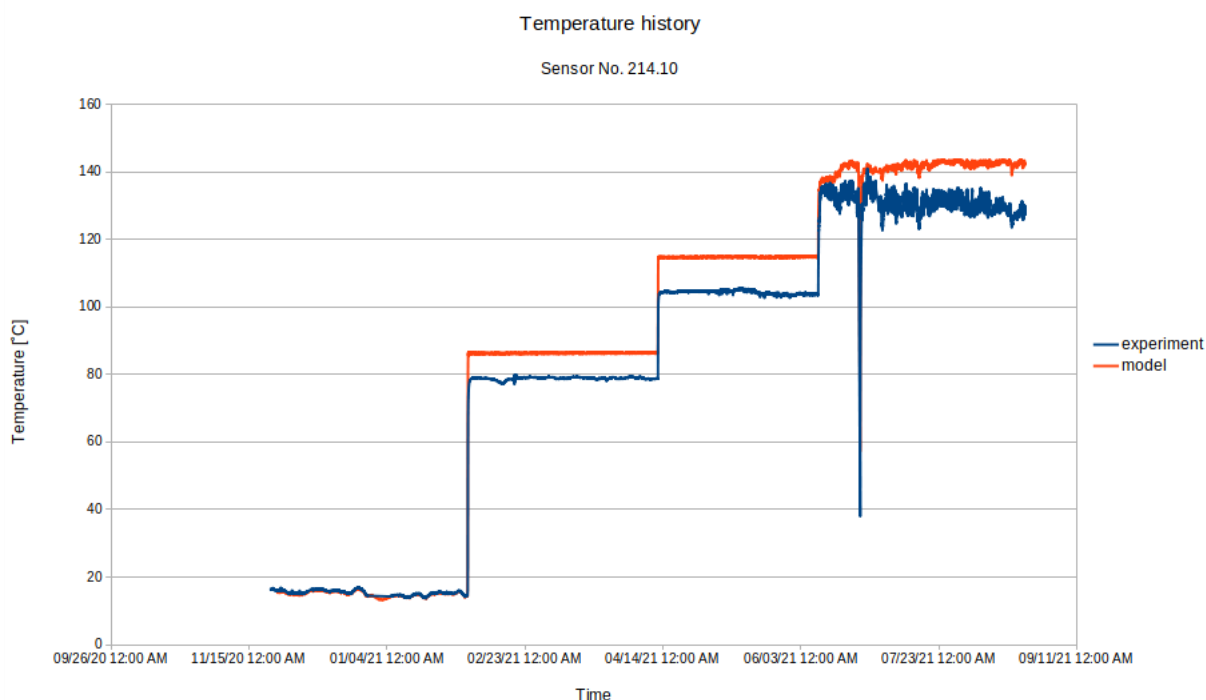


Figure 2.36: Temperature history in sensor 214.10

EURAD Deliverable 7.10 – HITEC Modelling

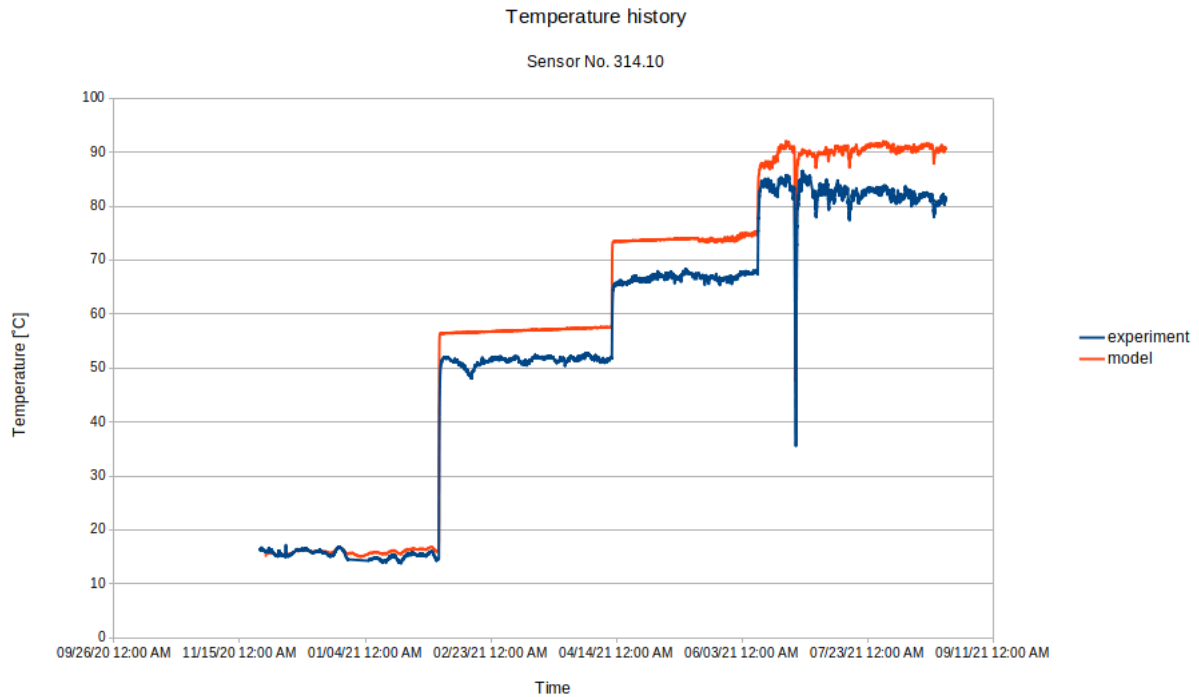


Figure 2.37: Temperature history in sensor 314.10

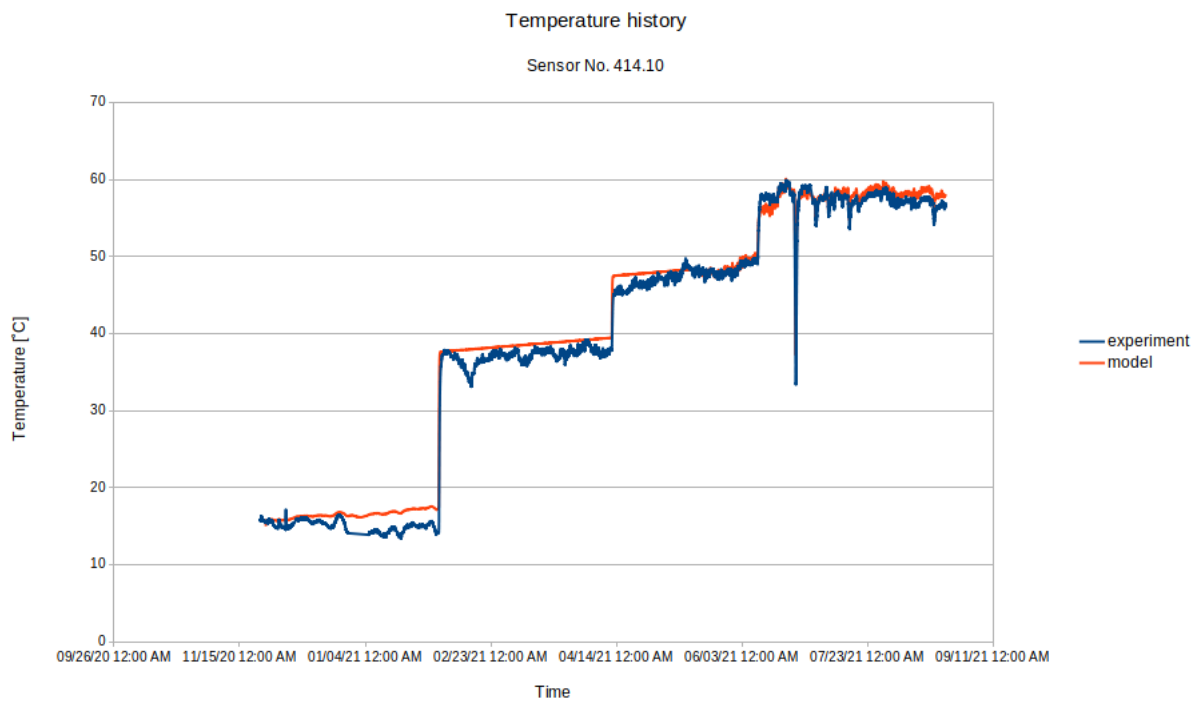


Figure 2.38: Temperature history in sensor 414.10

EURAD Deliverable 7.10 – HITEC Modelling

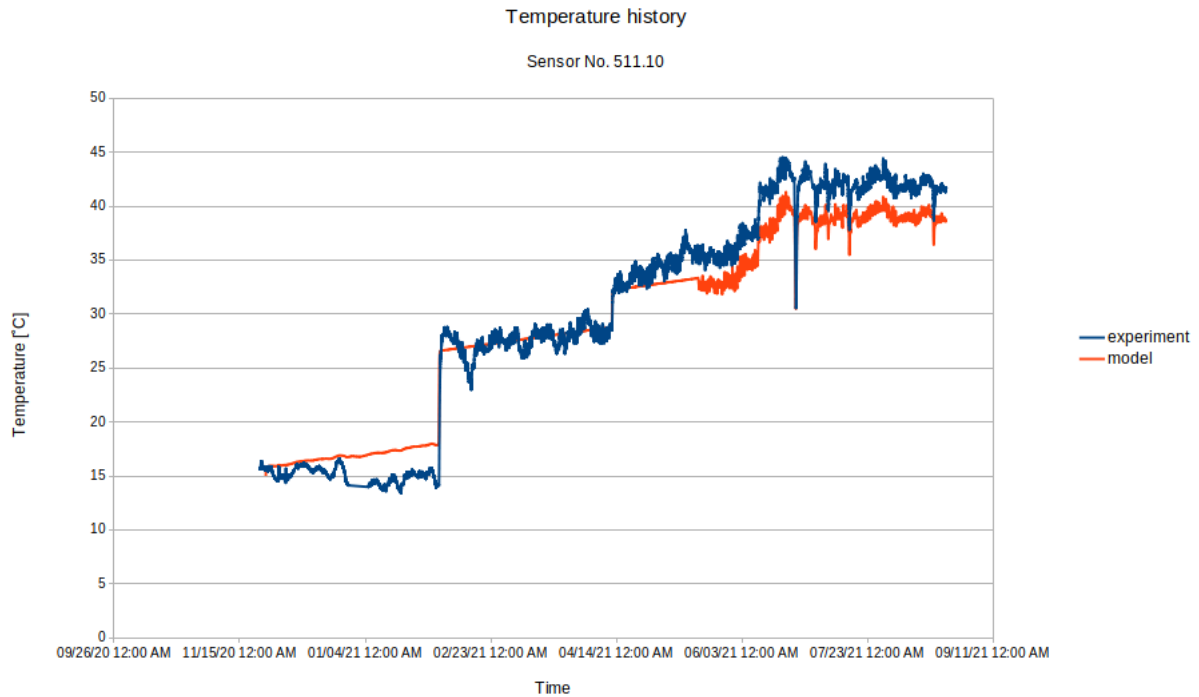


Figure 2.39: Temperature history in sensor 511.10

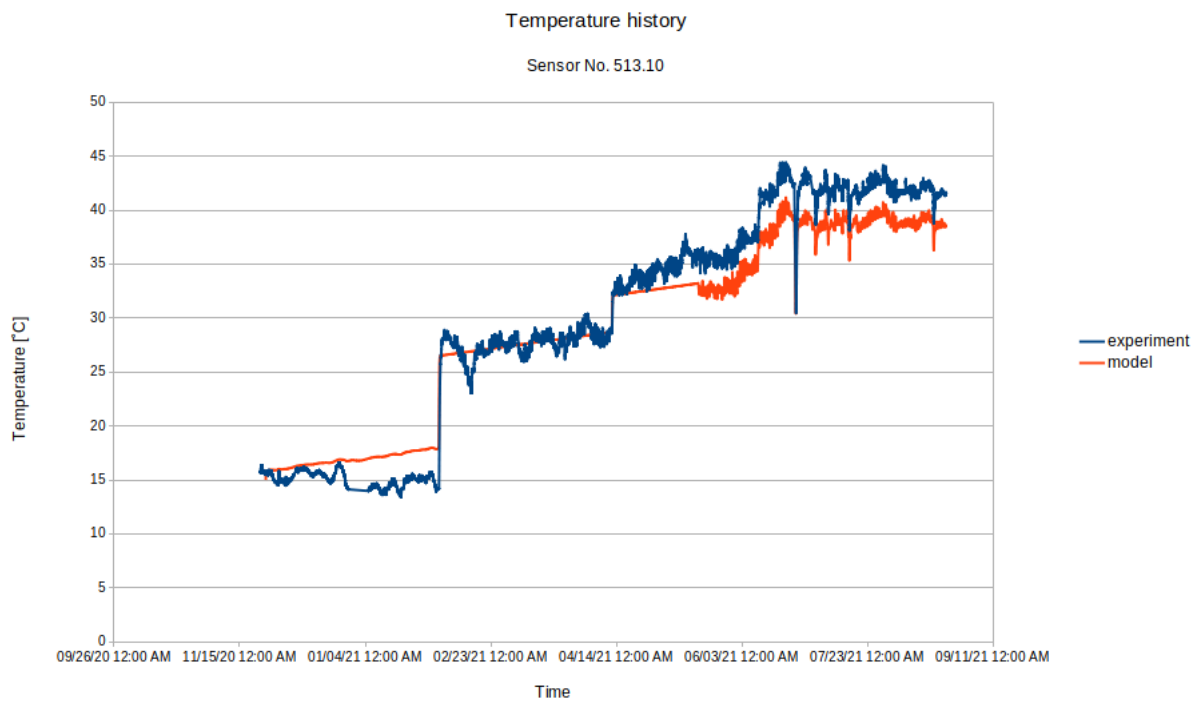


Figure 2.40: Temperature history in sensor 513.10

EURAD Deliverable 7.10 – HITEC Modelling

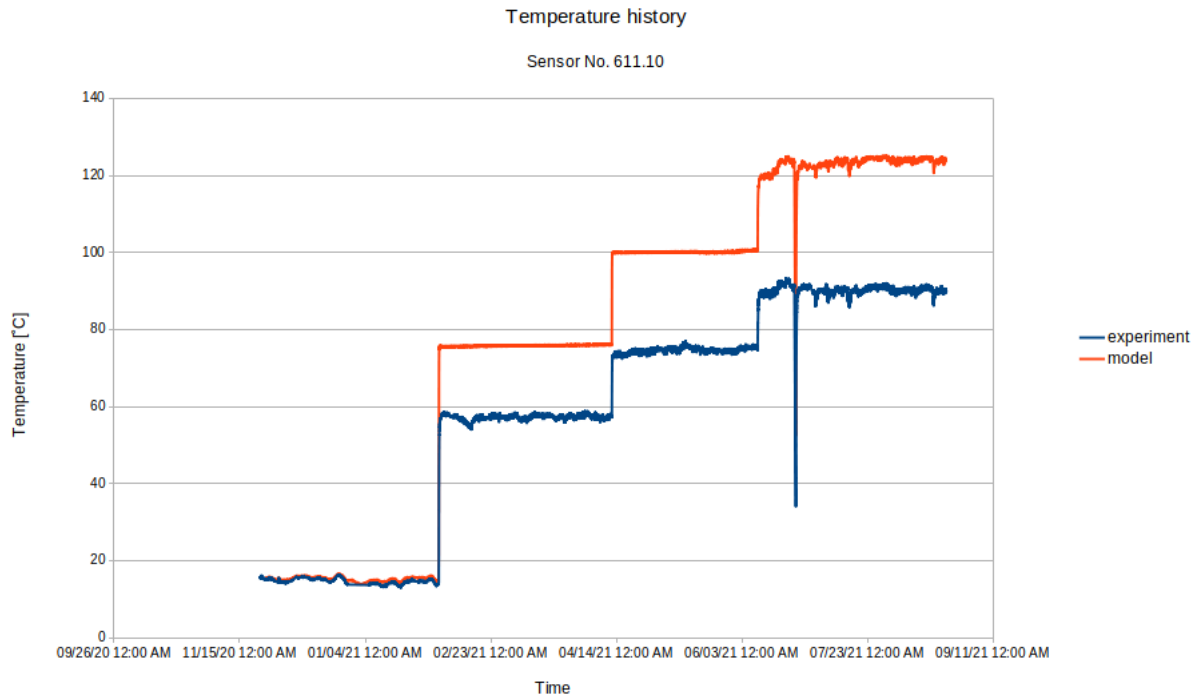


Figure 2.41: Temperature history in sensor 611.10

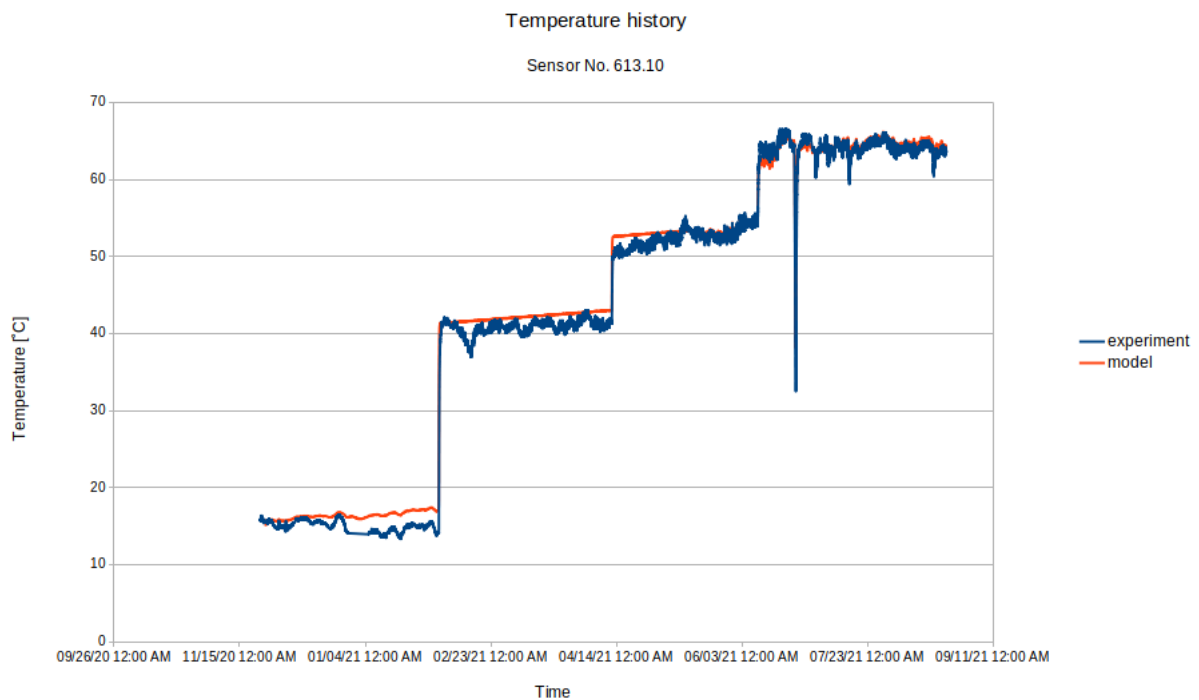


Figure 2.42: Temperature history in sensor 613.10

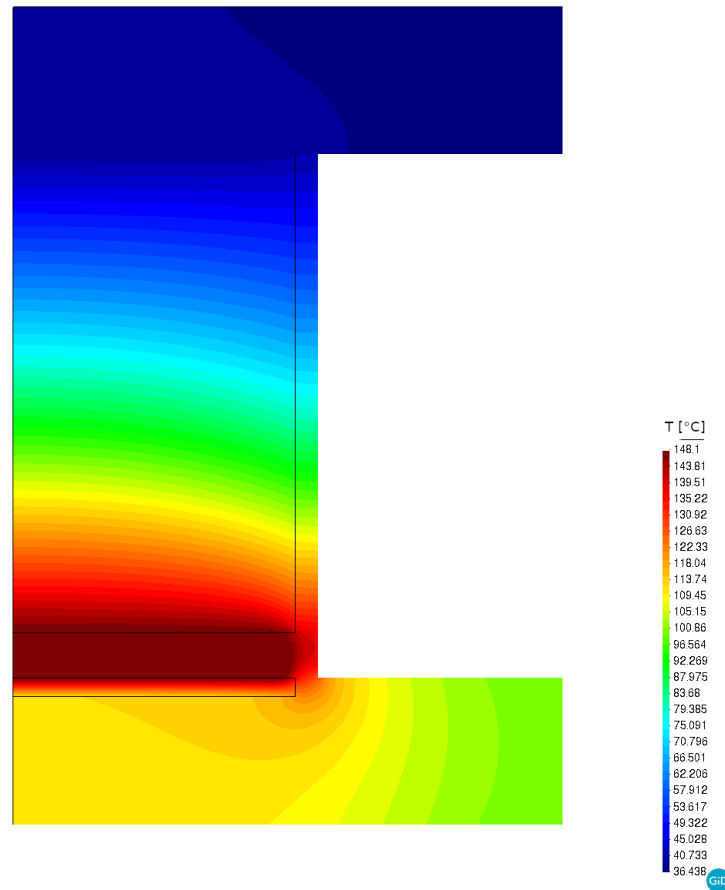


Figure 2.43: Temperature profile at the end time

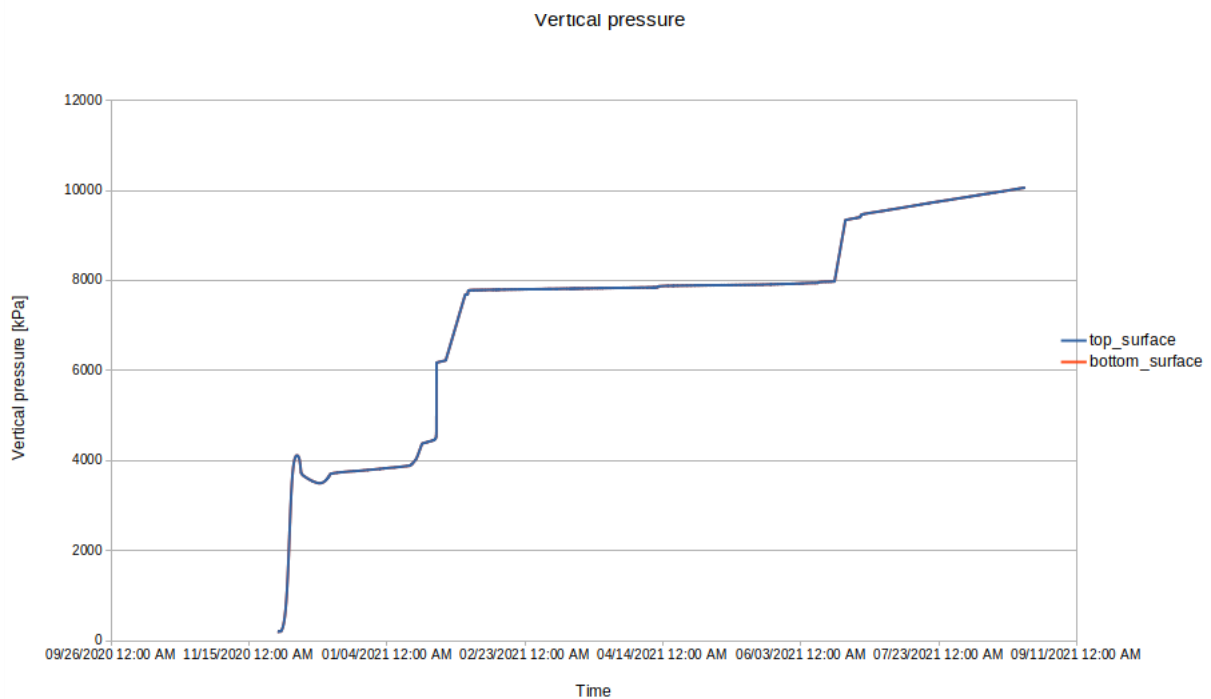


Figure 2.44: Vertical pressure evolution

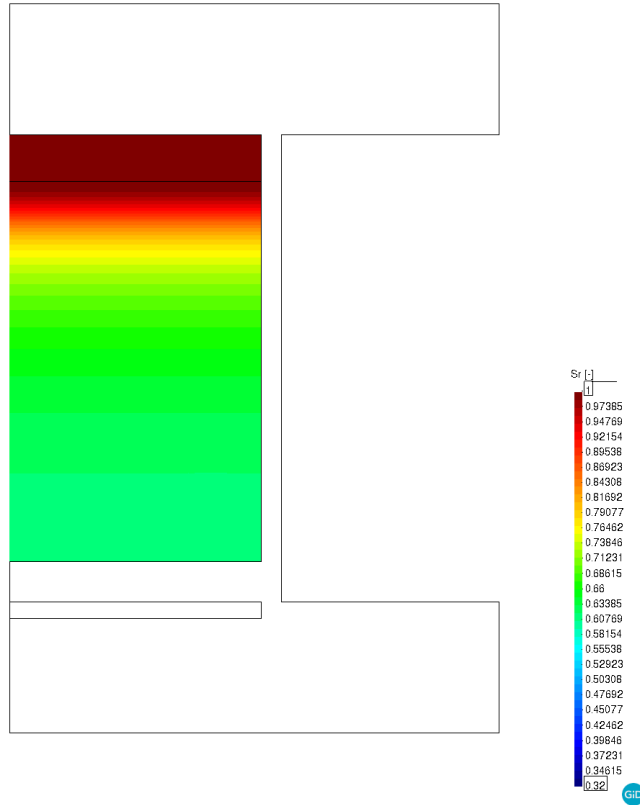


Figure 2.45: Saturation degree profile at time 20 days

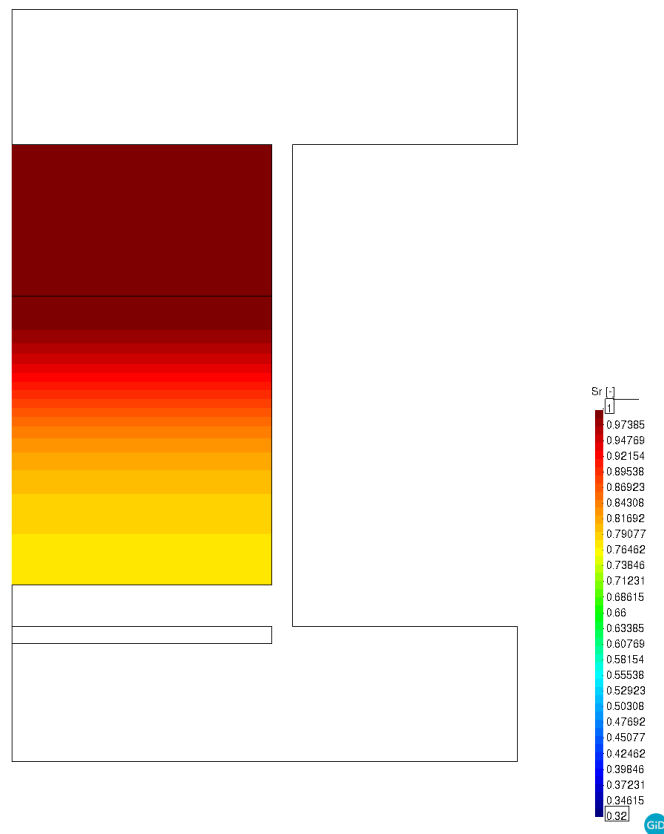


Figure 2.46: Saturation degree profile at time 40 days

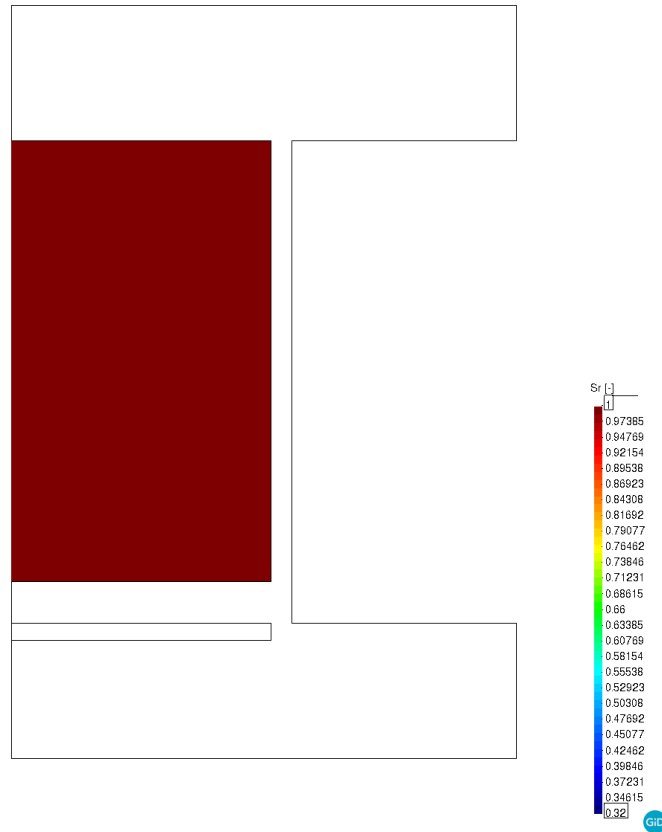


Figure 2.47: Saturation degree profile at time 60 days

1.1

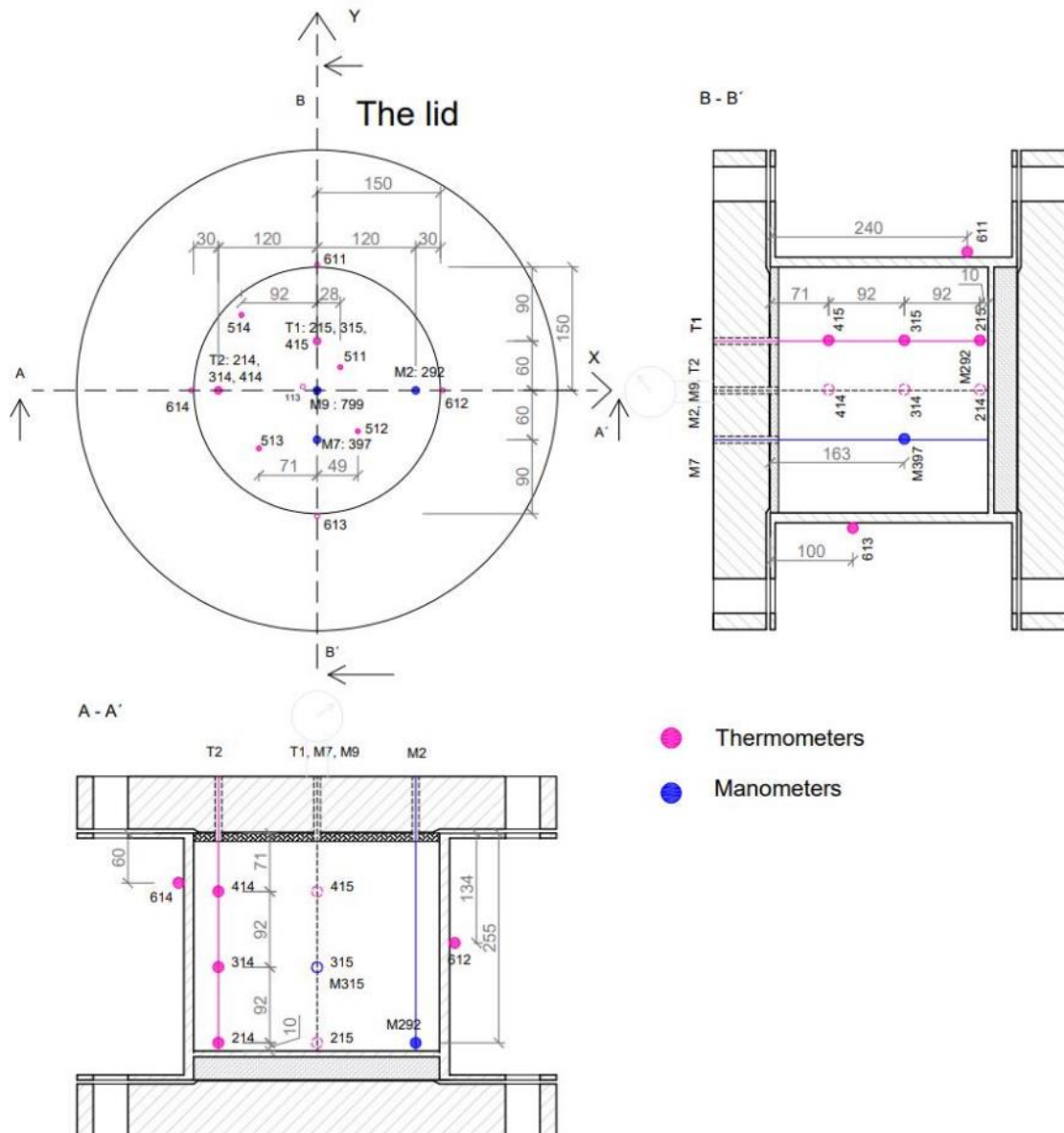


Figure 2.48: Scheme of the instrumentation [17]

2.5 Simulation results of the second run

Analysis of results of the second simulation shows agreement in calculated and measured temperatures for almost all sensors. The evolution of the vertical pressure corresponding to swelling pressure also follows the gradual saturation of the bentonite and subsequent increase of water pressure. Unfortunately, the model has convergence issues in the phase with increasing water pressure. This will be the aim of further investigation and model validation.

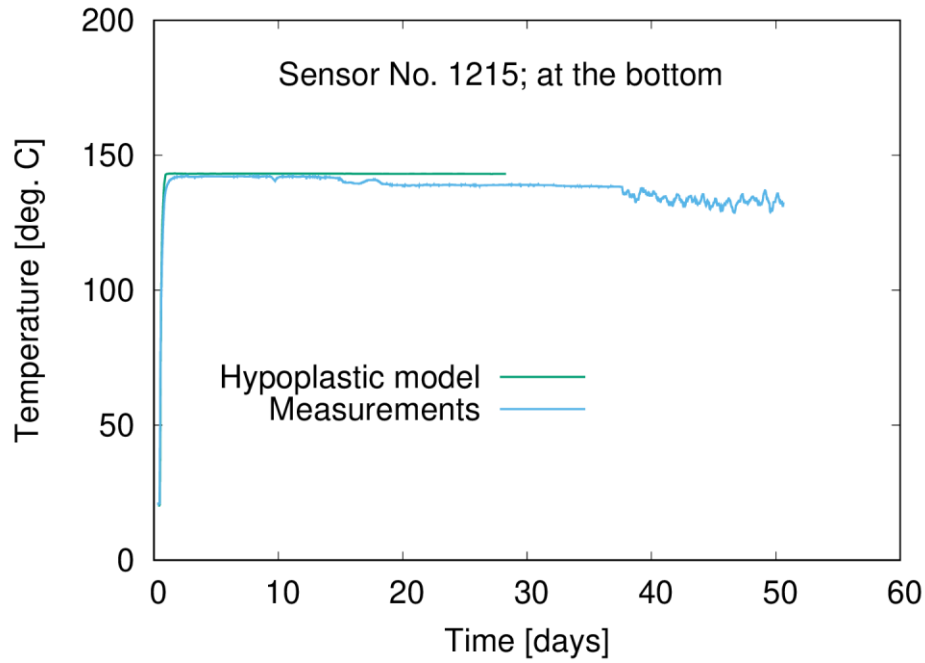


Figure 2.49: Temperature history in sensor 1215

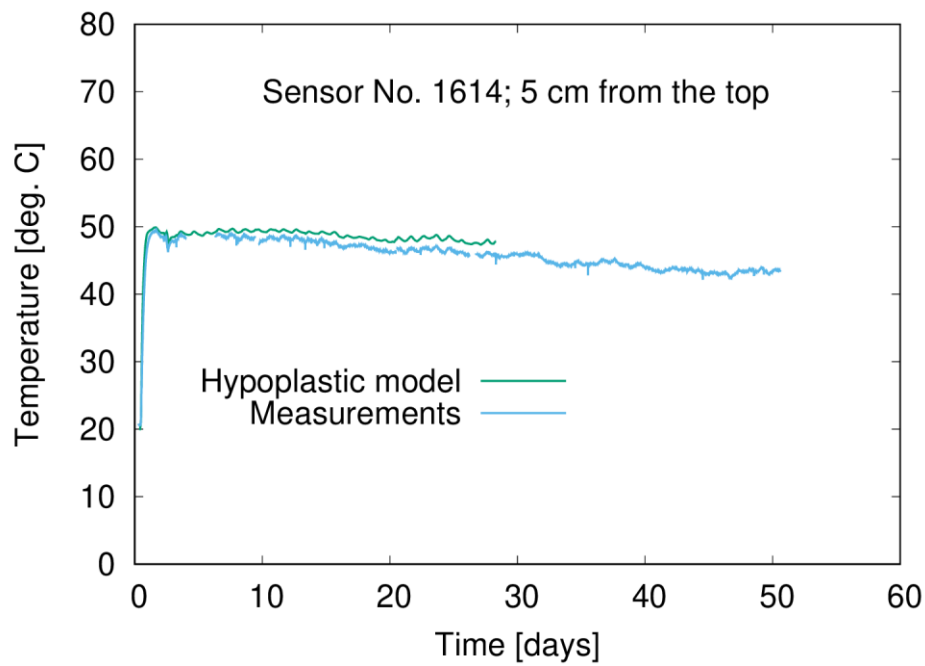


Figure 2.50: Temperature history in sensor 1614

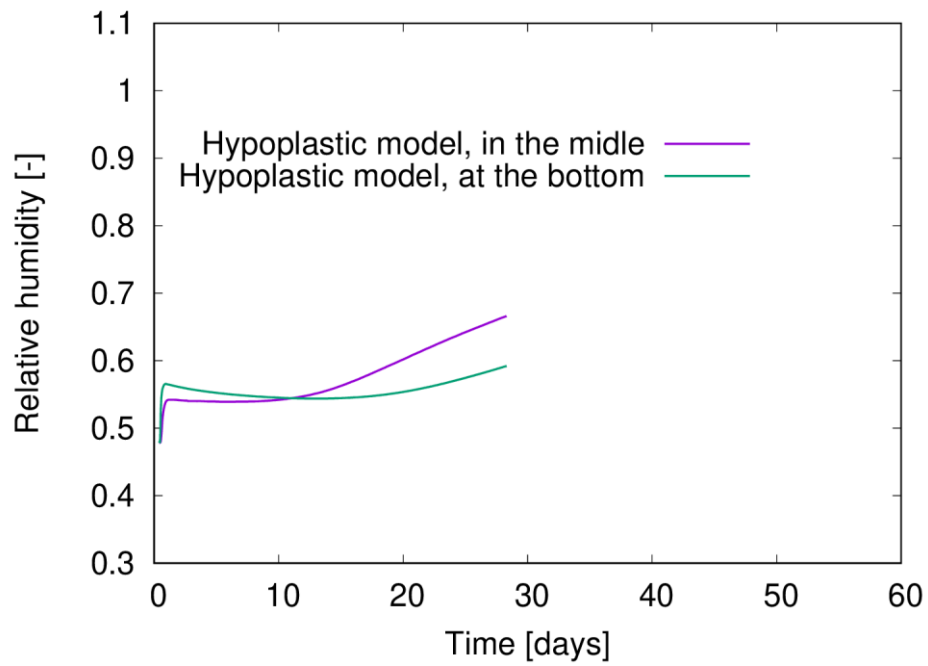


Figure 2.51: Relative humidity evolution

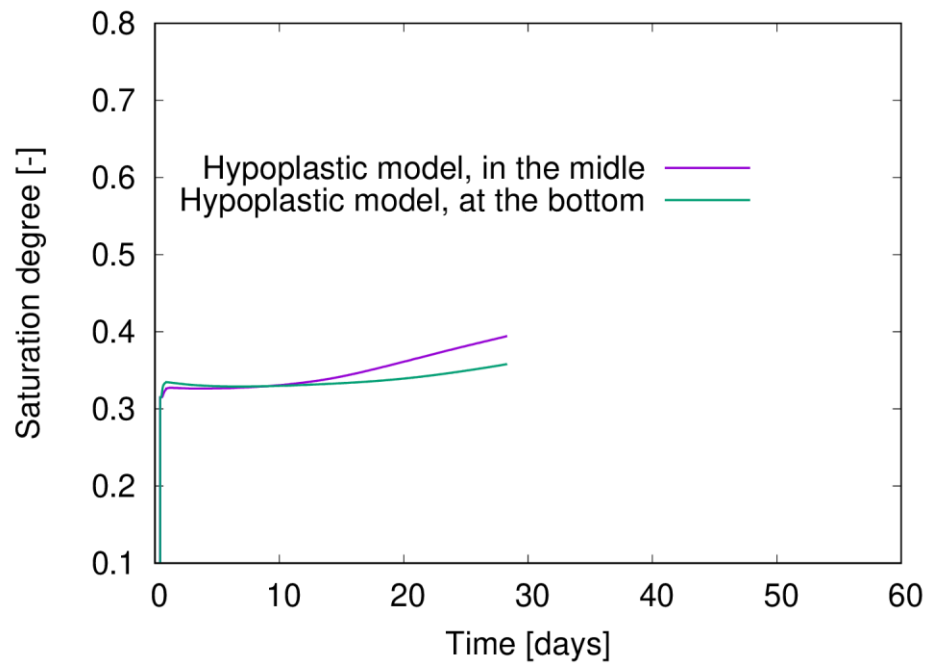


Figure 2.52: Saturation degree evolution

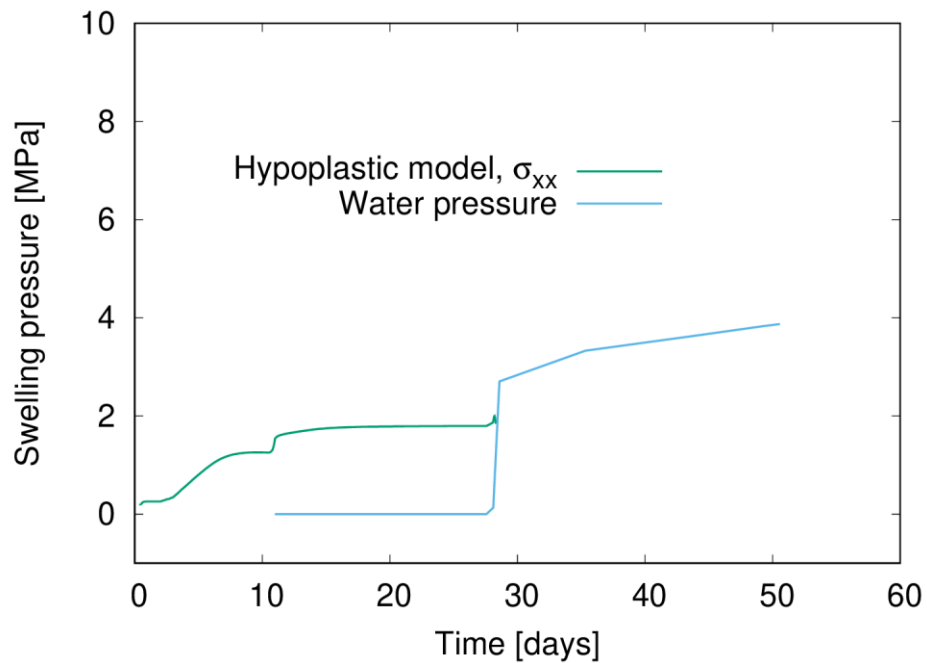


Figure 2.53: Swelling pressure in radial direction at the bottom

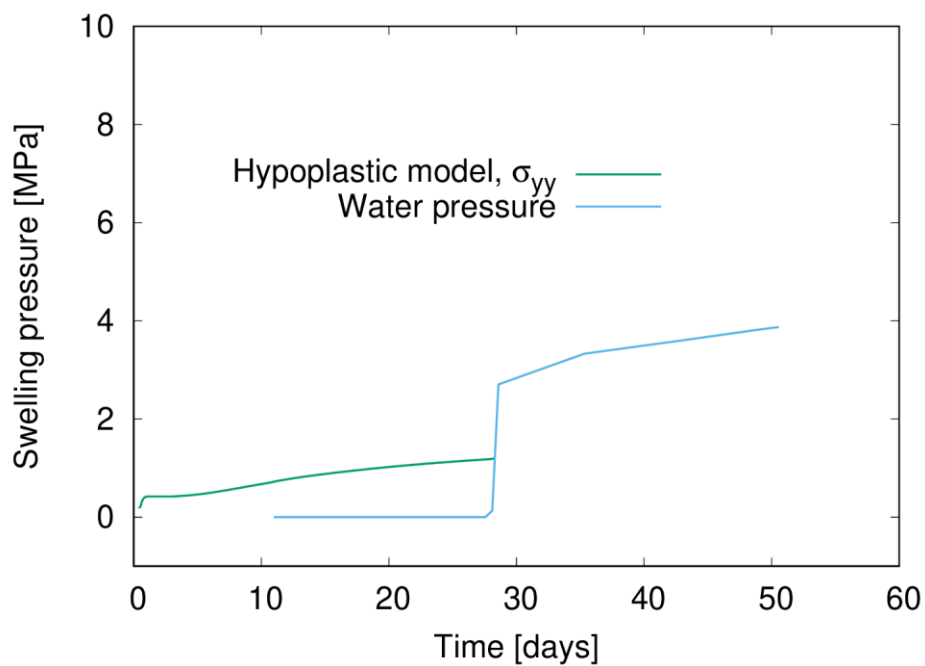


Figure 2.54: Swelling pressure in horizontal direction at the bottom

2.6 References

- [1] Alonso, E.E., Vaunat, J., Gens, A. Modelling the mechanical behaviour of expansive clays. *Engineering Geology* 54, 173–183, 1999
- [2] Brooks, R., Corey, A.. Hydraulic properties of porous media. Hydrology paper no. 3. Colorado State University, 1964
- [3] Gens, A., Alonso, E. A framework for the behaviour of unsaturated expansive clays. *Canadian Geotechnical Journal* 29, 1013–1032, 1992
- [4] Gudehus, G. A comprehensive constitutive equation for granular materials. *Soils and Foundations* 36 (1), 1–12, 1996
- [5] J. Kruis, T. Koudelka, and T. Krejčí, SIFEL package, <http://ksm.fsv.cvut.cz/~sifel/>, 2001 – 2021.
- [6] R. Lewis, B. Schrefler, *The Finite Element Method in the Static and Dynamic Deformation and Consolidation of Porous Media*. 2nd Edition. John Wiley & Sons., 1998.
- [7] Mašín, D. A hypoplastic constitutive model for clays. *International Journal for Numerical and Analytical Methods in Geomechanics* 29 (4), 311–336, 2005
- [8] Mašín, D. Predicting the dependency of a degree of saturation on void ratio and suction using effective stress principle for unsaturated soils. *International Journal for Numerical and Analytical Methods in Geomechanics* 34, 73–90, 2010
- [9] Mašín, D. Hypoplastic Cam-clay model. *Géotechnique* 62 (6), 549–553, 2012
- [10] Mašín, D. Double structure hydromechanical coupling formalism and a model for unsaturated expansive clays. *Engineering Geology* 165, 73-88, 2013
- [11] Mašín, D. Clay hypoplasticity model including stiffness anisotropy. *Géotechnique* 64 (3), 232–238, 2014
- [12] Mašín, D. Coupled thermohydromechanical double structure model for expansive soils. *ASCE Journal of Engineering Mechanics* 143, No. 9, 2017
- [13] Mašín, D., Khalili, N. A hypoplastic model for mechanical response of unsaturated soils. *International Journal for Numerical and Analytical Methods in Geomechanics* 32 (15), 1903–1926, 2008
- [14] Mašín, D., and Khalili, N. Swelling phenomena and effective stress in compacted expansive clays. *Can. Geotech. J.*, 53(1), 134–147, 2016
- [15] von Wolffersdorff, P. A. A hypoplastic relation for granular materials with a predefined limit state surface. *Mechanics of Cohesive-Frictional Materials* 1, 251–271, 1996
- [16] Wong, K. S. and Mašín, D. Coupled hydro-mechanical model for partially saturated soils predicting small strain stiffness. *Computers and Geotechnics* 61, 355-369, 2014
- [17] M. V. Villar, A. Gens, K. Černočová, J. Svoboda, D. Mašín, Milestone MS130: HITEC Task 3.3 – Modelling benchmarks – description (Description of calibration case, verification cases and benchmarks selected for T3.3 in cooperation with DONUT), Work Package 7, 4., 2021

3. VTT

3.1 Introduction

The objectives of the modelling are:

- 1) to contribute to experiments design in T3.1 and T3.2 from modelling perspective to ensure the ability to utilize the experimental results in THM modelling,
- 2) to develop the Varied Multiplicative Processes model to include thermal phenomena and dependencies, and
- 3) to interpret and compile obtained experimental data for modelling purposes.

The objective 1) includes pre-modelling to ensure relevant temperature conditions and input to experimental protocols.

3.2 Pre-modelling and input to experiments

3.2.1 Pre-modelling

Pre-modelling of the thermal conditions in Olkiluoto disposal site in Finland was performed to obtain a realistic view of the expected thermal conditions. The model includes thermal conduction through the disposal site components surrounding one disposal hole, but also thermal radiation is taken into account over gas filled gaps within the disposal canister (Figure 3.1).

The results show that the highest temperatures in bentonite buffer occur only very close to the disposal canister and the temperature elevates only to moderately high temperatures in the major parts of the buffer. Therefore, also moderately high temperatures should be of interest when performing experiments in over room temperatures. In addition, the sparsity of experimental data in this moderate to high temperature range supports the conclusion.

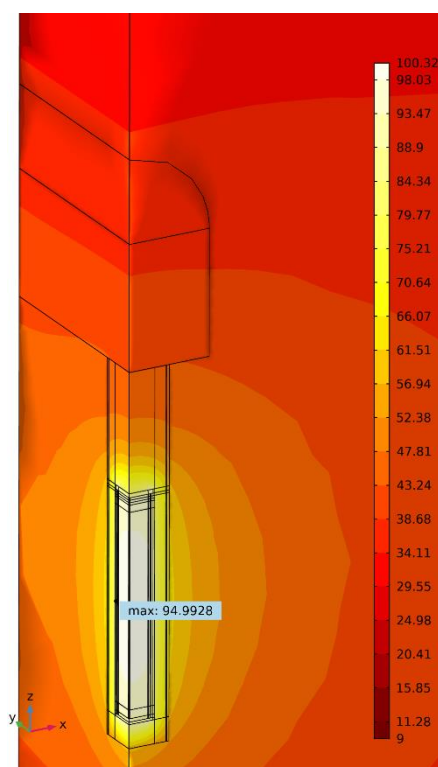


Figure 3.1. An example of modelled temperature field surrounding a disposal canister in Olkiluoto disposal site in Finland.

EURAD Deliverable 7.10 – HITEC Modelling

3.2.2 Input to experiments

High uncertainties in the thermo-hydro-mechanical (THM) models of bentonite relate to the basic elastoplastic mechanical model. For example, the elastic behaviour in the shear direction is not described with too much detail (often only constant Poisson's ratio or shear modulus is assumed) and there is little experimental data to define the yield surface or the hardening behaviour directly based on the data. Similarly, the elastic and plastic components of the deformation cannot be separated directly based on the experimental data due to its sparsity.

To reduce these uncertainties, VTT's experiments in T3.1 and T3.2 have been planned such that they provide the data that is needed for model development. The experiments are performed with a volumetric compaction and triaxial apparatus to cover both the pressure and shear directions of stress and deformation, although this is more complicated than, for example, experiments with oedometers (which provides data only in one stress-direction). Sufficient loading and unloading cycles are performed to be able to distinguish between elastic and plastic deformations directly based on the experimental data.

To obtain high quality data for model development, the sample preparation procedure has been planned such that unwanted effects have been minimised. The samples are saturated to a wanted saturation degree by vapour equilibrium technique to avoid unwanted chemical effects (dissolution of side minerals, which may eventually change the cation composition of bentonite) and excess mechanical processing (for example, mixing). Pre-samples are compacted from powder with isotropic pressure (the compression data is also saved for accurate information of the processing history) to avoid anisotropic effects. The pre-samples are machined to final samples with desired shape and dimensions. The quality of the samples is monitored with X-ray tomography to avoid experiments with, for examples, pre-cracks. The triaxial apparatus is calibrated by measuring the deformation of the equipment (and a steel dummy) using similar stress-paths as the actual experiments.

The experiments cover triaxial tests with heat treated bentonite (powder) and at elevated temperatures as well as reference test with non-heat-treated bentonite in room temperature. Consequently, they provide information and data of the mechanical properties of heat-treated bentonite and at high temperature that can be used to extend THM models to these conditions.

3.3 Thermal phenomena to Varied Multiplicative Processes model

The aim of the modelling is to include thermal phenomena to the Varied Multiplicative Processes (VMP) model framework (Pulkkanen, 2019). The basic concepts and results are summarised in this chapter.

3.3.1 Conceptual model

Bentonite is conceptually divided into two (fig):

- the skeleton which contains
 - the solid material of the bentonite (montmorillonite and excess minerals)
 - the bound water that is adsorbed onto the surfaces of the montmorillonite
- the free porosity that is filled with
 - free water or
 - gas.

The adsorbed (or bound) water is considered to be an integral part of the solid structure and therefore conceptualized as a part of the skeleton. The bound water is the water that is attached to the interlamellar and stack outer surfaces of montmorillonite in the sense that the mass of this water can be measured by weighting when bentonite is equilibrated with water vapour at a fixed relative humidity. The chemical potential of this vapour in equilibrium with the bound water is taken as the chemical potential of the bound water. An assumption is that the bound water increases the volume of the skeleton by the volume that the bound water would occupy if it was liquid. This assumption should be further investigated by experiments with different bentonite types in different conditions and refined according to the results.

EURAD Deliverable 7.10 – HITEC Modelling

The free porosity is the pore space that is not a part of the skeleton, that is, the pore space that is not the solid material or the bound water. The free porosity can be filled with liquid water (called free water here) or gas. Salts can be dissolved in the free water.

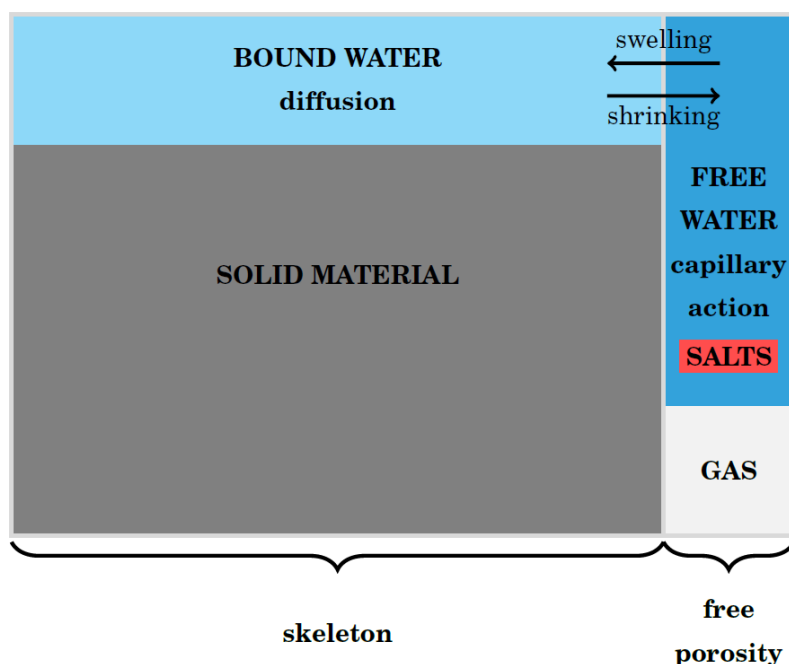


Figure 3.2. An illustration of the conceptual model. Solid material and bound water form the bentonite skeleton, while the free porosity is filled either with gas or (free) water where salts can be dissolved. If water moves from the free porosity to the bound state, the bentonite swells. If the movement of water is in reverse direction, the bentonite shrinks.

The VMP model is a large deformation model with extensive background of terminology and concepts that deviate from those used in the standard linear deformation theories. These are not repeated in this document, but the reader is advised to see (Pulkkanen, 2019) and the therein referred literature including, for example, (Gurtin et al. 2009).

3.3.2 (Im)balance equations

The following balance and imbalance equations are used to formulate the model.

The mass balance equation for the bound water is

$$\dot{m}_R = -\text{Div} \mathbf{h}_R + h_R, \quad (0.1)$$

where the dot denotes material time derivative, m_R is the mass density of bound water in the reference frame (mass of water per the volume of reference frame), Div the divergence operator in the reference frame, \mathbf{h}_R is the mass flux of bound water in the reference frame, and h_R the referential bound water supply.

The force balance equation is

$$\text{Div} \mathbf{T}_R + \mathbf{b}_{0R} = 0. \quad (0.2)$$

EURAD Deliverable 7.10 – HITEC Modelling

Where Div is the divergence operator in reference frame, \mathbf{T}_R the first Piola stress and \mathbf{b}_{0R} the referential inertial frame body force.

The free energy balance equation is

$$\dot{\varepsilon}_R = \frac{1}{2} \mathbf{T}_{RR} : \dot{\mathbf{C}} - \text{Div} \mathbf{q}_R + q_R - \text{Div}(\mu \mathbf{h}_R) + \mu h_R, \quad (0.3)$$

where ε_R is the referential internal energy, \mathbf{T}_{RR} the second Piola stress, $:$ the tensor inner product, \mathbf{C} the right Cauchy-Green strain tensor, \mathbf{q}_R the referential heat flux, q_R the referential heat supply, and μ the bound water chemical potential (in units J/kg).

The Helmholtz free energy imbalance is

$$\dot{\psi}_R + \eta_R \dot{\mathcal{G}} - \mathbf{T}_R : \dot{\mathbf{F}} - \mu \dot{m}_R + \mathbf{h}_R \cdot \nabla \mu + \frac{1}{\mathcal{G}} \mathbf{q}_R \cdot \nabla \mathcal{G} \leq 0, \quad (0.4)$$

where $\psi_R = \varepsilon_R - \mathcal{G} \eta_R$ is the referential Helmholtz free energy, η_R the specific referential entropy, \mathcal{G} the (absolute) temperature, \mathbf{F} the deformation gradient and ∇ referential gradient. For simplicity, the terms arising from plastic flow are not included.

3.3.3 Multiplicative decomposition of the deformation gradient

The VMP model is a large deformation model where the deformation gradient \mathbf{F} is decomposed multiplicatively

$$\mathbf{F} = \mathbf{F}_e \mathbf{F}_c \mathbf{F}_t \mathbf{F}_p \quad (0.5)$$

to the elastic \mathbf{F}_e distortion corresponding to mechanical elastic deformation, chemical \mathbf{F}_c (isotropic) chemical distortion corresponding to swelling due to water moving to adsorbed state, \mathbf{F}_t (isotropic) thermal distortion corresponding to thermal expansion and \mathbf{F}_p plastic distortion corresponding to mechanical plastic deformation.

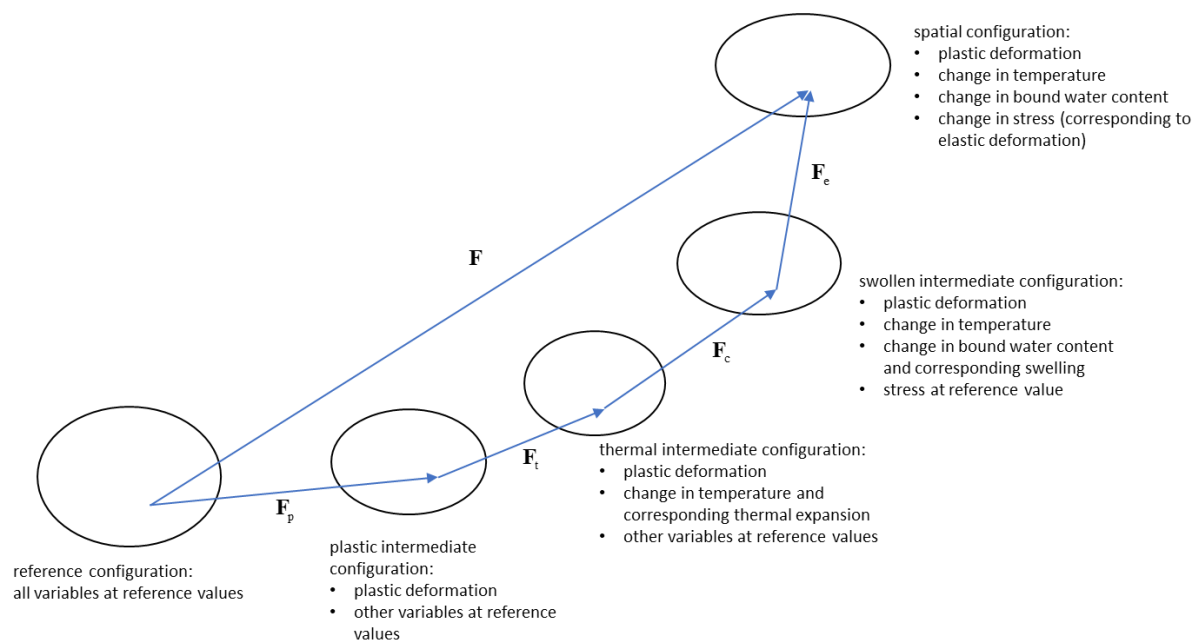


Figure 3.3. Illustration of the multiplicative decomposition of the deformation gradient, mapping properties and the intermediate configurations corresponding to the decomposition.

3.3.4 Constitutive assumptions and equations

It is assumed that swelling of bentonite due to adsorbed water intake is isotropic:

$$\mathbf{F}_c = b\mathbf{I} \quad (0.6)$$

leading to

$$J_c = \text{tr } \mathbf{F}_c = b^3, \quad (0.7)$$

where J_c is the volumetric Jacobian of the chemical distortion (ratio of volume change due to swelling) and b the chemical stretch ratio.

Similarly, it is assumed that the volume change of bentonite due to thermal expansion is isotropic:

$$\mathbf{F}_t = d\mathbf{I} \quad (0.8)$$

leading to

$$J_t = \text{tr } \mathbf{F}_t = d^3, \quad (0.9)$$

where J_t is the volumetric Jacobian of the thermal expansion (ratio of volume change due to the thermal expansion) and d the thermal stretch ratio.

The constitutive equations are formulated assuming that the constitutive relations for the dependent variables can be derived from the free energy of the system. For simplicity, plastic deformation is left out and the focus is on adding the thermal effect to the model.

The independent variables in the model are a measure for the deformation (Green – St.Venant strain

$\mathbf{E} = \frac{1}{2}(\mathbf{C} - \mathbf{I})$ or right Cauchy Green deformation tensor \mathbf{C}), referential mass density of the bound

EURAD Deliverable 7.10 – HITEC Modelling

water m_R and the temperature \mathcal{G} . These correspond to the use of Helmholtz free energy as the free energy from which the constitutive relations are derived. The constitutive equations for the dependent variables: the second Piola stress \mathbf{T}_{RR} , the referential specific entropy η_R and the bound water chemical potential μ are sought.

Using the assumption of frame indifference, the Coleman-Noll procedure (with standard assumptions) and the Maxwell relations (following from the procedure, Gurtin et al. 2009), the linearised constitutive relations are

$$\begin{aligned} \psi_R = & \frac{1}{2} \kappa_m (\log J_e)^2 + G_m |\text{dev } \mathbf{E}|^2 + \beta (\mathcal{G} - \mathcal{G}_0) \text{tr } \mathbf{E} \\ & + s (m_R - m_{R0}) \text{tr } \mathbf{E} + a (m_R - m_{R0}) (\mathcal{G} - \mathcal{G}_0) + \psi_R^c (m_R) - \frac{c}{2\mathcal{G}_0} (\mathcal{G} - \mathcal{G}_0)^2 \end{aligned} \quad (0.10)$$

$$\mathbf{T} = \frac{\partial \psi_R}{\partial \mathbf{C}} = \kappa_m \log(J_e) \mathbf{I} + 2G_m \text{dev}(\mathbf{E}) + \beta (\mathcal{G} - \mathcal{G}_0) \mathbf{I} + s (m_R - m_{R0}) \mathbf{I} \quad (0.11)$$

$$\eta_R = \frac{\partial \psi_R}{\partial \mathcal{G}} = \eta_{R0} - \beta \text{tr } \mathbf{E} + \frac{c}{\mathcal{G}_0} (\mathcal{G} - \mathcal{G}_0) + a (m_R - m_{R0}) \quad (0.12)$$

$$\mu = \frac{\partial \psi_R}{\partial m_R} = \mu_0 + s \text{tr}(\mathbf{E} - \mathbf{E}_c) + a (\mathcal{G} - \mathcal{G}_0) + \mu^c (n_R) \quad (0.13)$$

$$\mathbf{h}_R = -L m_R \nabla \mu - M \nabla \mathcal{G} \quad (0.14)$$

$$\mathbf{q}_R = -k \nabla \mathcal{G} - N \nabla \mu \quad (0.15)$$

Here, κ_m is the bulk modulus (at constant bound water content and temperature), $J_e = \text{tr } \mathbf{F}_e$ the volumetric Jacobian of the elastic distortion, G_m the shear modulus (at constant bound water content and temperature), $\beta = -3\kappa_m \alpha$ (for small deformations) with $\alpha = \frac{1}{d} \frac{\partial d}{\partial \mathcal{G}}$ the coefficient of thermal expansion, \mathcal{G}_0 the reference temperature, $s = -3\kappa_m \gamma$ (for small deformations) with the coefficient of chemical expansion $\gamma = \frac{1}{b} \frac{\partial b}{\partial m_R}$ due to bound water intake ($\gamma = \frac{1}{3\rho_w}$ with water density ρ_w for small swelling deformation), c the bentonite heat capacity (at constant bound water content), a the chemical-thermal interaction modulus, m_{R0} the reference bound water content, $\mu^c = \frac{\partial \psi_R^c}{\partial m_R}$ the adsorption isotherm of bentonite powder at zero stress, $\mathbf{E}_c = \gamma (m_R - m_{R0})$ the chemical strain due to swelling, L the mass transport coefficient for adsorbed water diffusion driven by chemical potential gradient, M the mass transport coefficient for thermal diffusion driven by temperature gradient, k the thermal conductivity for bentonite (including solid material and water) and N the heat transfer coefficient for heat transfer driven by chemical potential gradient.

The correction for the swelling back-coupling derived by using the multiplicative decomposition and the following intermediate configurations for linearisation is utilised (Pulkkanen, 2019) meaning that the chemical strain is subtracted from the Green-St.Venant strain in the constitutive relation for the bound

EURAD Deliverable 7.10 – HITEC Modelling

water chemical potential. Also, linear volumetric strain in the mechanical constitutive equations has been replaced by a modified logarithmic strain formulation.

The large deformation flow rule, the yield surface and the hardening/softening laws are not derived here and simple parameter dependency on the temperature is assumed. It simply stated here that, for now, Cam clay yield surface (Gens and Alonso, 1992)

$$f_y = q^2 + M^2(p - p_c)p = 0, \quad (0.16)$$

with the hardening law

$$p_c = p_{c0} - \lambda \ln J_p \quad (0.17)$$

is assumed. Here $q = \sqrt{3J_2}$ is the deviatoric stress, $p = -\frac{1}{3}I_1$ the pressure, M a parameter, p_c the previous highest compression (in the direction of p) of the material, p_{c0} the initial value for p_c , λ a material parameter and J_p the volumetric Jacobian of the plastic distortion. Parameter dependency on bound water density and temperature are assumed.

3.3.5 Discussion on included thermal phenomena

Thermal phenomena have been added to the VMP model thermodynamically consistently. The procedure has followed the similar principles as when building the original VMP model. The model now consists of

- the mass balance equation for adsorbed water transport,
- force balance equation for mechanical behaviour and
- thermal balance equation including thermal terms.

The constitutive equations have been derived thermodynamically consistently (and taking principle of frame indifference into account) such that they are as general as possible (compare to Pulkkanen, 2019, and Gurtin et al. 2009). Consequently, the constitutive equation for the second Piola stress includes (besides mechanical elasticity) swelling due to adsorbed water intake and thermal expansion. The thermal expansion has been added using multiplicative decomposition of deformation gradient, although linearisation at the swollen intermediate configuration would likely be enough due to the small effect in comparison to adsorbed water induced swelling. Besides the standard term including temperature, the constitutive equation for specific referential entropy includes mechanical term and a term arising from water adsorption. Especially the latter is a novel addition and its importance (or lack of it) should be studied experimentally. Similarly, the value or function for the thermal-chemical interaction coefficient should be measured. The thermal term in the constitutive equation for chemical potential is a new addition to the former VMP constitutive equation. Again, its importance and the value for the introduced thermal-chemical interaction coefficient should be experimentally determined.

Beside the expanded energy balance equation (to include thermal phenomena) and the extended constitutive equation, an important thermal effect is the constitutive equation parameter dependency on the temperate. Moreover, the memory effect of elevated temperature may be important (if the parameters are changed due to thermal treatment). These have been the topics for experimental Tasks 3.1 and 3.2 for VTT.

3.4 Thermal dependency of mechanical constitutive models

The experimental results by VTT in Task 3.1 suggest that the effect of heat treatment at 105°C or 150°C as powder for 6 months on the elastoplastic compressive behaviour of Wyoming sodium bentonite is negligible. Consequently, the same parameters for elastic and plastic constitutive equation as for non-

EURAD Deliverable 7.10 – HITEC Modelling

heat-treated bentonite could be used in the modelling. The rest of the experimental work for the mechanical model dependencies on the temperature by VTT is still on-going when writing this deliverable (October 2023).

3.5 References

Gens, A. & Alonso, E. E., 1992. *A framework for the behaviour of unsaturated expansive clays*, Canadian Geotechnical Journal, 29, pp. 1013–1032.

Gurtin, M. E., Fried, E., and Anand, L., 2009. *The Mechanics and Thermodynamics of Continua*. Cambridge University Press.

Pulkkanen, V.-M., 2019. *A large deformation model for chemoelastic porous media - Bentonite clay in spent nuclear fuel disposal*. D.S. (Tech.) Thesis. Aalto University.